

United Aircraft Research Laboratories



EAST HARTFORD, CONNECTICUT

H-910091-19

Experimental Investigations to
Simulate the Thermal Environment,
Transparent Walls, and
Propellant Heating in a
Nuclear Light Bulb Engine

NASA Contract No. NASw-847

REPORTED BY Ward C. Roman
Ward C. Roman
John F. Klein
John F. Klein
Paul G. Vogt
Paul G. Vogt

APPROVED BY James W. Clark
James W. Clark, Chief
Fluid and Systems Dynamics

DATE September 1969

NO. OF PAGES 118

COPY NO. 66

FOREWORD

An exploratory experimental and theoretical investigation of gaseous nuclear rocket technology is being conducted by the United Aircraft Research Laboratories under Contract NASw-847 with the joint AEC-NASA Space Nuclear Propulsion Office. The Technical Supervisor of the Contract for NASA is Captain C. E. Franklin (USAF). Results of portions of the investigation conducted during the period between September 15, 1968 and September 15, 1969 are described in the following five reports (including the present report) which comprise the required ninth Interim Summary Technical Report under the Contract:

1. Roman, W. C., J. F. Klein, and P. G. Vogt: Experimental Investigations to Simulate the Thermal Environment, Transparent Walls and Propellant Heating in a Nuclear Light Bulb Engine. United Aircraft Research Laboratories Report H-910091-19, September 1969. (present report)
2. Mensing, A. E. and J. F. Jaminet: Experimental Investigations of Heavy-Gas Containment in R-F Heated and Unheated Two-Component Vortexes. United Aircraft Research Laboratories Report H-910091-20, September 1969.
3. Krascella, N. L.: Theoretical Investigation of the Radiant Emission Spectrum from the Fuel Region of a Nuclear Light Bulb Engine. United Aircraft Research Laboratories Report H-910092-12, September 1969.
4. Latham, T. S., H. E. Bauer, and R. J. Rodgers: Studies of Nuclear Light Bulb Start-up Conditions and Engine Dynamics. United Aircraft Research Laboratories Report H-910375-4, September 1969.
5. Johnson, B. V.: Exploratory Experimental Study of the Effects of Inlet Conditions on the Flow and Containment Characteristics of Coaxial Flows. United Aircraft Research Laboratories Report H-910091-21, September 1969.

Experimental Investigations to Simulate the
Thermal Environment, Transparent Walls, and Propellant Heating in a
Nuclear Light Bulb Engine

TABLE OF CONTENTS

	<u>Page</u>
SUMMARY	1
RESULTS	3
SECTION I - INTRODUCTION	6
SECTION II - DESCRIPTION OF PRINCIPAL EQUIPMENT	8
UARL 1.2-Megw R-F Induction Heater	8
Background	8
Primary Heater Components	8
Test Chamber	9
Plasma Starting System	9
Water Cooling and Gas Systems	10
Control Console	10
Diagnostic Equipment	10
Spectral Emission Measurements	10
Total Radiation Measurements	11
Optical Scanning Device for Plasma Diameter Measurements	12
Viewing Screen for Observing Real-Time Plasma Behavior	12
Photographic Equipment for Plasma Size, Shape, and Stability Observations	12
SECTION III - RADIANT ENERGY SOURCE PROGRAM	13
Objectives of Program	13
Description of Equipment	13
Basic End-Wall Configuration	13
Test Chamber Water-Dye Coolant	15

TABLE OF CONTENTS (Continued)

	<u>Page</u>
SECTION III - (Continued)	
Test Procedures For 1.2-Megw R-F Induction Heater	15
Discussion of Test Techniques and Results	16
Effects of Discharge Power on Radiant Energy Source	
Geometric Characteristics and Power Loss	
Mechanisms	16
Effects of Pressure on Radiant Energy Source	
Characteristics	21
SECTION IV - TRANSPARENT-WALL MODEL PROGRAM	25
Objectives of Program	25
Model Fabrication Techniques	25
Models With Axial Coolant Tubes	25
Models With Circumferential Coolant Tubes	27
Test Procedures	28
Discussion of Models and Test Results	28
Tests With 1.26-in.-ID Axial-Coolant-Tube Models	28
Tests With 0.95-in.-ID Axial-Coolant-Tube Models	29
Comparison of Operating Conditions of Full-Scale Engine, R-F Plasma Radiant Energy Source and Models	30
Heat Transfer Limitation in Model Tests	31
SECTION V - INITIAL SIMULATED PROPELLANT HEATING PROGRAM	32
Background	32
Objectives of Program	33
Description of Equipment	33
Seed Dispersal System	33
Cold-Flow Configurations	34
Propellant Heating Configuration Used With D-C	
Arc Heater	35
Concentric-Coolant-Tube Model Configuration	35
Propellant Heating Configurations Used With The 1.2-Megw Induction Heater	35

TABLE OF CONTENTS (Continued)

Page

SECTION V - (Continued)

Test Procedures	37
D-C Arc Heater	37
Cold-Flow Tests	37
Propellant Heating Tests	37
Discussion of Test Results	38
Tests With Cold-Flow Configurations	38
Tests With Concentric-Coolant-Tube Model Configuration	39
Tests With Axial-Coolant-Tube Model Configuration	43
REFERENCES	45
LIST OF SYMBOLS	48
APPENDIX A - PRELIMINARY DESIGNS FOR 200- AND 500-ATM R-F PLASMA TEST EQUIPMENT	52
APPENDIX B - DIMENSIONAL CHARACTERISTICS AND HYDROSTATIC TESTS OF FUSED SILICA TUBES	59
APPENDIX C - DESCRIPTION OF D-C ARC HEATER	60
APPENDIX D - OPTICAL PROPERTIES OF PARTICLE CLOUDS	64
TABLES	68
FIGURES	73

Experimental Investigations to Simulate the
Thermal Environment, Transparent Walls, and Propellant Heating in a
Nuclear Light Bulb Engine

SUMMARY

Experiments were conducted to develop an intense radiant energy source capable of producing radiant energy fluxes within the range expected in nuclear light bulb engines. Concurrently, small-scale internally cooled fused silica models similar to the transparent walls proposed for the engine were developed and tested. Experiments to demonstrate heating of a seeded simulated propellant by thermal radiation passing through the transparent wall were also initiated.

The major portion of the test program was conducted using the UARL 1.2-megw radio-frequency induction heater at d-c input power levels up to approximately 600 kw. R-F energy was supplied to an argon plasma within a radial-inflow vortex. The effects of several important parameters on the power radiated from the plasma, the power deposited in the surrounding water-cooled transparent peripheral wall, and the power carried away from the vortex by convection were investigated. Tests were conducted with argon at pressures up to 16 atm and with up to 216 kw of power deposited in the steady-state plasma discharge. A maximum of 156 kw was radiated through a 2.24-in. inside diameter water-cooled transparent peripheral wall. The maximum radiant energy flux at the edge of the plasma was 36.7 kw/in.^2 , which corresponds to an equivalent black-body radiating temperature of 10,200 R. For reference, the range of edge-of-fuel radiant energy fluxes of interest for full-scale nuclear light bulb engines is from 177.8 kw/in.^2 for a reference engine to 14.4 kw/in.^2 for a derated engine; the corresponding equivalent black-body radiating temperatures are 15,000 R and 8000 R, respectively.

Transparent-wall models having multiple axial coolant tubes up to 10 in. long and peripheral-wall vortex injection were fabricated and tested in the 1.2-megw r-f induction heater. These models, with inside diameters of 1.26 and 0.95 in., were constructed from many individual tubes having internal diameters of 0.040 in. and wall thicknesses down to 0.005 in., the estimated thickness required in the full-scale engine. One of these models was tested at power levels up to 55 kw; higher power levels resulted in localized melting of the argon-cooled vortex injectors.

Both the UARL 1.2-megw r-f induction heater and the d-c arc heater were used in the propellant heating tests. The propellant heating configurations used were generally similar to the geometries of the components expected to be employed in the nuclear light bulb engine. Argon seeded with micron-sized carbon particles was used as the simulated propellant. At the low radiant energy source power levels of up to 3 kw that were used in these initial tests, temperature rises up to 223 R were obtained. Further increases in simulated propellant temperature rise will be obtained primarily by means of increased power, improved particle deagglomeration to increase absorption, and more effective buffer layers to reduce the coating of particles on the transparent walls.

RESULTS

1. An intense radiant energy source was developed using the UARL 1.2-megw r-f induction heater. The experiments were conducted with a 5.5 MHz r-f argon plasma which was contained using a radial-inflow vortex within a test chamber formed by concentric water-cooled fused silica tubes with copper end walls. The plasma was ellipsoidal with a major axis of 2 in. and a minor axis varying between 0.64 in. and 0.96 in. The experiments were conducted at pressures up to 16 atm and argon weight flow rates up to 0.041 lb/sec. The following levels of performance were attained:
- a. The maximum steady-state power deposited into the plasma was 216 kw. The corresponding plasma diameter at the mid-plane (minor axis) was 0.82 in. A maximum power density of 328 kw/in.³ occurred at a pressure of 8.5 atm.
 - b. The maximum power radiated through the inner water-cooled transparent wall was 156 kw. The corresponding radiation flux based on the surface area of the plasma was 36.7 kw/in.², and the corresponding equivalent black-body radiating temperature was 10,200 R.
 - c. The plasma diameter at the mid-plane decreased with increasing argon weight flow rate and, to a lesser extent, with increasing chamber pressure. Within the experimental range tested, the plasma could be maintained in a relatively laminar, stable ellipsoidal geometry. Test times averaged one hour.
 - d. The total power deposited into the plasma, the chamber pressure, and the argon weight flow rate are interrelated in determining the most stable operating conditions for a given geometry. Simultaneous increases in chamber pressure and r-f power into the plasma yielded the largest increases in the fraction of plasma power that was radiated through the inner transparent wall.
 - e. The radial temperature distributions determined from the observed chordal variation in intensity of the argon 4158.59 Å spectral line indicate a distinct off-axis peak. Typical plasma centerline temperatures ranged between 16,500 and 18,000 R, while the off-axis peak values were higher by approximately 10 percent.
 - f. Further increases in radiant energy source performance can be attained through increased pressure and increased power deposited in the plasma. This will require higher resonator voltages than are presently available (the maximum voltage available in these tests was limited by heating of certain of the vacuum capacitors in the r-f resonator).

2. Significant progress was made in the development of internally cooled transparent-wall models similar to the walls proposed for the nuclear light bulb engine. Models up to 10 in. long with 1.26- and 0.95-in. inside diameters and made from many individual tubes having internal diameters down to 0.040 in. and wall thicknesses of 0.010 and 0.005 in. were fabricated from standard-grade fused silica. An axial-coolant-tube model having a 1.26-in. inside diameter and a wall thickness of 0.020 in. was fabricated entirely from high-purity fused silica. Circumferential-coolant-tube model components having inside diameters of 1.26 in. and wall thicknesses of 0.20 in. were fabricated from standard-grade fused silica.

3. Tests with axial-coolant-tube models in the 1.2-megw r-f induction heater resulted in the following levels of performance:

- a. The maximum power deposited in the r-f discharge for a 1.26-in.-ID model was about 55 kw. The corresponding power radiated through the wall was 23.3 kw at 9.2 atm; 23.8 kw was deposited in the model cooling water. This model had a wall thickness of 0.010 in. The maximum discharge power was limited by localized melting of the argon-cooled copper injectors along the peripheral wall. Further increases in power can be attained by water-cooling these injectors.
- b. The maximum power deposited in the r-f discharge for the 0.95-in.-ID model was 16.6 kw. The corresponding power radiated through the wall was 3.6 kw at 2.8 atm; 10.35 kw was deposited in the model. This model had a wall thickness of 0.005 in. Further increases in power in this model can also be attained by water-cooling the peripheral-wall injectors.

4. Initial simulated-propellant heating tests using micron-sized carbon seed material dispersed in an argon carrier gas were conducted using both the 1.2-megw r-f induction heater and the d-c arc heater radiant energy sources.

- a. Initial low-power-level tests employed configurations in which the seed duct was an annulus formed by two concentric fused silica tubes. The pressure in the seed duct was about one atm and the simulated-propellant velocity was about 20 ft/sec. The average temperature rise in the exhaust of the simulated propellant stream was typically 30 R; the maximum temperature rise attained was 223 R. The average value of β , the mass attenuation coefficient, was only about 10^3 cm²/gm, and the maximum fraction of the radiation absorbed was 0.33.
- b. Later tests employed configurations in which multiple axial-coolant-tube models formed the inner wall of the propellant duct. For these tests, coating of the transparent-wall model also occurred. Interaction between

the vortex flow in the model and the simulated propellant flow may have caused the coating of the model by the carbon seed. This coating prevented the deposition of significant amounts of radiant energy in the simulated propellant.

- c. Increases in the amount of radiant energy absorbed can be achieved through (1) use of thicker buffer layers between the seeded stream and the duct walls to prevent coating, (2) use of deagglomeration techniques at locations other than the duct inlet to increase the mass attenuation coefficient, and (3) use of increased radiant energy source power levels.

SECTION I

INTRODUCTION

An experimental and theoretical investigation of gaseous nuclear rocket technology is being conducted by the United Aircraft Research Laboratories (UARL) under Contract NASw-847 administered by the joint AEC-NASA Space Nuclear Propulsion Office. This investigation is presently directed toward the nuclear light bulb engine concept. This engine would consist of seven unit cavities similar to that shown schematically in Fig. 1. In this concept, heat is transferred from gaseous fissioning fuel through an internally cooled transparent wall to seeded hydrogen propellant. A transparent buffer gas, such as neon, is injected at the inner surface of the transparent wall to form a vortex which isolates the fuel from the wall. Because of the high temperatures obtainable in the gaseous fuel, engines of this type can theoretically provide specific impulses of 1500 to 3000 sec and thrust-to-weight ratios greater than one. The concept is also attractive because the physical barrier between the fuel and propellant offers the possibility of perfect containment of fuel and fission products. Additional details of the nuclear light bulb concept are discussed in Ref. 1, and the fluid mechanics requirements are discussed in Ref. 2.

Recent fluid mechanics experiments related to the nuclear light bulb engine are reported in Refs. 3 and 4. This research emphasized preliminary radiant energy source tests in the UARL 1.2-megw r-f induction heater facility. Initial tests (Ref. 3) demonstrated that an internally cooled transparent wall could be located adjacent to the plasma while maintaining its structural integrity.

The research program discussed in the present report was concerned with simulating fluid-dynamic containment and radiant energy flux of the gaseous nuclear fuel, and the transfer of radiant energy from the simulated fuel to a seeded simulated propellant. The fabrication and testing of internally cooled transparent walls which form the interface between the fuel and propellant is also discussed herein. Major emphasis was placed on use of the UARL 1.2-megw r-f induction heater to develop a non-nuclear light source that will provide steady-state radiant energy fluxes similar to those expected for the full-scale engine. Emphasis was also placed on the development of techniques to provide information on the fabrication of thin transparent-wall models with walls similar to those proposed for the actual engine, and on initial propellant heating tests. The latter portion of the research effort is designed to eventually lead to heating of a simulated propellant at the full-scale radiant energy flux with a transparent-wall model located between the radiant energy source and the simulated propellant.

The primary objectives of the research reported herein were: (1) to determine the factors that influence the size, shape, stability, and power deposition in confined

gas vortex r-f plasma discharges, (2) to maximize the percentage of total plasma power that is radiated, thus operating the plasma in a radiation-dominated mode, (3) to design, fabricate, and test several different types of thin, internally cooled, transparent-wall models around the radiant energy source, and to determine their operating limitations, and (4) to conduct initial propellant heating experiments using both the 1.2-megw r-f induction heater and a lower-power d-c arc heater. Other objectives included preliminary design of 200- and 500-atm r-f radiant energy sources (See Appendix A).

This experimental investigation was organized into three programs, each based on one of the primary objectives. Accordingly, this report is divided into sections corresponding to the research in the Radiant Energy Source Program, Transparent-Wall Model Program, and Initial Simulated Propellant Heating Program. The principal equipment common to all three programs is described in the following section.

SECTION II

DESCRIPTION OF PRINCIPAL EQUIPMENT

This section contains descriptions of the UARL 1.2-megw r-f induction heater and the principal diagnostic equipment. Details of the vortex chamber end walls, the transparent-wall models, and other special equipment used in each of the three programs---the Radiant Energy Source Program, the Transparent-Wall Model Program, and the Initial Simulated Propellant Heating Program--are discussed later under the appropriate program. A summary of all of the geometries of the test configurations used in all three programs is presented in Table I.

UARL 1.2-Megw R-F Induction Heater

Background

The UARL 1.2-megw r-f induction heater was constructed during 1966 and 1967 as part of a Corporate-sponsored program. This heater was designed to ultimately be capable of depositing approximately 600 kw of r-f power into a small gas discharge; to date the maximum power deposited in a small gas discharge (0.7 in.³) has been 216 kw (see Section III).

Primary Heater Components

A block diagram showing the primary components of the heater is presented in Fig. 2. The operating frequency is selected by means of a variable-frequency oscillator. The oscillator output is stepped-up through a sequence of r-f power amplifiers to an intermediate power level of 80 kw at the output of a buffer amplifier. This power level is further amplified to 880 kw by a pair of power amplifier tubes connected in a push-pull configuration. The category of operation is class "C". The r-f power output from these tubes drives a resonant tank circuit (resonator section) of unique design.

The power levels indicated within the blocks of Fig. 2 correspond to the maximum rated r-f output for each component. Voltage levels noted on Fig. 2 correspond to the maximum rated d-c voltage input for the various amplifiers. Each power amplifier tube requires 600 kw of d-c input power to produce 440 kw of r-f output power. The maximum total d-c input power to the power amplifiers employed in gas discharge tests during this program was approximately 600 kw. However, as part of a Corporate-sponsored research program, the heater has been operated at input d-c power levels exceeding 700 kw.

Photographs of the resonator section are shown in Fig. 3. The resonator section and load are located within a 56-in.-dia cylindrical aluminum test tank which is not shown in Fig. 3(a). The resonator section consists of two arrays of ten vacuum capacitors; each array is connected with a single-turn work coil. The ends of the capacitors are water-cooled and r-f chokes are installed in the cooling water lines.

Figure 3(b) is a photograph showing details of the work coils. Each 3.06-in.-dia coil consists of five internally water-cooled 0.187-in.-dia copper tubes which were silver soldered together to form a single structure. The work coils were silver plated to reduce the power loss due to resistive heating.

Test Chamber

A pair of concentric water-cooled fused silica tubes approximately 39-in. long located within the r-f heater work coils form the outer boundary of the test chamber (Fig. 4). These inner and outer fused-silica tubes have wall thicknesses of 0.080 and 0.120 in., respectively. By using O-ring seals at the extreme ends of each tube, the annulus between the tubes can be used for the water coolant. To provide end-wall simulation similar to that of the full-scale engine, a symmetrical pair of end walls were used to form the axial boundary of the test chamber. The various end wall configurations installed in the test chamber will be described in Sections III and IV. To reduce the intense radiation incident on the components within the test tank during plasma discharge tests, known concentrations of an organic, water-soluble dye were added to the test-chamber cooling water (see Section III).

Plasma Starting System

The plasma starting system utilized an auxiliary d-c arc which provided the initial ionization level necessary for sustained coupling with the r-f power. A 3-kw d-c arc is drawn between two movable electrodes along the centerline of the test chamber. Figure 4 also shows a block diagram of the test chamber and plasma starting system. The electrode material composition and shape, insulating materials, d-c arc starter current level, axial position of the electrodes within the test chamber, and speed of electrode withdrawal were all selected to minimize sputtering of electrode material in the test chamber which could result in damage to the transparent walls of the test configurations.

The starter electrodes used with the basic test chamber configuration shown in Fig. 4 consist of 0.086-in.-OD hemispherically tipped rods of 2 percent thoriaated tungsten. Different electrode diameters were used for other test configurations depending on the diameter of the end wall. Each electrode was connected to a copper drive rod of the starter assembly. Ceramic and fused silica sheath material was used

to electrically isolate the starting and drive rod assemblies from the test chamber and end walls. The starter assembly is described in detail in Ref. 3. Photographs of the arc starter in operation are shown in Fig. 5.

Water Cooling and Gas Systems

To provide the necessary cooling, two closed-loop water cooling systems, each with a total capacity of approximately 80 gallons, are used. A 180-psig system employing centrifugal pumps can supply up to 100 gpm of cooling water. A high-pressure 450-psig system using a positive displacement pump supplies up to 20 gpm of cooling water. In addition, to reduce the pressure pulsations inherent in positive displacement pumps, a high-pressure ripple filter is used to damp out the pressure pulsations to less than one percent. To permit long run time capability, particularly during the high-power and high-argon-weight-flow rate tests, an 11-bottle argon supply and manifold system was used.

Control Console

To conduct all tests in an efficient and safe manner, a central console housing both electrical and fluid flow controls was used. The console includes the cooling water flow meters and associated valving (to permit monitoring the cooling water flow rates after strong concentrations of dye were added, special magnetic flow meters were also used), argon flowmeter and high- and low-flow type pressure regulators and associated valving, auxiliary d-c arc starter controls, timing equipment, cooling-water pump controls, and the necessary safety interlocks and warning lights. To permit simultaneous monitoring of various critical measurements during the tests, a set of strip chart recorders and an automatic stepping temperature recorder were used.

Diagnostic Equipment

Spectral Emission Measurements

The optical system used to obtain spectral emission measurements is shown in Fig. 6. A Jarrell-Ash 82-410 0.25-meter Ebert monochromator and EMI 9558 photomultiplier detector were mounted on a traversing table to allow chordwise scans of the discharge. The monochromator has 25-micron-wide entrance and exit slits. A 13.5-in. focal length lens was positioned between the r-f plasma source and the entrance slit. The source spot size was 0.001 by 0.186 in. The lens was positioned such that the image size was equal to the spot size. Wavelength scans between 3500 Å and 8200 Å were made at a scanning rate of 1000 Å/min. A 5600 Å cut-off filter was placed in front of the monochromator entrance slit when spectral scans at wavelengths greater than 5600 Å were made to minimize second-order effects from lines at shorter wavelengths.

A calibrated neutral density filter to reduce the intensity of the incident light was also located in front of the monochromator entrance slit. The photomultiplier output was processed and recorded on a Honeywell Model 1108 Visicorder.

Total Radiation Measurements

The power radiated from the plasma discharge was measured using a specially constructed radiometer. A block diagram of the radiometer optical system and an oscilloscope trace of a typical output is presented in Fig. 7. A synchronous motor drives a chopper wheel containing four apertures. Calibrated filters with specific transmission characteristics were inserted into the apertures. For most tests, three of the apertures contained filters and the remaining one was open. In addition, a filter having upper and lower 50-percent transmission levels at 2.6 and 0.22 microns, respectively, was located behind the chopper wheel (see Fig. 7). A BaF₂ thermopile detector with a lower 50-percent cut-off at 0.25 microns was mounted in a blackened enclosure. The window of the enclosure had a collimating tube with a blackened inside surface. The transmission characteristics of all filters are shown in Fig. 8. The response of the thermopile with filters was calibrated using a Eppley Laboratory Calibrated Standard of Spectral Irradiance. Transmission characteristics, obtained from Ref. 5 for a 0.079-in.-thick layer of water corresponding to the water-coolant annulus between the fused silica transparent walls, are also shown. The output of the thermopile was connected to an operational amplifier and displayed on an oscilloscope. An r-f choke was used between the amplifier and oscilloscope. In addition, internal r-f shielding isolated the radiometer electronic system from the stray r-f fields; this was particularly necessary at the high power levels. A magnetic pickup probe on the chopper wheel synchronized the chopper wheel with the oscilloscope trace. For the tests reported herein, total radiation measurements were obtained in the following wavelength ranges: 0.25 to 0.3, 0.3 to 0.72, 0.72 to 1.0, and 1.0 to 1.3 microns. The lower wavelength cut-off was determined by the 50-percent transmission level of the individual filters in the radiometer or by the BaF₂ detector. The upper wavelength cut-off was determined by the 50-percent transmission level of the 0.079-in.-thick water layer located between the two fused silica tubes within the test chamber. Figure 7(b) shows an oscilloscope trace of the thermopile output signal in millivolts as a function of time for a typical output. To provide a continuous record of the total radiation in the wavelength band of 0.25 to 1.3 microns for selected tests, the output signal of the thermopile was connected through an r-f choke to a strip chart recorder. In this case, the chopper wheel was held stationary and the open aperture was used.

Following calibration of the radiometer with the standard lamp of known spectral characteristics, a calibration constant for each wavelength range was determined. The total power radiated from the plasma in each wavelength range was then calculated from the radiometer measurements by assuming isotropic radiation. For the tests in the 1.2-megw r-f induction heater, allowance was made for the blockage due to the presence of the r-f heater coils. For the case of an ellipsoidal discharge, about 55 percent of

the total discharge volume was visible to the radiometer.

Optical Scanning Device for Plasma Diameter Measurements

A sketch and photograph of the optical scanning system used for determining the representative discharge diameter are shown in Fig. 9. The system consists of a high-voltage power supply, an end-on photomultiplier tube (RCA 6655) mounted in a blackened enclosure, a fiber optic tube, an internally blackened collimating tube containing two apertures and baffles, a traversing mechanism driven by a synchronous motor, and a rotatable filter wheel containing several neutral density filters each having different transmission characteristics. The apertures were sized and located such that a 0.04-in.-dia spot was viewed. The traversing mechanism was attached, using a swivel mount, to the top view port of the experimental test tank (see Fig. 9). The distance between the r-f plasma discharge centerline and end of the collimating tube was 27 in. A counter was located on the synchronous drive assembly to indicate the displacement of the scanning device relative to the centerline of the r-f plasma. The output of the photomultiplier (proportional to light intensity) was displayed on a strip chart recorder.

Viewing Screen for Observing Real-Time Plasma Behavior

Continuous observation of the plasma during the tests in the 1.2-megw r-f induction heater was accomplished by using a specially constructed projection screen system. The system consists of a rotatable projection lens assembly containing an 18-in. focal length convex lens (see Fig. 9). The rotatable filter wheel containing neutral density filters was used with the optical scanning device to increase the filtering during tests at high power levels. When the lens and appropriate filter was placed in position over the upper view port of the experimental test tank, the image of the plasma discharge was projected onto an overhead screen. Horizontal and vertical grid lines placed on the screen permitted estimates to be made of the changes in the discharge diameter and shape as a function of the test parameters.

Photographic Equipment for Plasma Size, Shape, and Stability Observations

Various still and high-speed photographs and movies were taken of the plasma discharge from several of the view ports. A camera was employed to obtain black-and-white photographs of the discharge. High-speed color movies of the plasma discharge were taken using Milliken and Fastax cameras at framing speeds up to 8000 frames per second.

SECTION III

RADIANT ENERGY SOURCE PROGRAM

Objectives of Program

The r-f plasma discharge tests conducted during this program, using the 1.2-megw r-f induction heater, were directed at developing an intense non-nuclear steady-state radiant energy source capable of producing energy fluxes like those expected in a full-scale nuclear light bulb engine. Simulation of the thermal radiation environment of a nuclear light bulb engine requires a steady-state radiant energy source having an equivalent black-body temperature between 8000 and 15,000 R. To best satisfy these simulation requirements, a radiant energy source configuration was investigated which contained the r-f plasma in a small volume using an argon radial-inflow vortex flow pattern within a transparent-wall test chamber.

Major emphasis was placed on a series of r-f plasma discharge tests directed toward determining the effect of various parameters (e.g., discharge power, discharge pressure, argon vortex weight flow rate, and test geometry) on the plasma discharge size, shape, stability, and the fraction of total discharge power dissipated through the various modes of conduction, convection, and radiation heat transfer. In addition, tests were directed at maximizing the percentage of total plasma power that is radiated.

Description of Equipment

Basic End-Wall Configuration

The radiant energy source test chamber used in the 1.2-megw r-f induction heater tests reported herein was described in Section II and a block diagram of the test chamber is presented in Fig. 4. To permit safe operation at high power and pressure levels, calculations and static tests (see Appendix B) were performed to estimate the stress limits in the various transparent fused silica tubes used in the test chamber. These calculations included both hoop stress and thermal stress loading. The results indicated that by using the basic test chamber configuration shown in Fig. 10 (see also sketch for radiant energy source geometry in Table I), significantly high power and pressure levels (approximately 20 atm) could be achieved while maintaining a reasonable factor of safety.

The end walls that were used are shown within the test chamber in Fig. 10. They consist of a symmetrical pair of cylindrical, water-cooled copper end walls, 0.80-in. in diameter. They form the axial boundary of the plasma in the test chamber. The end-wall faces were spaced 2 in. apart and were located concentrically within the fused silica tubes of the test chamber. The faces of the end walls were lapped and polished to increase their reflectivity. To establish the desired radial-inflow vortex flow pattern, argon was injected through eight 0.10-in.-ID stainless steel vortex injectors located on a 1.44-in. diameter circle (see Fig. 10); the exit of the vortex injectors was in a plane 2.5 in. back from the face of the end wall. In most tests one set of these vortex injectors was located on each end wall. The vortex injectors were rigidly attached to the end wall using a copper spacer. This spacer serves as a support for the vortex injectors, provides a means for adjusting the injection angle (normally set approximately 10 deg from tangential), and allows the radial and axial location of the injectors to be varied. It is through this fluid-dynamic technique that control of the plasma discharge was effectively achieved. Various other vortex injection configurations were also tested (e.g., vortex injectors located on larger or smaller diameter circles, various diameter and total number of vortex injectors, and various locations of vortex injectors relative to the plasma discharge). The symmetric configuration employing a series of eight equally spaced 0.10-in.-ID injectors provided the best fluid-dynamic control of the plasma discharge over the test range reported. Previous cold flow results (Ref. 6) indicated stable vortex flow patterns occurred in a range of injection Reynolds number $Re_{t,j}$ comparable with those of the tests reported herein (approximately 10^5).

Each end wall contained a 0.185-in.-dia thru-flow port on the centerline. These ports were used to remove the argon test gas from the vortex chamber.

The cross section of the end walls shown in Fig. 10 illustrates the cooling-water flow passages used. These passages, together with the closed-loop high-pressure water-cooling system, provide the high-velocity flow of water cooling required to adequately cool the end walls. The cooling water flowed along the circumference of the end wall, radially inward across the end-wall face and was withdrawn axially around the thru-flow port. From heat transfer considerations, this permitted the greatest temperature difference across the end wall face in addition to taking advantage of centrifugal effects in the water in the annular region near the face.

The plasma discharge was produced in the region between the r-f work coils (see Fig. 10) with the major axis of the discharge colinear with the centerline of the coils. The test chamber can be viewed from different angles through five 4-in.-dia fused silica windows located in the front dome of the aluminum test tank (see Fig. 9).

Test Chamber Water-Dye Coolant

To reduce the intense radiation incident on the components within the test tank during gas discharge tests, known concentrations of an organic, water-soluble dye (nigrosine CI-50420) were added to the test chamber cooling water. Nigrosine was selected after various comparison tests were conducted to determine the type of dye or pigment with the most desirable spectral absorption characteristics. Figure 11 shows a direct comparison of the relative radiated power transmitted through the pigments or dye in several wavelength bands. The standard lamp described in Section II was used as the source in these comparison tests. The bar graph on the left in Fig. 11 shows the spectral absorption characteristics of the standard lamp over four wavelength bands between 0.25 and 1.3 microns as measured by the radiometer. The bar graph on the right presents the results obtained when a sufficient concentration of pigments or dye was added to reduce the total radiation from the lamp by a factor of four (note the difference in ordinate scales). For nigrosine, sufficient absorption in the 0.3-to 0.72-micron wavelength band was obtained. Tests were conducted to verify that the absorption characteristics of the coolant with nigrosine added were not influenced by the radiation from the plasma discharge or by the bulk temperature of the coolant for the range of test conditions employed. Results of other tests also showed the water-dye (nigrosine) coolant did not absorb r-f energy and thereby introduce errors into the energy balance calculations. In preliminary tests using the 1.2-megw r-f induction heater test chamber, the carbon black and cadmium red pigments partially coated the peripheral fused silica tubes and therefore would have prevented meaningful radiation measurements. Based on the results of these tests nigrosine (CI 50420), in concentrations varying from 200 to 1000 ppm, was selected for the test chamber cooling water.

Test Procedures For 1.2-Megw R-F Induction Heater

The sequence of events used during a typical test employing the 1.2-megw r-f induction heater is presented in Table II. Measurements of important electrical quantities, cooling water flow rates and temperature rises in certain critical parts of the heater are made during each test operation to provide the information required for performing a component and overall system energy balance. The auxiliary d-c arc starter technique has permitted moderately high power level r-f plasma discharges to be reliably started at pressure levels exceeding 5 atm.

Discussion of Test Techniques and Results

Effects of Discharge Power on Radiant Energy Source Geometric Characteristics and Power Loss MechanismsCriterion for Determining Plasma Diameter

For investigating the effects of power on the radiant energy source characteristics, it was necessary to establish a criterion for determining the r-f plasma discharge diameter. The determination of a representative r-f plasma discharge diameter is somewhat arbitrary due to the fact that, by using different filter densities combined with under- or over-exposing a photographic film, a wide variety of different apparent diameters can be obtained (Ref. 3). The temperature profiles of r-f plasma discharges exhibit a distinct off-axis peak and strong temperature gradients near the boundary (see Ref. 7); this introduces additional difficulty in determining a representative discharge diameter. Based on prior experience gained with photographic techniques, one method for obtaining a representative discharge diameter would be to take a photograph of the discharge and then use the relative density of the photographic negative as measured with a densitometer. In this case, constant film exposure must be maintained. An alternate method is to vary the exposure time over a range and plot the measured diameter as a function of exposure time. The resulting curve has a slight plateau which would correspond to the diameter of the current-conducting core.

Based on experience gained with photographic techniques for determining a representative r-f plasma discharge diameter using a suitable camera shutter speed, neutral density filter, and film exposure time (Ref. 3), a comparison was made with the results of the data taken using the optical scanning device. A Press camera was employed to obtain the photographs of the plasma which were used to compare with the measurements from the optical scanning system. The majority of the photographs were taken with Polaroid Type 57 film (ASA 3000) at f/16 and 1/100 sec. A No. 4.0 (i.e., 10^4 attenuation) neutral density filter was used for typical high-power test conditions. The comparison indicated the representative r-f plasma discharge diameter measured at a point on the output trace of the recorder where the intensity was equal to 1.0 percent of the peak intensity agreed within about 5 percent with measurements of the diameter determined from photographs. This 1.0-percent criterion was used in establishing the representative plasma diameter in the data presented herein. For a maximum temperature of about 20,000 R, the diameter selected in this way should represent an r-f argon plasma discharge with a boundary temperature of approximately 13,000 R (see following section). Below this temperature the electrical conductivity drops to a negligibly small value. Once an arbitrary discharge diameter was selected and defined through a chosen optical scanning and photographic technique, the various diameter changes of the r-f plasma discharge due to the influence of varying test parameters can be systematically compared.

Method for Measuring Total Power Deposited in Discharge

The total power deposited into the plasma discharge, Q_T , was obtained from an overall energy balance. The radiometer was used to measure Q_R , the radiated power escaping from the test chamber. All cooling water and argon weight flow rates were measured with rotameters. The cooling water inlet and exit temperature at the test chamber peripheral walls and end walls was also measured. This permitted calculating Q_W , the power deposited in the peripheral wall cooling water and Q_E , the power deposited in the end-wall cooling water. A water-cooled calorimeter attached to the end-wall thru-flow port exit measured Q_L , the amount of power convected out of the exhausts. The total discharge power was obtained from

$$Q_T = Q_R + Q_W + Q_E + Q_L \quad (1)$$

Effect of Power on Geometric Characteristics of Discharge

For the test configuration shown in Fig. 10, the effects of varying the total discharge power on the geometric characteristics of the discharge are illustrated in Fig. 12. Data are shown over a range of chamber pressure P_D and argon weight flow W_A (from 2 to 16 atm and from 0.010 to 0.041 lb/sec, respectively). A summary of results from tests in which Q_T is greater than 100 kw is presented in Table III. The discharge diameter shown on the ordinate was measured at the axial mid-plane of the test chamber using the technique discussed above. For reference, the upper two horizontal dashed lines show the inside diameter of the r-f work coils and the inside diameter of the inner fused silica tube of the test chamber. Within the range of experimental data shown, the plasma discharge could be maintained in a relatively laminar, stable geometry with diameters ranging between 0.64 and 0.96 in. It should be emphasized that to maintain a relatively laminar, stable discharge, the combination of discharge power, chamber pressure, and argon weight flow are interrelated; simultaneous changes in at least two of these parameters were necessary. For a fixed chamber pressure and relatively constant power level, the discharge diameter varied inversely with the argon weight flow rate. Large diameters could be obtained by decreasing the argon weight flow rate until indications of turbulence appeared at the boundary of the discharge. An example of this diameter change is illustrated in Fig. 12 (see data for Q_T equal to approximately 84 kw).

High-speed color movies were taken of the discharge through several of the view ports. Ektachrome (tungsten type) color film with an ASA number of 125 was used (together with color correcting filter for tungsten) with the 8000 fps camera. The movies indicate that the discharge is approximately ellipsoidal in shape. The pictures taken through the central view port located directly perpendicular to the discharge major

axis indicated an essentially constant diameter in the central 1.0-in. portion of the discharge. A double-mirror arrangement located inside the test tank permitted simultaneous orthogonal viewing of that portion of the discharge not blocked by the r-f work coils. This aided in verifying symmetry.

Assuming an ellipsoidal shape for the discharge, the discharge surface area and volume were computed using the axial mid-plane diameter as the minor axis of the ellipsoid. These volumes and surface areas are also shown on Fig. 12.

Discharge Stability

Frame-by-frame study of the high-speed color movies yielded information concerning the overall plasma discharge relative stability, and fluctuations in light intensity. To allow a comparison with the small fluctuations in intensity as viewed on the films, the output of the optical scanning device (with the collimating tube positioned on the discharge axis) was connected to the Visicorder. The galvanometer of the Visicorder had a response time of approximately one kilocycle. The Visicorder output indicated distinct periodic fluctuations in intensity corresponding to 360 Hz (the ripple frequency of the three-phase power supply). In the color movies, the amplitude of the discharge diameter change at mid-plane appeared to be less than 10 percent. This observed phenomena is similar to the so-called "breathing mode" of a d-c arc discharge powered by either moving-coil transformers or saturable-reactor power supplies. The inherent ripple found in this type of power supply leads to radial pulsations in the discharge accompanied by cyclic fluctuations in the light intensity.

Operation of the discharge at test conditions other than those which provide a relatively laminar, stable discharge sometimes resulted in discharges with random axial oscillations in the vicinity of the end-wall faces. The plasma discharge appeared to develop small plasma "tails" which at times would partially extend over the end wall. While test conditions required to initiate such a phenomena could be duplicated, the exact cause of this behavior is not understood. It is directly influenced by the type and location of the vortex injectors and the amount of flow removed through the end-wall thru-flow ports.

Discharge Power Loss Breakdown

A sketch of the end walls and r-f plasma discharge showing power losses for the highest power operating point is shown in Fig. 13. The test condition which resulted in the highest total discharge power (216 kw) occurred at a chamber pressure of 8.5 atm and resulted in a radiated power through the peripheral-wall water-dye coolant of 18 kw and a total power deposited into the peripheral-wall water-dye coolant of 147 kw. Each end wall removed 23.5 kw of power while each end-wall thru-flow port convected out 1.95 kw of power. The total power removed from the thru-flow ports is lower than

the end-wall power deposition. However, much of the power contained in the thru-flow ports is transferred to the annular cooling of the surrounding end walls prior to the exhaust flow reaching the end-wall exit location. Future modifications to the end walls will permit a more accurate determination of this power distribution. The discharge volume in this test was 0.71 in.³ and the corresponding surface area was 4.26 in.². Based on the conduction heat loss estimates through the inner peripheral wall, discussed in the following sub-sections, the total power radiated through the inner peripheral wall was 156 kw. This resulted in a value for the fraction of discharge power radiated through the inner peripheral wall Q_{RT}/Q_T , of 0.72. Thus, in the high power and pressure region of the tests conducted, the plasma was operating in a radiation-dominated mode. The total d-c input power to the induction heater, Q_I for the results shown in Fig. 13 was 600 kw (see Fig. 2). This corresponds to a tank circuit efficiency (defined by the ratio of the r-f power deposited in the load to the total r-f power output from the power amplifiers) of approximately 70 percent and an overall efficiency (defined by the ratio of the total discharge power to the total d-c input power) of 36 percent. The r-f input power to the discharge is determined by the r-f voltage supplied to the resonator section of the heater (see Fig. 2) and the impedance (related to the electrical conductivity) of the plasma which, in turn, determines the current level. The r-f voltage supplied to the resonator section was measured with a capacitive type voltage probe. Measurements of the total d-c input power were obtained by monitoring the power supply voltage and current. The power into critical parts of the heater system were also monitored and recorded to provide an overall energy balance for the system.

Discharge Power Density

The variation of discharge power per unit volume with total discharge power corresponding to the data presented in Fig. 12 is illustrated in Fig. 14. For reference, lines of constant discharge volume of 0.5 in.³ and 1.0 in.³ are also shown. The power density of the discharge increased as the total discharge power increased. The highest power density of 328 kw/in.³ occurred at a discharge pressure of 8.5 atm, an argon weight flow rate of 0.041 lb/sec, and a total discharge power of 180.5 kw.

Note that, due to the strong influence of argon weight flow rate on reducing the discharge diameter, the maximum power density occurred at a moderate pressure level but maximum argon weight flow rate. The maximum power density achieved was limited solely by the operating capability of the 1.2-megw r-f induction heater. Corporate-sponsored tests using salt water to mock-up the impedance of the plasma load were conducted throughout the test program to establish the operating limits of the 1.2-megw r-f induction heater. These tests are used to verify the similarity of load characteristics and permit r-f system component check-outs without the plasma radiant energy source present. High-power salt water tests conducted late in the program indicated the occurrence of overheating of the vacuum capacitors in the resonator section (see Fig. 3). Therefore, until additional systematic tests can be completed to determine

the sources of overheating, an upper operating limit on resonator voltage was assigned to the radiant energy source test program. The combination of test parameters used in many of the high-power tests resulted in a resonator voltage closely approaching this upper operating limit. Consequently, the majority of high-power tests were restricted to operation within this limit. Future increases in power density can be expected as the discharge power is increased and the argon weight flow rate is increased simultaneously to reduce the discharge diameter.

It is of interest to compare the maximum power deposited into the argon plasma discharge and the discharge power density with those in the r-f tests of Refs. 3 and 8. For the tests reported herein, the maximum power deposited into the plasma discharge and the maximum power density were 216 kw and 328 kw/in.³, respectively. For the results described in Ref. 3, (the preceding UARL program under Contract NASw-847), the corresponding levels were 85 kw and 220 kw/in.³, respectively. From Ref. 8, the corresponding levels for pure argon discharges were approximately 405 kw and 28 kw/in.³. This power density was calculated using data in Ref. 8 and assuming a cylindrical discharge with a diameter and length equal to 75 percent of the 3.5-in. torch diameter. Higher power levels (approximately 609 kw, but at a power density of only about 6.4 kw/in.³) were obtained by employing various gas mixtures and larger diameter torches (see Ref. 8). This comparison illustrates the significant progress made in the present program in depositing a large amount of r-f power into a very small volume plasma.

Discharge Radiant Energy Flux

Calculations of ϕ_R , the radiant energy flux at the surface of the discharge, were made for the data shown in Figs. 12 and 14. The results are shown in Fig. 15. The radiant energy flux is defined as the total radiated heat transferred through the inner peripheral wall of the test chamber (see Fig. 13) divided by the discharge surface area. For the data reported herein, the total radiated power $Q_{R,T}$ in kw is defined as

$$Q_{R,T} = Q_R + Q_W - Q_C \quad (2)$$

where Q_R is the radiated power as measured by the radiometer, Q_W is the power deposited in the peripheral-wall coolant, and Q_C is the power conducted through the inner peripheral wall. Since Q_C was not measured directly, estimates of Q_C were made by calculating the maximum heat which could be conducted through the inner peripheral wall. Experience has indicated that rapid cooling of the fused silica tube from temperatures in excess of 2250 R will induce residual stresses which can be easily seen when viewed under polarized light. Examination of the inner fused silica peripheral wall used in the high power tests showed only slight traces of residual stress. Thus, it was assumed that during the highest power tests the inner surface of the peripheral wall did not exceed 2250 R. In addition, there was no indication of severe

heating of the peripheral wall or boiling of the water-dye coolant in the annulus for any of the tests. It was further assumed that the effective surface area for conduction heat flow is governed by the tube periphery and a length in the axial direction of 3.0 in. The discharge major axis is only 2.0 in., but it is believed that convective heating of the peripheral wall will occur over a slightly longer length. Based on these assumptions, the maximum Q_C was calculated to be equal to about 9 kw. To be conservative, this value of Q_C was used (see Eq. (2)) for all data from tests having $Q_T \geq 100$ kw. Further, Q_C was assumed to be negligible for all total discharge powers below 100 kw. Future tests are planned in which simultaneous measurements of total heat flux and radiation incident on the inner fused silica tube will be made.

The highest level of radiant energy flux achieved was 36.7 kw/in.^2 which corresponds to an equivalent black-body radiating temperature, T^* , of 10,200 R. Equivalent black-body radiating temperatures corresponding to the radiant energy fluxes for other test data are also shown on Fig. 15.

A comparison can be made between the experimental results from the 1.2-megw r-f induction heater tests with the radiation flux levels desired for simulation of the thermal radiation from a full-scale nuclear light bulb engine. Figure 16 shows the variation of total radiation from the source with discharge diameter. The source was assumed to be ellipsoidal in shape with a major axis of 2 in. The upper and lower dashed lines correspond to the design radiant flux levels of the reference and derated reference engines, respectively. Also shown are the corresponding equivalent black-body radiating temperatures. The cross-hatched area on the figure indicates the envelope of experimental test results. The maximum radiation heat flux obtained to date, corresponding to a total radiation from the source of 156 kw, is shown by the open symbol. This value corresponds to a flux of 36.7 kw/in.^2 , with a corresponding equivalent black-body radiating temperature of 10,200 R, and is approximately 20 percent of the value required to simulate the full-scale reference engine (Ref. 1). However, a full-scale engine would still be extremely attractive even if the radiant flux levels were lower than those of the reference engine. The maximum radiation flux level achieved to date is 2.55 times the design flux level for the derated reference engine.

Effects of Pressure on Radiant Energy Source Characteristics

Effects of Pressure on Power Loss Mechanisms

Tests were conducted to determine the effect of chamber pressure on the power loss mechanism from the plasma discharge by attempting to hold all variables, except chamber pressure, approximately constant. It was not possible to do this and still maintain a satisfactory discharge except over a limited range of flow conditions because the geometric characteristics of the plasma discharge in a vortex flow field

depend on the coupling between the discharge and the electric and magnetic fields producing the discharge. In addition, the thermal and electrical characteristics of r-f plasma depend on the combined mechanisms of heat dissipation to the surroundings. The results of these tests are shown in Fig. 17. The results illustrate the effect of chamber pressure over the range 3 to 15 atm on the fraction of power removed by conduction and convection losses. This fraction is equal to the quantity, total discharge power, Q_T , minus the total radiated power, $Q_{R,T}$, divided by Q_T . Data for two values of argon weight flow rate are shown. The range of total discharge power was from 50 to 116 kw. During these tests, the saturable reactor controls of the r-f system were adjusted to maintain a constant power-amplifier d-c supply voltage. As the chamber pressure was raised above 3 atm, the total discharge power increased. A relatively small, but monotonic, decrease in discharge diameter accompanied this pressure increase. At the level of 15 atm, the total power into the discharge reached 116 kw. As expected, increases in pressure resulted in a substantial decrease in the fraction of total discharge power lost by conduction and convection. The fraction of power removed by conduction and convection losses over the data range was reduced by approximately a factor of two from the initial value of 0.44. The relationship appears to be logarithmic over the range of tests reported. This is encouraging in light of the overall objective of operating the r-f plasma discharge in a radiation-dominated mode. The maximum pressure in any test conducted during this program was 16 atmospheres. This limit was predicated on the equipment considerations discussed previously. Further increases in discharge pressure above 20 atm are possible in future tests (see Appendix A).

The effect of increasing the total discharge power on the fraction of power removed by conduction and convection losses at nearly constant pressure ($P_D = 5$ to 6 atm) is shown in Fig. 18. These data are for a wide range of argon weight flow rates (0.010 to 0.028 lb/sec). For reference, lines of constant conduction-convection losses are shown by the dashed lines in Fig. 18. The data indicate that the fraction of power removed by conduction and convection losses decrease as both total discharge power and argon weight flow rate were changed.

Radiated Power in Various Wavelength Bands

A series of tests were conducted to permit comparisons of the power radiated through the peripheral wall in various wavelength bands with and without the addition of dye. The tests could not be conducted at high power levels because the inclusion of dye into the peripheral-wall coolant was necessary to protect the surrounding equipment and test tank. Results of typical tests are presented in Fig. 19. During these tests, 800 ppm of nigrosine dye was added to the peripheral-wall cooling water. The bar graph in Fig. 19 (a) shows the reduction of total radiated power due to the addition of dye. Fig. 19 (b) shows the distribution of radiated power in the various wavelength bands. A significant portion of the total radiated power appears in the 0.72-to-1.3-micron wavelength band. It is expected that, as higher power and pressure

levels are reached in future tests, significantly more of the radiated power will shift to lower wavelengths, particularly between 0.72 to 1.0 micron. The addition of seed material into the plasma discharge can be used to shift the emission spectrum of the r-f plasma discharge (Ref. 9).

Radial Distribution of Temperature

To obtain an estimate of the average temperature in the central portion of typical discharges, spectral emission measurements were made using the optical system shown in Fig. 6. The optical system was calibrated using the Eppley Laboratory Calibrated Standard of Spectral Irradiance. The absolute value of the plasma continuum radiation was measured along a diameter of the plasma at a wavelength of 4140 Å. By assuming thermodynamic equilibrium, the average temperature of the plasma along a diameter was determined from the continuum radiation measurements using the methods described in Ref. 4 for relating the continuum intensity to the temperature. The monochromator was also positioned on the maximum intensity of the Argon I 4158.59 Å line and scanned across the plasma. The Argon 4158.59 Å line was selected, as opposed to the Argon 7635 Å spectral line used in Ref. 3, because of the possible effects of self-absorption. A machine program employing the Abel inversion method was used to convert the measured chordal intensities to radial intensities. From the known temperature along a diameter and the Boltzmann equation, the relationship between the line intensity and the temperature is determined. Then, from the inverted radial intensities, the radial temperature distribution is determined. A more complete description of this method and the associated data reduction techniques is presented in Ref. 4.

Figure 20 shows two typical radial distributions of temperature that were obtained. The temperature profile shown by the dashed line corresponds to a relatively low-discharge-power, low-chamber-pressure, test condition (60 kw and 4 atm, respectively). The solid line corresponds to an approximate factor-of-two increase in both the power and pressure. For reference, the representative discharge radius is shown for both cases, as determined by the technique discussed previously. The peak temperature for the 60 kw case was 18,700 R and occurred off the axis at approximately the mid-radius. The peak temperature for the 120 kw case was 19,550 R. Similarly, the peak temperature occurred at approximately mid-radius. The occurrence of an off-axis peak can be attributed to the mechanism of power deposition (in an r-f discharge power is deposited in an annulus). For reference, the value of the intensity-average temperature, T_{AV} , of 18,500 R corresponding to the 120 kw case is denoted by the solid line in Fig. 20. This temperature was calculated from an integrated average intensity using the relationships determined between temperature, intensity, and radius. The relatively small change in discharge temperature over the wide range of discharge powers and pressures shown by these results and those reported in Refs. 3 and 4 make it worthwhile to compare the experimental and the theoretical radiated power per unit volume with temperature for an argon plasma. The results of this comparison for the

120-kw (7 atm) case are shown in Fig. 21. The procedure outlined in Ref. 7 was used to obtain the curves shown in Fig. 21. This figure clearly shows a steep slope in the radiated power per unit volume versus temperature curves with pressure as the parameter. However, the values of the radiated power density shown now include the contributions due to both the continuum and line radiation between 0.3 and 1.0 microns. At the value of radiated power density corresponding to this case, an approximate temperature difference of 2000 R exists between the calculated and the measured temperatures. Separate calculations were also made to estimate the degree of self-absorption which was present in the range of the test results reported for the 4158.59 Å line. These calculations indicate that, even at the highest pressures and temperatures produced in the current tests, that negligible self-absorption would occur. Further radiant energy source tests should employ diagnostic probes to permit direct side-on viewing of the r-f plasma discharge. This will permit direct determination of the radiant heat flux. In addition, spectral measurements, particularly in the far ultra-violet, are necessary to provide additional information on the transmission characteristics of fused silica in this wavelength band.

Simultaneous simulation of full-scale nuclear light bulb engine operating pressures and radiant heat fluxes may require r-f plasma test equipment capable of a 500-atm operating environment (see Appendix A).

SECTION IV

TRANSPARENT-WALL MODEL PROGRAM

Objectives of Program

The primary objective of the transparent-wall model program was to develop and test internally cooled transparent walls (such as the ones shown in Fig. 22) similar to those which might be employed in a nuclear light bulb engine. The walls of the engine must be highly transparent to allow the thermal radiation to reach the propellant with a minimum of absorption. They must be cooled to remove heat deposited by radiation, conduction, and convection. The transparent walls must also have provision for tangential gas injection to provide a radial-inflow vortex flow field. The radial-inflow vortex flow serves to contain the gaseous nuclear fuel and to isolate it from the transparent wall. Emphasis in this program was directed toward (1) development of fabrication techniques for models having wall thicknesses of approximately 0.005 in. and (2) testing of a number of these models in the 1.2-megw r-f induction heater to determine their operating limitations. A description of the model fabrication techniques which were employed in this program and discussions of the test procedures and results obtained in the model tests are presented in the following three subsections.

Model Fabrication Techniques

Models With Axial Coolant Tubes

The major problems associated with fabrication of transparent-wall models are (1) sealing the thin, transparent coolant tubes into the coolant manifolds, (2) insuring that adequate cooling flow is provided throughout the model (especially for those parts of the model which are not transparent to thermal radiation), and (3) insuring that the completed model configuration can be routinely handled and installed in the 1.2-megw r-f induction heater for testing.

Sealing the thin, transparent coolant tubes into the coolant manifolds was difficult because (1) it was desired to have the individual coolant tubes as close to each other as possible and (2) the number of sealant materials which are compatible with fused silica, copper or aluminum, and the r-f environment is limited. The coolant-tube sealing techniques that were evaluated include fusing coolant tubes into coolant manifolds and potting the coolant tubes into copper or aluminum coolant manifolds using silicone rubber and epoxy sealants.

The technique of fusing coolant tubes into fused silica manifolds was used successfully in fabricating the 0.020-in.-wall-thickness models described in Ref. 3. This technique involves locally heating the ends of the coolant tubes to a temperature slightly less than the softening temperature of fused silica (approximately 3500 R) and then pushing the tubes into a fused silica manifold which has been preheated to a slightly higher temperature. A pulse of air is applied through the tubes when they are pushed into the manifold. This process of "blowing" the coolant tubes into the manifolds produces a completely fused structure. Successful application of this technique requires precise control of both the coolant tube and manifold temperatures. Several transparent-wall models having 0.010-in. wall thickness were fabricated using this technique. However, careful inspection of some of these models after fabrication showed that small cracks existed in some coolant tubes near the point where the coolant tube joined the coolant manifold. It is believed that these cracks resulted from thermal stresses induced in the model due to differences in the rate of cooling for coolant tubes and coolant manifolds. The thin-walled coolant tubes cool very rapidly relative to the thick-walled coolant manifold. Although it was sometimes possible to repair the cracked tubes by reheating the model to the fusion temperature, it was generally concluded that, without more precise control of the heating and cooling process, the technique of fusing was impractical for use in fabricating models with 0.010 and 0.005-in. wall thickness.

The second coolant-tube sealing technique which was evaluated consists of potting the fused silica coolant tubes directly into copper or aluminum manifolds. Numerous silicone rubber and epoxy sealants were used. Pourable, self-leveling silicone rubber (RTV-112, manufactured by the General Electric Co.) was found to have the best combination of adhesive, temperature, and electrical characteristics of the materials tested. It was also found that curing the silicone rubber at temperatures of approximately 200 to 300 F was necessary to achieve a leak-tight seal between the coolant tubes and the coolant manifold. Figure 22a, a photograph of a 1.26-in.-ID axial coolant-tube model, shows details of the coolant-tube seal. This model consists of 39 0.040-in.-ID by 0.060-in.-OD fused silica coolant tubes and 3 0.1275-in.-ID by 0.1875-in.-OD copper vortex injectors equally spaced around the circumference of a 1.26-in.-dia circle. A photograph of a 0.95-in.-ID axial coolant tube model is shown in Fig. 22b. This model consists of 42 0.040-in.-ID by 0.050-in.-OD fused silica coolant tubes and 3 0.1275-in.-ID by 0.1875-in.-OD copper vortex injectors equally spaced around the circumference of a 0.95-in.-dia circle. This particular model was used in the simulated propellant heating tests discussed in Section V. The copper shrouds located at each end of the model were intended to provide a smooth transition for the simulated propellant stream. For both types of models, the copper vortex injectors were soldered to the copper manifold at both ends to form a rigid structure. The fused silica coolant tubes were potted into this structure. Each vortex injector tube had 23 0.020-in.-dia injection holes equally spaced at an injection angle approximately 11 deg from the tangent. The separation of the holes was approximately 1/16 in.

This potting technique has been used for fabrication of models similar to those shown in Fig. 22a having both 0.010 and 0.005 in. wall thickness.

In some models, the distance between adjacent cooling tubes was reduced by using manifolds in which the coolant tubes were potted in annular passages rather than in individual holes. The coolant manifolds are split to allow sealing of the coolant tubes from inside the manifold. The technique of potting the coolant tubes into the coolant manifold was found to be the most satisfactory of the two techniques which were evaluated and was used for all of the models employed in the tests in the 1.2-megw r-f induction heater.

Models With Circumferential Coolant Tubes

As described in Ref. 1 and shown in Fig. 1b, the transparent wall in a unit cavity of the reference nuclear light bulb engine is 6 ft long and 1.6 ft in diameter. In an actual engine, the coolant tubes would probably be arranged in a circumferential fashion to satisfy thermal, structural and support requirements. An investigation was conducted to develop techniques for fabricating thin-walled circumferentially cooled models. Fabrication of a circumferentially cooled model requires several steps in addition to those used in fabricating models with axial coolant tubes. The additional steps can include cutting, bending, and coiling of thin-walled fused silica tubing, depending on the method of fabrication which is employed. A description of two fabrication techniques which were evaluated is presented in the following paragraphs.

Circumferentially cooled model components were fabricated from fused silica tubing which had been previously wound into coils. The coils were cut in half along their lengths and then heated and bent into the desired shape (as described in Ref. 3). The bent ends were "blown" into manifolds using the same techniques that were used in fabricating models with axial coolant tubes. The circumferential coolant tubes were 0.040-in.-ID by 0.080-in.-OD. Three 120-deg segments were combined to form the circumferentially cooled model configuration shown in Fig. 23a. Peripheral-wall vortex injection tubes could be located between the circumferential coolant manifolds at 120-deg intervals.

A second configuration shown in Fig. 23b was fabricated by potting previously bent 0.020-in.-wall thickness fused silica tubes into copper manifolds with epoxy sealant. Ten 0.040-in.-ID by 0.080-in.-OD fused silica injector tubes were bent to permit tangential injection and were also potted into copper manifolds with epoxy sealant. Additional techniques for coiling and bending thin-walled glass tubing are required before circumferential models having wall thicknesses of 0.005 in. can be fabricated. Initial attempts at forming the desired bends in thin-walled coolant tubes often resulted in collapsed or restricted tubes and nonuniform tube shapes.

Test Procedures

As discussed previously, all of the models employed in tests in the 1.2-megw r-f induction heater (see summary in Table I) were fabricated by potting the fused silica coolant tubes directly into the coolant manifolds. Prior to installing a model into the 1.2-megw r-f induction heater, a number of preliminary tests were performed. The model was pressurized to approximately 20 psig for approximately 20 minutes with water to insure that there were no large leaks in model seals or coolant tubes. (Small leaks of 3 to 4 drops/min were considered tolerable). Next, the model was mounted on the end walls (see following subsection) and the argon and water coolant lines were connected. The model was then pressurized once again. Following the second pressure check, the model assembly (including end walls, argon and water coolant lines, and simulated propellant inlet and exhaust ducts when used) was installed in the 1.2-megw r-f induction heater. After installation, a final pressure check of the complete model configuration was made. During an actual test, a pressure differential of less than 20 psig across the model coolant tubes was maintained by varying the model water coolant and test chamber pressures. Both the water coolant flow and argon injection flow ducting had inlet and exhaust throttle valves to independently control pressure and flow rate.

Discussion of Models and Test Results

Tests were conducted in the 1.2-megw r-f induction heater to determine the heat transfer characteristics and operating limitations of several different transparent-wall model configurations. The axial boundaries of the r-f plasma discharge were formed by two 0.625-in.-dia water-cooled copper end walls which were spaced 2.0-in. apart. The argon vortex flow was withdrawn through 0.075-in.-dia thru-flow ports located on the centerline of each end wall (refer to Section III). The primary variables in these tests were the r-f discharge power, argon injection flow rate, and chamber pressure. The configurations tested include models similar to that shown in Fig. 22a having both 0.010 and 0.005-in. wall thickness and models similar to that shown in Fig. 22b with 0.005-in. wall thickness.

Tests With 1.26-in.-ID Axial-Coolant-Tube Models

A 1.26-in.-ID axial-coolant-tube model is shown installed in the 1.2-megw r-f induction heater in Fig. 24a. Models of this type were operated at total discharge power levels up to 55.3 kw. A photograph of the plasma discharge during a typical test condition is shown in Fig. 24b. Due to multiple reflections from the axial coolant tubes, the shape of the discharge is not readily determined. A breakdown of the power losses from a typical test is shown in Fig. 25. For this test, a total of 51.3 kw was deposited into the plasma discharge; of this, 25.3 kw, or approximately

55 percent, was deposited into the model coolant and 1.19 kw, or 2.6 percent, was deposited into the vortex injector bypass coolant flow. The total power radiated was 19.54 kw, or 38.1 percent, as measured by the radiometer and determined from the annular coolant flow heat balance (nigrosine dye was added to this coolant flow to attenuate the radiation). The remaining 5.37 kw was deposited in the end-wall coolant and thru-flow exhaust gases.

The variation of power deposited into the model coolant tubes with total discharge power is shown in Fig. 26. These data (open symbols) were obtained in tests employing models having coolant wall thicknesses of 0.010 in. and 0.005 in. Also included for comparison is the line representing the ratio $Q_{CO}/Q_T = 0.5$ where Q_{CO} is the power deposited in the cooling water of axial-coolant-tube model and Q_T is total discharge power. The data indicate that between 45 and 55 percent of the total power was deposited into the model due to the combined effects of conduction, convection, and radiation.

Tests With 0.95-in.-ID Axial-Coolant-Tube Models

The 0.95-in.-ID axial-coolant-tube model is shown installed in the 1.2-megw r-f induction heater in Fig. 27a. Models of this type were operated at total discharge power levels up to 16.6 kw. It was determined that the distance between the fused silica tubing and the copper shrouds for the propellant heating experiments (Section V) was too small and often resulted in broken coolant tubes when the shrouds were placed on the model. For the tests reported in this section, the model configuration did not include these shrouds.

A photograph of the plasma discharge during a typical test is shown in Fig. 27b. As discussed previously, the shape of the discharge is not readily determined due to multiple reflections from the axial coolant tubes. A breakdown of the power losses from the discharge is shown in Fig. 28 for a typical test. For this test, a total of 16.6 kw was deposited into the plasma discharge; 10.35 kw, or approximately 62 percent, was deposited into the model coolant and 0.21 kw, or 1.26 percent, was deposited into the vortex injector bypass coolant flow. The total power radiated was 3.58 kw, or 21.6 percent, as measured by the radiometer and determined from the annular coolant flow heat balance. Due to the low radiation level, the addition of nigrosine dye to the annular cooling water was not necessary. The remaining 2.46 kw power was deposited into the end-wall coolant and thru-flow exhaust gases. The variation of power deposited into the model coolant tubes with total discharge power is shown in Fig. 26. For these data (see closed symbols), between 50 and 80 percent of the total power was deposited into the model. The increased percent of power deposited into the model, Q_{CO}/Q_T , for tests with seeded simulated propellant flow (see Section V) over that obtained in tests without seeded simulated propellant flow is probably due to one or

all of the following causes. Seed coating on the model resulted in more of the total radiation deposited in the model; the introduction of a stream of seeded simulated propellant flow around the model increased the convective heat load to the model. This is shown in Fig. 29 when the data before seeds are introduced (flagged solid symbols) are compared with the data after the seeds are introduced (solid symbols). Also, the smaller diameter (0.95 in.-dia as compared with 1.26 in.-dia) of the models used in tests with simulated propellant flow means that the absolute distance between the discharge and the wall of the model is probably reduced, thereby causing an increase in the amount of heat conducted to the model.

Comparison of Operating Conditions of Full-Scale Engine, R-F Plasma Radiant Energy Source And Models

A summary of the physical dimensions and operating conditions of the models employed in the tests is given in Table IV. Also shown in Table IV are corresponding physical dimensions and operating conditions for the reference nuclear light bulb engine, for a derated nuclear light bulb engine and for the highest power radiant energy test obtained in the 1.2-megw r-f induction heater.

A comparison of the model wall heat deposition rate obtained in the tests with those expected in the reference and derated nuclear light bulb engines is shown in Fig. 29. For some of the data corresponding to tests without simulated propellant flow (open symbols), the heat deposition rate per unit area was greater than that expected in the derated engine. The coolant tube area that was exposed to the plasma discharge was assumed to be equal to the circumference times the coolant tube length for each tube (i.e., the number shown in Table IV). For the reference engine (see Table IV), 218 Btu/sec-ft² would be deposited into the fuel side of the transparent wall due to the combined effects of radiation, conduction, and convection. The maximum heat deposition rate obtained in the model tests was 300 Btu/sec-ft² for a model having a wall thickness of 0.010 in. This heat deposition rate per unit area is equal to 1.24 times the heat deposition rate per unit area expected from the fuel side in the reference nuclear light bulb engine. However, the heat deposited into the fuel side of the transparent wall in the reference engine is predominantly due to radiation which is deposited at or near the surface of the transparent wall. The heat deposited in the model tests was predominantly due to conduction and convection from the discharge which is deposited at the surface of the transparent wall. Additional model tests should be conducted in which the proportion of heat deposited due to radiation is increased; this will more closely simulate the conditions expected in the reference engine.

Tests conducted with the 0.95-in.-ID model resulted in heat deposition rates per unit area that are less than those expected in the nuclear light bulb engine

(see Fig. 29, solid symbols). In this case, the coolant tube area exposed to both the internal plasma discharge and the external simulated propellant flow (see Section V) was assumed to be equal to the circumference times the length for each tube (see Table IV), since the model received heat from both the plasma side and the simulated propellant-stream side. It was not possible to separate the effects of fuel-side heating from simulated propellant-side heating during these tests.

Heat Transfer Limitation in Model Tests

The maximum discharge power was limited by heat transfer which caused buckling and localized melting of the copper vortex injectors. In future tests employing models of this type, steps must be taken to provide additional cooling to the vortex injectors. Results of tests conducted late in the program indicate that the addition of water cooling to the vortex injectors should significantly increase their heat transfer capability. These tests were conducted with a fixture designed to simulate the mechanical attachment and the thermal conditions that each copper vortex injector was operated at in actual tests. Heat from a calibrated oxy-acetylene torch was applied to the central 2-in. portion of the injector tubes for 15 sec. The torch flame temperature at the test location was approximately 1200 F. Argon flow rates identical to those employed in actual transparent-wall model tests were used. Buckling occurred in the central portion of the copper injector tube due to thermal expansion when both ends of the injector were held fixed. To determine the magnitude of the expansion prior to buckling, a second test was conducted in which one end of a copper injector tube was allowed to freely expand in the axial direction. All other conditions of applied heat and argon flow rates were the same as in the previous test. With the argon flowing, less than 0.005-in. displacement was measured using a dial indicator mounted at the free end of the injector. When the argon flow was turned off an axial displacement of 0.035 in. was measured. The displacement returned to the original 0.005 in. as soon as the argon flow was re-established. A third test was conducted with a 1/16-in.-OD copper tube soldered to the back of a copper vortex injector (i.e., the side away from the flame). Water (approximately 0.005 gpm) was passed through the 1/16-in.-OD copper tube. All other conditions of applied heat and argon flow rate remained the same as in the first tests. One end of the copper injector tube was again allowed to freely expand. With the water cooling, negligible axial expansion was indicated. In addition, temperature-sensitive paint (Tempilaq) located at various points on the injector tube indicated relatively low temperatures (less than 200 F) surrounding the central 2-in. high-heat flux region.

SECTION V

INITIAL SIMULATED PROPELLANT HEATING PROGRAM

Background

In the nuclear light bulb engine, thermal radiation from the hot nuclear fuel is transferred through an internally cooled transparent wall to seeded hydrogen propellant. Figure 1a is a sketch of a unit cavity of the nuclear light bulb engine. The reference engine is formed by a cluster of seven such cavities to increase the effective radiating surface area of the nuclear fuel cloud. Seeded hydrogen propellant flows through the annular region surrounding the transparent wall. Figure 1b is a sketch showing dimensions of a unit cavity for the reference engine. For simplicity, only one half of the rotationally symmetric cavity is shown. The propellant region is a divergent annulus 6-ft long with a 1.636-ft inside diameter. The annulus width increases uniformly from 0.093 ft at the inlet to 0.502 ft at the exhaust.

In the reference engine, 98 percent of the total thermal radiation incident on the propellant stream is absorbed by the hydrogen propellant. Hydrogen is essentially transparent to thermal radiation at the engine operating pressure of 500 atm and below a temperature of approximately 14,000 R. Therefore, a seed material must be added to the propellant stream to provide the required opacity. The ideal seed material would consist of nonreactive, high-melting-point, high-boiling-point, sub-micron-sized metal seed particles that exhibit good absorption characteristics in both the particle and vapor forms. Sub-micron-sized particles, low-ionization-potential metal vapors, and various polyatomic gases have been examined theoretically and experimentally as possible seed materials for the propellant stream (Refs. 10 through 17). Sub-micron-sized solid or liquid particles exhibit essentially continuous spectral absorption characteristics as contrasted with discrete spectral absorption characteristics exhibited by low-ionization-potential metal vapors and polyatomic gases. Theoretical studies (Refs. 10 through 18) of the absorption properties of small solid particles have been based on the Mie theory. This theory describes the spectral extinction, absorption, and scattering of radiation by spherical particles as a function of particle size, material properties, and the wavelength of the incident radiation. The results of these studies indicate that tungsten is attractive as a seed material because of its high melting point, high boiling point, and low reactivity with hydrogen. In the reference engine, 0.05-micron-dia tungsten particles are assumed to be used as a propellant seed material.

In each unit cavity the inner wall of the propellant annulus is transparent. The outer wall is highly reflecting to reduce the heat load to the moderator and to increase the effective radiant energy path length in the propellant region. A thin layer of unseeded gas flows adjacent to both the inner and the outer walls of the propellant region. These thin unseeded layers serve as buffer regions which prevent the degradation of the optical properties of the walls due to partial coating by the propellant seed. They also keep hot gas away from the walls, reducing the heat transfer to the duct walls.

The radiant heat flux levels at the surface of the nuclear fuel are 177.8 kw/in.² for a reference engine and 14.4 kw/in.² for a derated engine (see Table IV). These flux levels correspond to equivalent black-body radiating temperatures of 15,000 R and 8,000 R, respectively. For the reference engine, the inlet conditions in the propellant region are: a velocity of 35.5 ft/sec, a temperature of 4,050 R, and an enthalpy of 1.55×10^4 Btu/lb. The corresponding exhaust conditions are: a velocity of 23.7 ft/sec, a temperature of 12,000 R, and an enthalpy of 1.033×10^5 Btu/lb (see Ref. 1). The hydrogen weight flow rate per unit cavity is 6.04 lb/sec. The seed weight flow rate is equal to 3 percent of the hydrogen weight flow rate. The hot propellant from the cluster of seven unit cavities will exhaust into either a single common nozzle or a multiple nozzle system.

Objectives of Program

The tests discussed in this report represent a first attempt at UARL to simulate the heating of the propellant stream in the nuclear light bulb engine. The objectives were: (1) to develop methods for injecting solid particle seeds into a simulated propellant stream, (2) to study the effectiveness of buffer layers for preventing wall coating, and (3) to absorb a large percentage of radiation in the simulated propellant stream, leading to maximum propellant temperature rises due to absorption of thermal radiation.

Description of Equipment

Seed Dispersal System

Figure 30 is a schematic diagram of the simulated propellant flow system and high-pressure seed dispersal system. The seed dispersal system consists of a 5.0-in.-ID by 11.75-in.-deep, high-pressure (3,000 psi), stainless steel canister.

However, for the tests reported herein, the maximum canister pressure was considerably lower than 3,000 psi. Carbon particles (nominal diameter of 0.01 microns) were placed in the lower portion of the canister (approximately 2/3 full). Carbon seed material was used in the initial tests instead of tungsten because it is inexpensive, readily available, easier to handle and disperse than tungsten, and its properties and optical characteristics over the size range of interest are well known. The carbon was dispersed within the canister by rotating agitator blades located in the upper portion of the canister. The agitator blades were driven at a rotational speed between 2,140 rpm and 2,140 rpm using a variable-speed motor. Argon was passed through the canister, entraining dispersed carbon particles with it. The argon gas entering through the top face of the canister also helped to agitate the carbon powder through aerodynamic forces. The ratio of total argon weight flow rate to carbon weight flow rate was controlled by allowing some of the total argon carrier flow to bypass the canister (see Fig. 30). The carbon weight flow rate could also be varied by changing the rotational speed of the agitator blades. The seeded argon flow line was connected to the plenum of the seeded gas injection duct in the simulated propellant flow chamber. For the typical carbon seed weight flow rates used in the tests, the capacity of the canister was sufficient to permit total test times of approximately 20 min before the carbon supply was depleted. Two argon flow lines for the separate buffer layers were also connected to their respective plenums in the simulated propellant flow chamber. Individual pressure regulators, pressure gauges, control valves, and flow metering equipment were used for each system. Argon flow rates were measured with variable-area rotameters. See Fig. 31 for a photograph of the high-pressure seed dispersal system and control consoles.

Cold-Flow Configurations

Figure 32 is a schematic of the initial configuration used for cold-flow simulated propellant experiments. The propellant duct consists of an annulus formed by two concentric fused silica tubes. The inner diameter of the annulus was 1.37 in., the outer diameter was 2.40 in., and the duct length was 7.4 in. Seeds were to be introduced into the propellant stream through a series of 120 hypo-tubes located on the circumference of a 1.885-in.-OD circle. The hypo tubes had a 0.020-in.-ID and were 1.5-in. long.

A schematic of the configuration used to test the introduction of seed material into the simulated propellant stream through a slot is shown in Fig. 33. The simulated propellant duct was 4.0-in. long, 0.273-in. wide, and 3.0-in. deep. The parallel sidewalls were 0.25-in.-thick lucite plates, 4.0-in. long by 3.0-in. deep, spaced 0.273-in. apart. Argon seeded with carbon particles was introduced into the test section through a 0.039-in.-wide slot. Unseeded argon was introduced between the seeded gas slot and the lucite walls. The buffer layer thickness was 0.117 in.

Propellant Heating Configuration Used With D-C Arc Heater

D-C Arc Heater

The d-c arc heater was constructed in 1968 as part of a UARL Corporate-sponsored program. Figure 34 is a schematic diagram showing the primary components of the heater facility. Figure 35 shows the current and voltage operating range of the d-c power supplies together with the results of tests employing an argon arc operating at approximately 1.0 atm pressure. A detailed description of the d-c arc heater components and operating characteristics is presented in Appendix C. The basic heater configuration consists of a vortex stabilized d-c arc enclosed within concentric water-cooled fused silica tubes. The configuration used in propellant heating tests is shown in Fig. 36.

The arc has been operated at radiation levels up to 45.0 kilowatts in the 3.0-in.-long test section. Figure 37 is a plot of the power radiated through the 3-in.-long test section as a function of the total power deposited in the arc for a 3-in.-long test length.

Concentric-Coolant-Tube Model Configuration

The propellant heating test section was a 3.0-in.-long annular duct surrounding the water-cooled fused silica tubes (see Fig. 36 and Table I). The inside wall of the simulated propellant duct was a fused silica tube with a 1.69-in. OD. The outer wall of the duct was a fused silica tube with a 2.24-in. ID. The seed was introduced into the propellant stream through a 0.039-in.-wide annular slot. Buffer layers of unseeded argon were introduced between both the inner and outer fused silica walls and the central seeded gas stream. The buffer layers were 0.118-in. wide. For these tests, the d-c arc was 10.25-in. long from cathode to anode.

Propellant Heating Configurations Used With The 1.2-Megw R-F Induction Heater

Concentric-Coolant-Tube Model Configuration

Propellant heating tests using the 1.2-megw r-f induction heater as the radiant energy source were conducted with two types of transparent walls separating the propellant stream from the plasma discharge region (see Table I). The first type was a concentric-coolant-tube model (Fig. 38). This model consisted of two concentric fused silica tubes with a water cooling annulus between them. The dimensions of the inner tube were 1.06-in. ID by 1.18-in. OD, and those of the outer tube were 1.26-in. ID by 1.42-in. OD. In this configuration the vortex was driven by eight

0.054-in.-ID stainless steel vortex injector tubes located at one end of the model. The axial boundaries of the r-f plasma discharge are formed by the two 0.625-in.-dia water-cooled copper end walls which were spaced 2.0 in. apart. Argon was withdrawn through 0.075-in.-dia through-flow ports located on the centerline of each end wall.

The simulated-propellant heating duct surrounded the transparent-wall model. The outer wall of the propellant duct was water-cooled and consisted of a 2.24-in.-ID by 2.40-in.-OD fused silica tube. The water cooling annulus for the outer wall was formed by a concentric 2.54-in.-ID by 2.88-in.-OD fused silica tube. The test section, shown in Fig. 38, is 7.38-in. long and extends from the seed inlet to the downstream end of the transparent-wall model. Seeded argon was introduced into the test section through a 0.039-in.-wide annular slot. A buffer layer, 0.118-in. wide, of unseeded argon was introduced between the outer fused silica wall of the propellant duct and the central seeded argon stream. A second buffer layer, 0.253-in. wide, was introduced between the inner fused silica wall of the propellant duct and the central seeded argon stream.

Axial-Coolant-Tube Model Configuration

The second configuration for simulated-propellant heating tests in the 1.2-megw r-f induction heater used a 0.095-in.-ID axial-coolant-tube model (see Fig. 39 and Table I) between the plasma discharge region and the propellant duct. A description of the 0.095-in.-ID axial-coolant-tube model including dimensions, fabrication techniques, and performance during these tests was presented in Section IV. A photograph is shown in Fig. 22b. The axial coolant tubes of the transparent-wall model formed the inner wall of the simulated propellant duct. The outer wall and simulated propellant injector were identical to those of the configuration used with tests employing the concentric coolant-tube configuration. However, the axial-coolant-tube model had an outer diameter of 1.05 in., compared to an outer diameter of 1.42 in. for the concentric-coolant-tube model. Therefore, the buffer layer on the inside wall of the axial-tube models was thicker than for the concentric-coolant-tube models. The inner buffer with the axial-tube model was 0.438-in. thick.

Test Procedures

D-C Arc Heater

The following sequence of events was used during a typical test employing the d-c arc heater: (1) start motor-generators, (2) start all diagnostic and recording equipment, (3) start ventilators, cooling water, and gas flows and adjust to the desired operating conditions, (4) index the auxiliary starting electrode until it contacts the cathode, (5) activate the auxiliary starter system, (6) record all data at a particular test condition, (7) turn off arc power after completion of run.

Cold-Flow Tests

For the cold-flow tests the argon for both the buffer layers and the seed carrier flow were turned on. The argon seed carrier flow was adjusted for full bypass of the seed dispersal system (Fig. 30). The flows were adjusted such that the average velocities of each of the three streams were matched.

A collimated beam of light was passed through the test section perpendicular to the direction of argon flow. The intensity of the beam was measured with a photomultiplier and recorded by a strip chart recorder. Seed material was introduced into the test section by allowing some of the argon seed carrier gas to pass through the seed dispersal canister. The seeds were allowed to flow for periods of up to 10 min. The flow of seed material was stopped by adjusting the valves back to full bypass of the seed dispersal canister for the argon carrier flow. The intensity of the light transmitted through the test section before, during, and after seeds were flowing was recorded on the strip chart.

Propellant Heating Tests

For each series of tests the propellant heating configuration was assembled with a clean set of fused silica tubes. The simulated propellant heating portion of the operating procedure was as follows: the argon flow rates for the two buffer flows and the seed carrier flow were turned on and adjusted prior to discharge ignition (either the d-c or r-f discharge). The seed carrier flow was initially set for full argon carrier bypass of the high-pressure seed canister. The strip chart recorders for the radiometer and the propellant exhaust temperature measurements were turned on. The discharge was initiated. After the radiation and temperature measurements came to steady state, the seed flow was started using the following procedure. The agitator blades were started rotating, and argon was

then bled through the chamber to initiate the carbon seed flow to the test section. After a timed interval of operation (2.5-min maximum) the seed flow was turned off, and the radiation and exhaust temperature measurements were again allowed to come to steady state. This sequence was repeated several times. The average velocities of injection of the three parallel gas streams were matched at the entrance to the test section.

For each test, the argon weight flow rates were measured using rotameters. The average carbon weight flow rate was measured, for each series of tests, by measuring the change in weight of the carbon seed in the high-pressure canister and the total test time. Figure 31 is a photograph of the control system for propellant heating tests used at the 1.2-megw r-f induction heater facility with axial-coolant-tube models. This photograph also shows the high-pressure carbon feeder system, the radiometer, the still camera, the strip chart recorder, and a portion of the test-tank cover. Not shown are the control systems for the 1.2-megw r-f equipment and the data recording equipment.

The radiation transmitted through the test section to the radiometer located outside the propellant heating duct was measured before, during, and after seeded simulated propellant was introduced into the test section. The temperature of the propellant exhaust was measured by a chromel-alumel thermocouple located in the gas stream downstream of the test section. The thermocouple was positioned such that it was not exposed to radiation.

Discussion of Test Results

Tests With Cold-Flow Configurations

A schematic of the initial configuration used for simulated propellant flow experiments is shown in Fig. 32. A technique used for the deagglomeration of fluidized solid particles is to apply aerodynamic shear (Ref. 11). The hypo-tubes were intended to deagglomerate the particles just prior to their introduction into the propellant stream. Tests with this configuration were unsuccessful due to partial clogging of the hypo-tubes, resulting in uneven injection of seed material around the annulus. The nonsymmetric injection caused severe turbulence and coating of the walls. In some tests virtually all the tubes became clogged. The clogging was caused by large agglomerates in the plenum from which the tubes were fed. No conclusive results on buffer layer effectiveness were obtained with this configuration.

A two-dimensional configuration shown in Fig. 33 was designed to test the introduction of seeds through a slot. Argon gas seeded with carbon was used as the simulated propellant. In all tests, the average velocity of the seeded stream and the buffer gas were matched to reduce the shear and turbulence at the junction of the three parallel streams. To further reduce turbulence, the thin aluminum plates separating the seed duct from the buffer duct were tapered to a knife edge (half angle approximately 7 deg). Tests were conducted with velocities ranging from 5 to 25 ft per sec. The ratio of carbon to argon weight flow rate was varied from 0.1 to 2.0. The experimental results indicated that some coating of the lucite wall occurred. Heavier coating of the walls occurred for the lower velocities and the higher carbon-to-argon weight flow ratios. The degree of coating was measured by passing a collimated beam of light through the test section. The amount of light transmitted through the test section to a fiber optic tube was measured before, during, and after the seeded stream was flowing through the test section. The results indicated a rapid initial deposition of seeds onto the walls during the first tests of each test series. This initial deposit remained at a constant level for all the tests that followed in that series. The level of initial coating reached during each series represented an attenuation of from 40 to 60 percent of the light transmitted with clean lucite walls. In many of the tests the first 1.5 in. of the wall downstream of the inlet remained completely free of seed deposit. In the majority of the tests, some of the seed coating would be removed by turning off the seed flow and increasing the buffer flow. In a few tests, after this cleaning process, the light transmitted through the lucite walls returned to 98 percent of the original level. During the assembly and cleaning of the test equipment it was noted that small particles of dust and dirt adhered to the lucite walls. This may have been due to an electrostatic force between the particles and the lucite walls. An attempt was made to replace the lucite walls with fused silica plates. Sealing problems were encountered with this configuration. The level of wall coating that occurred in the two-dimensional tests with 0.117-in.-thick buffer layers was considered acceptable for the initial hot-flow tests. Therefore, no further tests were conducted on the question of the charge effect using fused silica plates.

Tests With Concentric-Coolant-Tube Model Configuration

The results of the propellant heating tests using the d-c arc heater and the 1.2-megw r-f induction heater with concentric-coolant-tube models will be discussed first. This discussion will be followed by a discussion of the results of the tests employing axial-coolant-tube models.

With few exceptions, partial wall coating with seeds occurred in all the tests. The wall coating was not uniform around the circumference of the propellant duct. As in the tests with the two-dimensional propellant flow simulator, the wall coating rapidly reached a certain level and remained constant for the remainder of the test series. The level of this initial coating resulted in a 40 to 70 percent attenuation of the light transmitted to the radiometer without seeds flowing. In all tests, argon with carbon seed was used as the simulated propellant. In the d-c arc heater tests, both the inner and outer buffer layers were 0.118-in. thick, and both the inner and outer fused silica walls of the simulated propellant heater duct became coated. However, for the 1.2-megw r-f induction heater tests with concentric-coolant-tube models, the outer wall with a 0.118-in.-thick buffer layer became coated, while the inner wall with a 0.253-in.-thick buffer layer remained clean during all the tests. It is therefore apparent that, with the configurations and test conditions used, the 0.253-in.-thick buffer layer was effective in preventing seed coating while the 0.118-in.-thick buffer layer was not. In many of the tests in which the coating occurred, the walls did not coat for the first 0.5 to 0.75 in. downstream of the inlet.

The migration of the seeds towards the walls in the configurations used is most likely governed by turbulent diffusion. No special steps were taken to reduce turbulence effects such as the addition of fine mesh screen or foam to the buffer inlets (Ref. 19). The steps taken were to match the average velocity of the buffer and seed flow streams and provide a length-to-diameter of greater than 20 for the entrance ducts connecting the plenums to the test sections. As in the two-dimensional tests, in many cases the walls could be cleaned to a condition of about 98 percent transmission by turning off the seed flow and increasing the buffer flows.

The fraction of radiation transmitted through the test section, η_T , is related to the attenuation parameter, $\rho_s \beta l$, by:

$$\eta_T = \exp[-\rho_s \beta l] \quad (3)$$

where ρ_s is the seed density, β is the experimentally determined mass attenuation coefficient, and l is the path length of the radiation. (See Appendix D for a discussion of Eq. (3)). The fraction of radiation absorbed in the seeded gas η_A , is:

$$\eta_A = 1 - \eta_T \quad (4)$$

In the propellant heating experiments, the percent absorbed ($\eta_A \times 100$) ranged from 12 percent to 33 percent. Values of β , the mass attenuation coefficient, were between $678 \text{ cm}^2/\text{gm}$ and $1990 \text{ cm}^2/\text{gm}$. The average value was $952 \text{ cm}^2/\text{gm}$.

Figure 40 shows typical data from the initial simulated propellant heating tests conducted in the 1.2-megw r-f induction heater. The data shown are time histories of the simulated propellant exit temperature (mixed-mean, or average) and the radiation transmitted through the test section from the r-f radiant energy source to the radiometer. Initially, with the r-f radiant energy source turned on before seed was introduced, argon gas was flowing through the test section, 1.25 kw of radiation was transmitted to the radiometer, and the simulated propellant exit temperature was 86.5 F. Note that this is a typical test where the initial wall coating had already occurred and the 1.25 kw is equal to the radiation transmitted through this coating to the radiometer. The 86.5 F temperature is the exit temperature of the argon with initial wall coating and without seeds. The seeds were introduced into the central portion of the simulated propellant duct at the time indicated by the first vertical dashed line in Fig. 40. The transmitted radiation decreased, and the propellant exhaust temperature simultaneously registered the corresponding rise. After about 2 min, the seed flow was turned off as indicated by the second vertical dashed line; the radiation transmitted returned to its initial level, as did the exhaust temperature.

The effect of the attenuation parameter, $\rho_s \beta \ell$, on the fraction of the radiation absorbed by the propellant stream, η_A , is shown in Fig. 41. The maximum value of η_A obtained in the tests was 0.33, compared to the value of 0.95 assumed for the nuclear light bulb. This reference nuclear light bulb value is based on absorption of normal radiation. The maximum value of the attenuation parameter was 0.41, compared to a value of 3.0 for the reference nuclear light bulb. The value of η_A can be increased by increasing the value of the attenuation parameter in the experiments. The effect of the propellant-stream seed density, ρ_s , on the fraction of the radiant energy absorbed within the propellant stream with the mass attenuation coefficient, β , as a parameter is shown in Fig. 42. The experimental value of the $\rho_s \ell$ obtained in tests was approximately equal to that required for the nuclear light bulb engine. However, the value of β obtained was lower than that required for the nuclear light bulb engine. Therefore, the main emphasis in future tests should be to obtain increases in the value of β from 1,000 to approximately 5,000. Values of β equal to or greater than 5,000 across a wide wavelength range have been obtained experimentally by the application of aerodynamic shear to a seeded stream (Refs. 11, 16, and 20). To achieve the full-scale absorption levels in the experiments with a small-scale duct, either β or ρ_s (or both) will have to slightly exceed the nuclear light bulb engine values to compensate for the smaller radiation path length.

Temperature rises in the propellant stream of between 13.9 R and 31.4 R with an average value of 24.9 R were obtained for the tests where a complete set of carbon flow rate, radiation transmission, and temperature-rise data were obtained (see Fig. 43). For several tests, temperature rises of up to 223 R were obtained. These tests were conducted with low velocities and heavy carbon flows. There was severe wall coating during these tests and the carbon flow rate was not steady. A complete set of data could not be taken. The argon flow rates during the tests with high values of temperature rise are shown with error bars in Fig. 43. All the measured temperature rise were greater than those which might be attributed to wall coating. For tests where complete data were obtained, the power absorbed in the propellant stream ranged from 0.06 kw to 0.14 kw with an average value of 0.10 kw. The average carbon weight flow rate was 0.0043 lb/sec for the d-c arc tests and 0.0046 lb/sec for the 1.2-megw r-f induction heater tests.

The temperature rise due to the absorption of thermal radiation achieved in these initial tests was limited to relatively low values for three principal reasons. First, coating of the walls accounted for up to about a 50 percent reduction in the radiant heat flux that passed through the inner wall of the propellant heating duct to the seeded stream. Elimination of the initial wall coating would allow a gain of about a factor of 1.66 in radiant heat flux incident on the simulated propellant stream. Second, a low value of β occurred in the experiments due to insufficient deagglomeration. Improvement of the absorption properties to levels approaching those required for the reference engine would represent at most a factor-of-three increase in absorption (i.e., 33 percent is already being absorbed). Combining these two effects, a factor-of-five increase in radiant-energy absorption (and corresponding temperature rise) would be expected within the seeded gas stream. The final, and most important reason, is that the tests were conducted at low radiant energy source power levels. The d-c arc source has radiated about 130 kw from a 10-in.-long arc and the 1.2-megw r-f induction heater radiant energy source has radiated 156 kw (Section III) from a 2.0-in.-long discharge. The radiant power levels used in the tests were between 1 and 3 kw radiated. Therefore, increases on the order of a factor of 50 in radiant power are available from the already existing energy sources. The low-power levels employed were due to the problems encountered in making the simulated-propellant heating duct compatible with operation in the vicinity of the intense radiant energy sources. In the case of the d-c arc radiant energy source, additional shielding of seals and shielding of the propellant duct inlets from the intense radiation flux are required. These modifications are within the state-of-the-art of high-heat-transfer cooling technology. With the 1.2-megw r-f induction heater facility configuration using these concentric-coolant-tube models, improved vortex injection techniques now understood as a result of the concurrent research with the radiant energy source, as discussed in Section III, are needed. As potentially higher radiant heat flux levels are used in future

simulated propellant heating tests, increased cooling of the simulated propellant heater components surrounding the radiant energy source and more advanced transparent wall configurations than the concentric-coolant-tube models used for these tests are required.

Tests With Axial-Coolant-Tube Model Configuration

In the propellant heating tests with axial-coolant-tube models, no conclusive measurements of simulated-propellant temperature rise due to radiation absorption could be made. The reason was that the axial coolant tubes were heavily coated with carbon seed in all the tests; hence, no significant deposition of energy occurred in the simulated propellant stream. The coating thickness was such that almost 98 percent of the radiation was blocked from the propellant stream. The small spaces (see Fig. 22b) between the axial coolant tubes permitted some of the argon gas injected inside the model to interact with the simulated propellant stream. This apparently caused turbulence and mixing in the propellant stream and resulted in wall coating. Various velocities and seed flow rates were employed. However, it is felt that the interaction of the simulated propellant with the vortex flow was the dominant effect on wall coating. Future axial-coolant-tube models must be modified to reduce the interaction. Coating of the axial coolant tubes with carbon seeds made it difficult to separate the radiant heat load to the model from the plasma side from that of radiation absorption due to seed coating on the simulated-propellant side of the axial coolant tubes. Refer to Section IV for details of the model test results for these experiments.

Further simulated propellant heating tests should employ aerodynamic shear to deagglomerate the seeded flow prior to entering the inlet section of the simulated propellant heater test section. Tungsten should also be used as a seed since it appears more promising than carbon as a seed material for the full-scale engine (Ref. 19). Cold-flow tests should be continued to optimize the inlet design and hence minimize the turbulence level in the simulated propellant flow. These tests should be designed to provide thin buffer layers without wall coating as an ultimate goal. Concurrent hot-flow tests should be conducted with relatively thick buffer layers to obtain a large temperature rise in the propellant stream. Additional propellant heating configurations compatible with the existing high-power radiant energy sources must be designed and fabricated. The results of these efforts should then be combined to design, fabricate, and test configurations that will result in high temperatures with the thinnest possible buffer layers. It is important to test these configurations in a high-temperature environment because effects such as photophoresis and thermal diffusion might alter the performance of a configuration that was successful in cold-flow tests. Simulation of propellant

heating, at full-scale engine heat flux levels, will require an axial or circumferential-coolant-tube model between the plasma and the propellant flow. Therefore, models must be developed which do not allow the interaction of the vortex with the propellant flow. In addition, more adequate techniques for measuring the seed flow rate and measuring the high temperatures of the seeded simulated propellant in the vicinity of an intense radiation field must be developed.

REFERENCES

1. McLafferty, G. H. and H. E. Bauer: Studies of Specific Nuclear Light Bulb and Open-Cycle Vortex-Stabilized Gaseous Nuclear Rocket Engines. United Aircraft Research Laboratories Report F-910093-37, prepared under Contract NASw-847, September 1967. Also issued as NASA CR-1030, 1968.
2. Clark, J. W., B. V. Johnson, J. S. Kendall, A. E. Mensing, and A. Travers: Summary of Gaseous Nuclear Rocket Fluid Mechanics Research Conducted Under Contract NASw-847. United Aircraft Research Laboratories Report F-910091-13, May 1967.
3. Kendall, J. S., W. C. Roman, and P. G. Vogt: Initial Radio-Frequency Gas Heating Experiments to Simulate the Thermal Environment in a Nuclear Light Bulb Reactor. United Aircraft Research Laboratories Report G-910091-17, prepared under Contract NASw-847; September 1968. Also issued as NASA CR-1311.
4. Mensing, A. E., and J. F. Jaminet: Experimental Investigation of Heavy-Gas Containment in R-F Heated and Unheated Two-Component Vortexes. United Aircraft Research Laboratories Report H-910091-20, prepared under Contract NASw-847, September 1969.
5. International Critical Tables, Vol. V. McGraw-Hill Book Company, Inc., 1930.
6. Mensing, A. E., J. S. Kendall: Experimental Investigation of Containment of a Heavy Gas in a Jet-Driven Light-Gas Vortex. United Aircraft Research Laboratories Report D-910091-4, prepared under Contract NASw-847, March 1965.
7. Mensing, A. E. and L. R. Boedeker: Theoretical Investigation of R-F Induction Heated Plasmas. United Aircraft Research Laboratories Report G-910091-18, prepared under Contract NASw-847, September 1968. Also issued as NASA CR-1312.
8. Thorpe, M. L.: Radio-Frequency Plasma Simulation of Gas-Core Reactor. Journal of Spacecraft and Rockets, Vol. 6, No. 8, August 1969.
9. Marteney, P. J., A. E. Mensing, and N. L. Krascella: Experimental Investigation of the Spectral Emission Characteristics of Argon-Tungsten and Argon-Uranium Induction Heated Plasmas. United Aircraft Research Laboratories Report G910092-11, prepared under Contract NASw-847, September 1968. Also issued as NASA CR-1314.
10. Krascella, N. L.: Theoretical Investigation of the Absorption and Scattering Characteristics of Small Particles. United Aircraft Research Laboratories Report C-910092-1, prepared under Contract NASw-847, September 1964. Also issued as NASA CR-210.

11. Marteney, P. J.: Experimental Investigation of the Opacity of Small Particles. United Aircraft Research Laboratories Report C-911092-2, prepared under Contract NASw-847, September 1964. Also issued as NASA CR-211.
12. Marteney, P. J., N. L. Krascella, and W. G. Burwell: Experimental Refractive Indices and Theoretical Small-Particle Spectral Properties of Selected Metals. United Aircraft Research Laboratories Report D-910092-6, prepared under Contract NASw-847, September 1965.
13. Krascella, N. L.: Theoretical Investigation of the Absorptive Properties of Small Particles and Heavy-Atom Gases. United Aircraft Research Laboratories Report E-910092-7, prepared under Contract NASw-847, September 1965.
14. Krascella, N. L.: Tables of the Composition, Opacity, and Thermodynamic Properties of Hydrogen at High Temperatures. United Aircraft Research Laboratories Report B-910168-1, prepared under Contract NAS 3-3382, September 1963. Also issued as NASA SP-3005.
15. Lanzo, C. D., and R. G. Ragsdale: Experimental Determination of Spectral and Total Transmissivities of Clouds of Small Particles. NASA Technical Note D-1405, September 1962.
16. Lanzo, C. D., and R. G. Ragsdale: Heat Transfer to a Seeded Flowing Gas from an Arc Enclosed by a Quartz Tube. NASA Technical Memorandum X-52005, June 1964.
17. Marteney, P. J., and N. L. Krascella: Theoretical and Experimental Investigations of Spectral Opacities of Mixtures of Hydrogen and Diatomic Gases. Air Force Systems Command Report RTD-TDR-63-1102, prepared by United Aircraft Research Laboratories under Contract AF 04(611)-8189, November 1963.
18. Mie, G.: Annalen der Physik, Vol. 30, 1919.
19. Johnson, B. V.: Exploratory Experimental Study of the Effects of Inlet Flow Conditions on the Flow and Containment Characteristics of Coaxial Flows. United Aircraft Research Laboratories Report H -910091-21, prepared under Contract NASw-847, September 1969.
20. Williams, J. R., J. D. Clement, A. S. Shenoy, and W. L. Partain: The Attenuation of Radiant Energy in Hot Seeded Hydrogen - An Experimental Study Related to the

Gaseous Core Nuclear Rocket. Quarterly Status Report No. 2, NASA Research Grant NGR-11002-068, prepared by Georgia Institute of Technology, February 1969.

21. Aden, A. L.: Electromagnetic Scattering from Spheres with Sizes Comparable to the Wavelength. Journal of Applied Physics, Vol. 22, No. 5, May 1955.
22. Van der Hulst, H. C.: Light Scattering by Small Particles, Wiley, New York, 1957.
23. Latham, T. S., H. E. Bauer, and R. J. Rodgers: Studies of Nuclear Light Bulb Start-up Conditions and Engine Dynamics. United Aircraft Research Laboratories Report H-910037-4, prepared under Contract NASw-847, September 1969.
24. McLafferty, G. H.: Studies of Coolant Requirements for the Transparent Walls of Nuclear Light Bulb Engine. United Aircraft Research Laboratories Report F-110224-6, March 1967.
25. General Electric Company: Fused Quartz Catalog, Form Q13, May 1967.

LIST OF SYMBOLS

A_M	Transparent-wall model tube surface area, sq ft or sq in.
A_S	Discharge surface area, sq in.
$b_{a,\lambda}$	Monochromatic mass absorption coefficient, cm^2/gm
$b_{e,\lambda}$	Monochromatic mass extinction coefficient, cm^2/gm
$b_{s,\lambda}$	Monochromatic mass scattering coefficient, cm^2/gm
\bar{b}_e	Total mass absorption coefficient, cm^2/gm
D	Diameter of unit cavity, transparent-wall model or fused silica tube, in. or ft
d	Discharge diameter, in.
$F_{C,C}$	Fraction of power removed by conduction-convection losses, $1 - \left[\frac{Q_{R,T}}{Q_T} \right]$
f	Frequency, MHz
I	Total intensity of light $\text{kw}/\text{cm}^2\text{-ster}$
I_A	Arc current, amperes
I_λ	Monochromatic intensity, $\text{kw}/\text{cm}^2\text{-ster}$
$I_{o,\lambda}$	Incident monochromatic intensity, $\text{kw}/\text{cm}^2\text{-ster}$
$I_\lambda/I_{o,\lambda}$	Internal transmittance, dimensionless
\bar{K}_a	Total absorption coefficient, cm^{-1}
$K_{a,\lambda}$	Monochromatic absorption coefficient, cm^{-1}
$K_{e,\lambda}$	Monochromatic extinction coefficient, cm^{-1}
$K_{s,\lambda}$	Monochromatic scattering coefficient, cm^{-1}
$\bar{K}_{a,\lambda}$	Total monochromatic absorption coefficient, cm^{-1}
$\bar{K}_{s,\lambda}$	Total monochromatic scattering coefficient, cm^{-1}

\bar{K}_a	Total absorption coefficient, cm^{-1}
\bar{K}_s	Total scattering coefficient, cm^{-1}
L	Length of unit cavity or transparent wall model, in. or ft
ℓ	Path length of radiation, cm
N	Particle number density, particles/ cm^3
P	Total pressure, atm or psia
P_D	Chamber pressure, atm
Q_C	Power conducted through inner peripheral wall, kw
Q_E	Power deposited in end-wall cooling water, kw
Q_I	Total d-c input power to r-f induction heater, kw
Q_L	Power convected through thru-flow exhaust ports, kw
Q_P	Radiant power deposited in the propellant stream, kw
Q_R	Radiated power as measured by radiometer, kw
Q_T	Total discharge power ($Q_R + Q_W + Q_E + Q_L$), kw
Q_W	Power deposited in peripheral wall coolant, kw
$Q_{A,0}$	Power deposited in argon by-pass of axial-coolant-tube model, kw
$Q_{C,0}$	Power deposited in cooling water of axial-coolant-tube model, kw
$Q_{R,T}$	Total radiated power, $Q_R + Q_W - Q_C$, kw
$Q_{R,3}$	Power radiated from a 3-inch length of d-c arc, kw
$Q_{T,3}$	Total power deposited in a 3-inch length of d-c arc, kw
R_B	Ballast resistance, ohms

$Re_{t,j}$	Injection Reynolds number based on average inlet jet velocity, dimensionless
r	Local radius from center of chamber, discharge radius, or particle radius, in., ft, or cm
T	Temperature, deg R or deg K
T_{AV}	Intensity-averaged temperature in plasma, deg R or deg K
T_e	Simulated propellant exit temperature, deg F
T^*	Equivalent black body radiating temperature, deg R
t	Time, min
V	Discharge volume, in. ³
x	Transparent wall thickness, in.
v	Local velocity, ft/sec
V_A	Arc voltage, volts
v_l	Tangential velocity at periphery, ft/sec
v_j	Average buffer gas injection velocity, ft/sec
W_A	Argon weight flow rate or buffer weight flow rate, lb/sec
W_C	Coolant weight flow rate, lb/sec or gpm
ΔT_e	Temperature rise of simulated propellant, deg R
β	Experimentally determined mass attenuation coefficient, cm ² /gm
η	R-F system coupling efficiency, Q_T/Q_I , dimensionless
η_A	Fraction of incident radiation absorbed by propellant stream, $1 - \exp(-\rho_s \beta l)$ dimensionless
η_T	Fraction of incident radiation transmitted through the propellant stream, $\exp(-\rho_s \beta l)$.

ϕ_R	Radiant energy flux from surface of the plasma, $Q_{R,T}/A_S$ kw/in. ²
ρ_s	Seed density, gm/cm ³
σ_H	Indicated hoop stress, psia
$\sigma_{a,\lambda}$	Monochromatic absorption cross section, cm ² /particle
$\sigma_{e,\lambda}$	Monochromatic extinction cross section, cm ² /particle
$\sigma_{s,\lambda}$	Monochromatic scattering cross section, cm ² /particle
τ	Optical thickness, dimensionless
λ	Wavelength, microns or Angstroms
$\rho_s \ell$	Seed density parameter, gm/cm ²
$\rho_s \beta \ell$	Attenuation parameter, dimensionless

APPENDIX A

PRELIMINARY DESIGNS FOR 200- AND 500-ATM R-F PLASMA TEST EQUIPMENT

Introduction

To permit simultaneous simulation of full-scale nuclear light bulb engine operating pressures and radiant heat fluxes, r-f plasma test equipment capable of 200- and 500-atm operation has been designed (the total pressure for the reference full-scale engine is about 500 atm).

Background

High-pressure (200 or 500 atm) plasma radiant energy source test equipment for r-f plasma discharges presents many design, installation, and operational problems not normally encountered in high-pressure work. Consequently, a rather complex and expensive high-pressure system would have to be fabricated and tested for safe operation up to these high pressures. Such a facility is within the state-of-the-art as far as high pressure is concerned. However, incorporating a highly radiating source within the system will require that each unit in the system be highly engineered, fabricated of special materials, integrated into the system with special pressure balancing between cooling liquid and test gas, and critically tested for reliability and personnel safety. By incorporating a pressure-balancing and submersible-pump concept into the high-pressure system discussed in the following paragraphs (see also Fig. 44), together with a fiberglass pressure vessel, an inexpensive, safe, and relatively simple experimental high-pressure test system can be constructed. The end result would be an experimental capacity for testing r-f plasma or components at high pressures, in any gaseous environment, with or without external stabilizing electric or magnetic fields.

Statement of the Problem

The objective is to provide safe, reliable high-pressure r-f plasma test equipment capable of continuous operation at 200 (and/or 500) atm. The equipment should permit testing of the transparent-wall models and propellant-heating configurations and be compatible with the existing 1.2-megw r-f induction heater facility.

The hazards involved in any 200 atm (or 500 atm) installation must be thoroughly understood. Some of the special hazards associated with this system, which must be fully considered, are as follows:

1. Special hazards associated with r-f plasma testing (i.e., high-power r-f plasma in a chamber).
2. Method of r-f plasma operation; special operating procedures.
3. High radiant energy flux shielding.
4. Sudden release of stored energy.
5. Necessity for remote monitoring and control (no direct viewing of the test section is permissible).

Major Component Requirements

The major requirements of the pressure vessel are the following: capable of withstanding continuous high-pressure loading as well as cyclic application and removal of the test pressure; fabricated of materials not strongly affected by r-f fields; capable of being opened and closed repeatedly; structurally sound and not susceptible to deformation on repeated use at the high test pressures; capable of existing in the radiant energy flux level environment established after radiation attenuation by the peripheral-wall water-dye coolant; capable of being installed within the existing 1.2-megw r-f work coils or coils of a slightly larger diameter; provision for the introduction and removal of cooling water and test gases (both these connections should be made at the extreme ends of the vessel, near the end-wall test-chamber interface). In addition, it should be possible to assemble the end walls to be tested onto the pressure vessel end plates, and to insert the whole assembly into the test chamber. It is expected that disassembly and reassembly of the test set-up will be done numerous times. Insulated instrumentation leads must be fed into the test chamber. The type of conductor and seal method should be such that "pinch-off" does not occur. Provisions should be made for the inclusion of direct viewing diagnostic probes to permit measurements of the radiation, particularly in the ultra-violet region of the spectrum.

The major requirements of the cooling water system are the following: designed for removing approximately 216 kw of power, which is the present operating level of the 1.2-megw r-f system (provisions can be included to extend this to 600 kw, an early design point of the 1.2-megw r-f system); capable of circulating the cooling water in the most efficient and economical way; provision for a pressure-

balancing and replenishing water supply; designed such that air is not trapped in the system; water pump must produce sufficient pressure to overcome the pressure drop in the piping, discharge chamber passages, heat exchanger, and associated fittings; pressure pulsations from the pump must be at a minimum so they do not cause weakening of low-pressure connections within the equipment (particularly on the transparent wall models); the water pressure and gas pressure should be balanced to approximately ± 1.0 percent during the charging, steady-state operation, and discharge operation.

The major requirements of the gas system are the following: since gas cylinders as received are normally at pressures of approximately 150 atm or less, means should be provided to bring this gas up in pressure to approximately 200 atm (or 500 atm in the case of the 500-atm design) and stored until needed to charge the system; all gas compression should be done so that no hydrocarbon or other impurities are introduced.

For safety reasons, the operating personnel should be located in a position remote from the high-pressure device when the equipment is operating under pressure. This necessitates monitoring all items such as pressures, temperatures, flow rates, etc., to indicate both normal and faulty operation. In addition to remote observations, the operator should be able to remotely charge, operate, and discharge the system.

Discussion

Figure 44 is a block diagram illustrating the basic design of the high-pressure system. It was designed to overcome the several problem areas discussed previously. For simplicity, the separate gas and water systems required for the different test configurations are not shown. Special consideration has been given to desirable operational features such as remote control, system operational checks, and safe isolation of water and gas. In addition to convenient operation, this system would provide maximum safety by having a minimum of piping, valves, and fittings required for a good installation.

A closed-loop configuration is used which includes the gas charging system, heat exchanger, pressure accumulator, test pressure vessel, and a submersible centrifugal water pump installed within a second high-pressure vessel. The submersible pump and pressure accumulator concept allow an accurate continuous balance of gas and water pressure throughout the entire operating pressure range of 1 to

200 atm (or 500 atm). Following is a general description of the overall system operation, and of each major component which makes up the system.

Gas Charging System

A gas compressor takes the gas from the argon bottle supply and compresses it to approximately 200 atm for storage in the gas charging and storage tanks. The inlet pressure to the gas compressor may be from 33 atm to 135 atm. Appropriate valves and fittings are provided to make use of the low-pressure gas. A valve is provided which isolates the argon supply from the system when it is not in operation. Similarly, an isolation valve is provided after the compressor so that the storage tanks can be left charged without back pressure on the compressor. This valve is located close to the storage tanks to minimize the quantity of piping which will stand exposed to high pressure during inactive periods.

The lines between the main gas line and the storage tanks are sized and adjusted in length to provide restricted release of energy. With a series of lines in parallel, no limitation is placed on the charging system; however, it will provide some limit to the rate of energy release of the high-pressure gas storage system should there be an inadvertent release.

A power-operated valve is located near the storage tanks and will provide remote control for charging the test chamber system with gas. Pressure regulators located on the master control console and downstream of the power-operated valve will allow for a pressure differential between the water and test gas. After charging, the power-operated valve will be remotely closed so the system can be reduced in pressure without reducing the pressure in the storage tanks.

In charging the system with gas, the pressure will go to both the test pressure chamber and to the cooling water system. In addition, the pressure accumulator will be charged. Pressures from the various chambers will be displayed to the operator.

Gas Compressor

The gas compressor is a diaphragm-type designed for a discharge pressure of 200 atm (or 500 atm) at inlet pressures greater than or equal to 33 atm. The pumping rate is not critical. The diaphragm-type of pump is used so that no hydrocarbon or other impurities are introduced into the test gas.

Cooling Water System

Gas for pressurizing the cooling water system will be supplied to the pressure accumulator through a check valve. This valve will assure that water or water vapor will not feed back into the gas in the test chamber and create a plasma hazard and/or contaminate the experiment being conducted.

Fill ports are provided for water filling the entire system and the pressure accumulator. When filling the pressure accumulator, a drain valve is used as a vent. Circulation of the water by the pump at atmospheric pressure will eliminate any air in the water piping, heat exchanger, and test chamber passages. The velocities are such that trapped air will be circulated with the water. This air can then be exchanged for water at the pressure accumulator; the accumulator will then be refilled and the system closed for operation. The accumulator is of sufficient size to provide for any gas or air still trapped in the system.

Submersible Motor and Water Pump

Typical high-pressure pumps are very expensive and consume large amounts of power; e.g., a factor of ten is normal for the power difference required between conventional and submersible pump motors. Consequently, a concept employing a submersible pump will be used. The submersible water pump and motor is a commercially available unit. The 230-v, 2-hp motor is oil filled and permanently sealed with a two-piece stator construction. The pump is a typical deep-well type employing a compact coaxial diffuser system and hydraulically balanced impellers. All high-pressure values, fittings, and tubing are standard. Values are provided in the system to permit isolation of the major components.

The cooling water would be circulated by the submersible centrifugal-type pump and motor illustrated in Fig. 44. This pump will produce a differential pressure of at least 10 atm. It is estimated that there will be a 1-atm pressure drop in the heat exchanger, and the remaining pressure will be lost in the piping and test chamber.

The cooling water pumping system is arranged and pressurized so that, during operation, the water pressure in the test facility will normally be a few percent higher than the gas pressure (depending on operating pressure level).

Heat Exchanger

The heat exchanger is a "U" tube-in-tube heat exchanger employing a Brown pin-tube type geometry. The heat exchanger is designed in accordance with the ASME pressure vessel code. The water leaving the test chamber will be monitored for temperature and passed through the heat exchanger. Measurement of temperature is considered a very necessary safety feature; should this temperature increase above 630 R it will indicate an abnormal condition. Further increases would greatly reduce the design safety factors; therefore, close observation of temperature is desirable.

No particular requirements, other than a flow of about 35 gpm and a supply temperature of 510 to 530 R, are applicable to the water required to cool the heat exchanger.

Test Chamber

The reference test chamber will be a 2.2 in.-ID vessel with an inside length of 40 in. The vessel is designed for a working pressure of 200 atm (the 500-atm configuration would have an increased wall thickness) at 660 R and would be hydrostatically tested to 400 atm at 532 R. The vessel parts would be ultrasonically tested for cracks before fabrication.

The structural parts of the vessel (end caps and end pieces) will use type 316 stainless steel. The test chamber will be a fiber glass tube with stainless steel end pieces locked in by the glass filament windings. The auxiliary glands and fittings of the vessel will be constructed of 200-series stainless steel.

The stress calculations for the various pressure vessels were computed using the design factors of Ref. 1. The selection of the glass filament-wound vessel results in approximately a factor-of-two decrease in wall thickness over that required by stainless steel. However, a stainless steel or aluminum test chamber would shield the test section from the r-f fields. The end caps are constructed in such a manner that the test apparatus can be assembled to the end caps outside the chamber, thus allowing the end-cap test apparatus assembly to be inserted into the chamber as a unit. Each end cap contains six passages for cooling water, four electrical feed-throughs, and one passage for pressurizing and exhausting the chamber. The material of constructions of the end cap is type 316 stainless steel.

The end cap retainers are cylindrical in shape with a modified Acme thread (2 threads/in.). The Acme thread was selected over a Buttress thread because of minimum stress concentration and minimum galling advantages.

Thermocouples are located at various positions in the vessel wall to permit monitoring of the local temperature in critical areas.

Pressure Accumulator

The pressure accumulator vessel is designed for a working pressure of 200 atm (500 atm in the case of the 500 atm system) at 440 to 660 R and a hydrostatic test pressure of 270 atm at 532 R. The vessel is designed in accordance with the ASME pressure vessel code. The volume of the vessel is 5 gallons.

Means have been provided to absorb minor surges which may be encountered. If the surge reaches such magnitude that it is overpressurizing the test chamber, relief valves are provided to quickly release the overpressure in the vessel.

Control Console

The console for controlling the high-pressure system will provide the operator with both operating information and control capability. The console will be located away from the immediate area of the high-pressure test vessel. Through proper instrumentation, the operator will have immediate knowledge of the following items: (1) gas pressure in the test chamber; (2) differential pressure between the cooling water loop and the test chamber, (3) cooling-loop water flow rate, and (4) maximum temperature of water in the cooling-loop. Remote control of the following items will be provided at the console: (1) pressurization of the test chamber and water cooling-loop; (2) depressurization of the test chamber and cooling-loop, (3) cooling water pump operation, and (4) gas compressor operation.

Safety Considerations

The safety of this high-pressure system has been the foremost consideration throughout the preliminary design phase. Some of the basic considerations include: (1) design of the test chamber, heat exchanger, pressure accumulator, gas storage tanks, and control console by personnel extensively experienced in high-pressure technology; (2) all high pressure values, pipings, fittings, and other equipment would be selected on an "off-the-shelf" basis where possible; (3) boiler code safety factors have been used as the minimum criteria; and (4) fast-acting surge protection for the system will be used.

APPENDIX B

DIMENSIONAL CHARACTERISTICS AND HYDROSTATIC TESTS OF FUSED SILICA TUBES

Dimensional Characteristics

The fused silica coolant tubes used in the transparent-wall models should have uniform wall thickness to provide a nearly uniform temperature distribution across the wall. Local variations in tube wall thickness could result in "hot spots" where the wall is thick or structurally weak areas where the wall is thin. In the transparent-wall models it is desirable to have the tubes as close as physically possible along their entire length so as to reduce the flow leakage across the model.

Measurements were made to determine the variation in wall thickness for samples of the fused silica tubes used in this investigation. The sample tubes were cut into 2-in. lengths and the inner and outer diameters were measured at each end of the tube. The inner diameter was measured by inserting a drill rod into the tube and the outer diameter was measured with a micrometer. A summary of the average wall thickness as determined from these measurements is given in Table V. A variation of 20 percent in wall thickness was typical for standard-grade fused silica tube samples. When these tubes were drawn to produce thinner walls (i.e., 0.010- and 0.005-in.-wall thickness) the variation increased significantly. The variation in wall thickness was greatest for the 0.005-in.-wall thickness tubes which were fabricated from larger diameter tubing.

Hydrostatic Tests

Hydrostatic tests were conducted with samples of the fused silica tubes used in the high-pressure gas discharge tests. Figure 45 is a sketch of the two aluminum end-wall caps which were fabricated to simulate the actual seal arrangement used in the 1.2-megw r-f heater. A separate pair of end-wall caps was fabricated for each of the different size fused silica tubes. A hydraulic accumulator was used to pressurize the tubes to failure and the pressure in the tube at the point of failure was recorded. Results of these tests are shown in Fig. 46. Hoop stresses at failure in the range of 4000 to 7000 psi were obtained. The mode of failure was such that the tubes developed many longitudinal cracks prior to breaking into individual pieces which resembled glass slivers.

APPENDIX C

DESCRIPTION OF D-C ARC HEATER

The d-c arc heater was constructed in 1968 as part of a UARL Corporate-sponsored program. This facility was designed for supporting the transparent-wall model tests, plasma seeding tests, and simulated propellant heating tests. Although the d-c arc heater, subject to certain modifications, has the capability to be run at high power and high pressure levels (considerably higher than the 1-atm design), it cannot simulate the high energy density or power per unit length possible with the 1.2-megw r-f induction heater.

Figure 34 is a schematic diagram showing the primary components of the d-c arc heater facility. The arc power is supplied by two, 250 kw rated shunt-wound General Electric motor-generator sets. The motor generators may be connected for either series or parallel operation. Power control is provided by setting a remote-controlled rheostat which permits the motor generator field voltage to be pre-set prior to and during each test. All control units, including a remote start-stop control, are located on the arc control console.

Figure 35 shows the operating range of the d-c power supplies together with results of tests employing an argon arc operating at approximately 1.0 atm pressure. For these tests the motor generators were connected in series. For those tests in which the arc current was greater than 1200 amp, the motor generators were operated for a short time in a series overload condition. Experiments using d-c arcs (with their inherent nonlinear dependence between voltage and current) are restricted by circuit considerations as to what operating range and stability can be attained. The arc can also exhibit large variations in static voltage-current characteristics depending on environmental conditions. The arc circuit is stable provided $R_B + dV_A/dI_A > 0$, where R_B is the ballast resistance, V_A is arc voltage, and I_A is arc current. Thus a 0.1-ohm air-cooled ballast resistor was added to the d-c power supply circuit to provide stable arc operation. A distinct advantage of d-c arc operation from motor generator power is the elimination of the undesirable power ripple inherent in all moving coil transformer or saturable-reactor-type power supplies.

The sketch of the basic d-c arc heater configuration used in the initial propellant heating tests is shown in Fig. 36. This configuration consists of a vortex-stabilized d-c arc enclosed within concentric water-cooled fused silica tubes. The dimensions of the inner fused silica tube were 1.26-in. ID by 1.37-in. OD, and those of the outer fused silica tube were 1.69-in. ID by 1.57-in. OD. The arc is established between a pin cathode and a hollow cylindrical anode. The cathode is a hemispherical-tipped 2 percent thoriated-tungsten rod of 0.25-in. diameter. The cathode is recessed and silver-soldered into a water-cooled copper well. The cathode is capable of being varied in a vertical displacement to optimize the location, size, operating temperature, and constriction of the cathode attachment spot. Experiments have indicated that the cathode operating temperature plays a role in achieving stable, uncontaminated, long-lifetime operation, particularly at high power levels. The cylindrical copper anode is also water-cooled and contains a 0.5-in. hole on its centerline with rounded corners. The anode is surrounded by a water-cooled magnetic field coil. The magnetic field coil is connected in series with the arc circuit. The interaction between the magnetic field from the coil and the arc current in the anode spot attachment region causes the arc anode attachment spot(s) to rotate rapidly. By magnetically driving the anode spot(s) at high speeds (approaching 2000 rev/sec) over the anode surface, the very high heat load in the anode spot region is spread over a significantly larger area. This permits the water cooling flowing meridianally within the anode cooling passage to remove the heat more effectively, thus preventing local melting and subsequent anode failure. This magnetically augmented water-cooled anode is capable of satisfactory operation at current levels of approximately 1500 amperes. The average lifetime of this type of anode is several hours. The length of quartz tubes used to surround the arc discharge are limited only by available power-supply voltage (see Fig. 35); thus, a discharge of several feet in length could be operated if desired in future simulated-propellant heating geometries.

The arc column is stabilized by the vortex flow which is introduced into the plenum surrounding the cathode assembly. The vortex generator injection assembly has four equally spaced vertical stainless steel tubes through which the argon gas flows. Each of these tubes has four 0.015-in.-dia holes, spaced 0.118 in. apart, drilled in it. The argon vortex flow provides a non-oxidizing environment which minimizes erosion of the tungsten cathode. The angle of vortex injection can be varied from full radial (coaxial flow) to full tangential (vortex flow) during arc operation by a variable-speed servo-motor drive and gear assembly. This permits establishing the optimum vortex geometry for a particular power level and vortex tube length-to-diameter ratio. The optimum condition is when the discharge axis is non-oscillatory and colinear with the axis of the fused silica tube surrounding the discharge. The vortex generator is connected to the inner fused silica tube through a convergent nozzle. Argon weight flow rates up to 0.024 lbs per second were used in the vortex generator.

The transition of the arc from the column to the anode occurs at the water-cooled copper locator. The locator serves to help confine the arc to the centerline of the fused silica tube. It also acts as the interface between the plasma and the top of the test facility. The convergent-divergent shape of the locator helps minimize anode erosion by directing the arc column into the center of the anode. The inner diameter of the locator was chosen as 3/8 in. to minimize pinching effects on the arc column.

The cathode and anode were electrically isolated from the components of the propellant heating test equipment and from the table which supported the configuration. The entire arc configuration is mounted on an adjustable table. This allows changes to be made in arc length without changing the position of the test section relative to various diagnostic systems (see SECTION II). All exhaust gases from the arc test section were removed through a vacuum ventilation system (1500 cfm capacity) which was installed directly above the arc test section.

Cooling water for the arc heater is supplied from a 4-in. main at approximately 80 psig (Refer to Fig. 34). Centrifugal-type water pumps, rated at 185 psig at 150 gpm, were connected to the water inlet. A high-pressure water manifold and high-pressure hose were used to supply cooling water to each element of the arc heater. The low-pressure return lines fed into rotameters to permit determination of the coolant flow rate through each element. A high-pressure argon bottle farm and manifold system provided the necessary argon gas flow for the vortex generator and the other auxiliary test equipment requiring argon gas. The arc operation was controlled from a central console housing both the electrical and fluid mechanical controls (Refer to Fig. 34).

The arc was initiated by employing a secondary tungsten-tipped stainless steel anode which initially makes contact with the cathode, and was then rapidly withdrawn (approximately 10 fps) upward through the primary anode. In this way, the arc was drawn vertically upward until it reached the level of the primary anode. Transfer from the secondary anode to the primary anode was accomplished as the secondary anode continued upward to its full retracted position. The starting system is actuated by a 2-way pneumatic cylinder. The starting sequence was synchronized such that the withdrawal of the secondary anode lagged the main arc power initiation by approximately 0.5 sec. This fully established the arc current prior to drawing apart the electrodes. During the starting sequence, an air-cooled ballast resistor was used to limit the arc current to 50 amp. This current-limiting technique was used to reduce contamination of the test-section walls due to tungsten sputtering caused by a sudden high current arc or the contamination which would be given off had an exploding wire starting technique been employed.

The arc has been operated at radiation levels up to 45.0 kilowatts in the 3.0-in.-long test section. Figure 37 is a plot of the power radiated through the 3-in. test section as a function of the total power deposited into the arc in the 3-in. test section length. The fraction of total power radiated per unit length increases from the low powers to the higher powers. Up to 73 percent of the total power per unit arc length has been radiated. To aid in comparison, a straight line with a slope of 0.7 is shown in the figure for the higher power levels. A corresponding change in argon weight flow rate and vortex injector angle also affects the specific radiation. The radiation measurements were made using the radiometer system described in the equipment section and shown in Fig. 6. A double-slit aperture arrangement was located between the collimating tube of the radiometer and d-c arc source to permit measurements within the 3-in.-test section only. During the tests of the operational capability of the d-c arc heater, the propellant heating ducting and associated water cooling were removed. At the higher power levels test times were limited to several seconds due to severe heating of the uncooled quartz tube. However, run times of several seconds are at least two orders of magnitude greater than the residence time of a fluid element of the simulated propellant within the test section.

APPENDIX D

OPTICAL PROPERTIES OF PARTICLE CLOUDS

In traversing an absorbing-scattering medium, such as a cloud of particles, a beam of radiant energy is attenuated. Part of the total attenuation is due to absorption and the remainder is due to the removal of energy from the incident beam by scattering. Absorption is the removal of energy from the beam by dissipative processes within the medium. Scattering in this discussion includes the combined processes of reflection, refraction, and diffraction.

The fractional decrease in the intensity of a monochromatic beam, I_λ , is proportional to the distance traveled by the beam, dl , or

$$\frac{dI_\lambda}{I_\lambda} = -K_\lambda dl \quad (D-1)$$

In the absence of scattering, the constant K_λ is defined as the absorption coefficient, $K_{a,\lambda}$; in the absence of absorption it is defined as the scattering coefficient, $K_{s,\lambda}$. If both absorption and scattering take place in the medium, then the K_λ is defined as the total attenuation or extinction coefficient, $K_{e,\lambda}$, and is equal to the sum of $K_{s,\lambda}$ and $K_{a,\lambda}$. The absorptive and scattering properties of particle clouds are often expressed in terms of an equivalent cross section per particle. The coefficient, K_λ , has the units of reciprocal length or area per unit volume. It can therefore be expressed as the product of the number of particles per unit volume times an effective cross-sectional area per particle. Thus, the absorption cross section, $\sigma_{a,\lambda}$, scattering cross section, $\sigma_{s,\lambda}$, and extinction cross section, $\sigma_{e,\lambda}$, are defined as:

$$N\sigma_{a,\lambda} = K_{a,\lambda} \quad (D-2)$$

$$N\sigma_{s,\lambda} = K_{s,\lambda} \quad (D-3)$$

$$N\sigma_{e,\lambda} = K_{e,\lambda} \quad (D-4)$$

where N is the number of particles per unit volume. When both absorption and scattering take place and the material is homogeneous, Eq. (1) can be written in terms

of these cross sections as:

$$I_{\lambda} = I_{a,\lambda} \exp \left[-N (\sigma_{a,\lambda} + \sigma_{s,\lambda}) \ell \right] \quad (D-5)$$

The attenuation of radiation by solid particles may be calculated theoretically using Maxwell's equations. The solution depends on the following dimensionless quantities: the ratio of the characteristic particle dimension to the wavelength of the radiation; the complex refractive index, and the particle shape. The rigorous solution of Maxwell's equations for the case of a plane wave incident on a homogeneous sphere was obtained by Mie (Ref. 18). A transformation of the basic Mie equations to a form suitable for machine calculations is given in Ref. 22. This transformation was used in Ref. 13 to calculate $\sigma_{a,\lambda}$, $\sigma_{s,\lambda}$, and $\sigma_{e,\lambda}$ as a function of the radiation wavelength and particle radius for fifteen types of small spherical particles.

Materials such as tungsten and carbon are of possible interest as seed materials in the nuclear light bulb engine. Experimental measurements of the absorption and scattering characteristics of clouds of these materials have been reported in Refs. 11, 16 and 20.

The absorption and scattering characteristics of an absorbing-scattering medium can also be expressed in terms of the mass extinction coefficient, $b_{e,\lambda}$, where $b_{e,\lambda}$ is the sum of $b_{a,\lambda}$ and $b_{s,\lambda}$ the mass absorption and scattering coefficients, respectively. These represent cross sections per unit mass of each particle. They are defined as:

$$\frac{\sigma_{e,\lambda}}{\rho V} = b_{e,\lambda} \quad (D-6)$$

$$\frac{\sigma_{a,\lambda}}{\rho V} = b_{a,\lambda} \quad (D-7)$$

$$\frac{\sigma_{s,\lambda}}{\rho V} = b_{s,\lambda} \quad (D-8)$$

where ρ is the mass density of the particle material and V is the volume of the particle. Equation 5 can be written in terms of the mass extinction coefficient, $b_{e,\lambda}$, the density of the solid particle seeds, ρ_s , and the mass of seed material per unit volume of the medium, as:

$$I_{\lambda} = I_{0,\lambda} \exp [-\rho_s b_{e,\lambda} \ell] \quad (D-9)$$

In the absence of optical interference between particles the total monochromatic absorption coefficient, $K_{a,\lambda}$, and the total monochromatic scattering coefficient, $K_{s,\lambda}$, are the sum of the contributions of particles of a given size, therefore;

$$\bar{K}_{a,\lambda} = \int_0^{\infty} N(r) \sigma_{a,\lambda}(r) dr \quad (D-10)$$

and

$$\bar{K}_{s,\lambda} = \int_0^{\infty} N(r) \sigma_{s,\lambda}(r) dr \quad (D-11)$$

where $N(r)$ is the number of particles of radius r and $\sigma_{a,\lambda}(r)$ are the absorption and scattering cross sections of particles of radius, r . The conditions under which optical interference between particles can be neglected have been cited as a center-to-center separation distance of 3 particles radii (Ref. 23). The attenuation for a cloud of different sized particles can be written as:

$$I_{\lambda} = I_{0,\lambda} \exp [-\bar{K}_{e,\lambda} \ell] \quad (D-12)$$

where

$$\bar{K}_{e,\lambda} = \bar{K}_{a,\lambda} + \bar{K}_{s,\lambda}$$

The extinction for a beam of multiple wavelengths may be expressed as

$$I = \int_0^{\infty} I_{a,\lambda} \exp [-\bar{K}_{e,\lambda} \ell] d\lambda \quad (D-13)$$

As discussed previously the loss of radiant energy from a beam of radiation energy transmitted through a medium is equal to the sum of losses due to the absorption and scattering. If the radius of particles in the medium are of the order or larger than the wavelength of the light passing through the medium, most of the radiation is scattered in the forward direction. This scattered radiation can be considered to be part of the radiation actually transmitted. Thus, the attenuation

is primarily due to absorption within the medium and,

$$I = \int_0^{\infty} I_{0,\lambda} \exp[-\bar{\kappa}_{a,\lambda} l] d\lambda \quad (D-14)$$

If $\bar{\kappa}_a$ is independent of wavelength, then the Eq. (8) can be integrated to obtain:

$$\frac{I}{I_0} = \exp[-\bar{\kappa}_a l] \quad (D-15)$$

Substituting the expression for the mass extinction coefficient and the particle density, Eq. (9) becomes,

$$\frac{I}{I_0} = \exp[-\rho_s \bar{b}_e l] \quad (D-16)$$

In the propellant heating tests (see Section V) the radiation incident on the particle cloud, I_0 , was determined by measuring the light transmitted through the test section in the absence of seeded gas. With the same light source, seed material was introduced into the test stream and the light transmitted, I , through the stream was measured. The carbon weight flow rate and the carrier gas velocity were also measured. These quantities and the test section dimensions were used to calculate the seed density, ρ_s , for a test condition. The experimental value of the mass attenuation coefficient, β , was calculated using the measured values of I , I_0 , ρ_s , and l . The values of β obtained represent an average value over all wavelengths of light emitted from the source. Experimental measurements for clouds of carbon and tungsten particles (Refs. 11, 1b, and 20) similar to those employed in the present studies indicate that β is approximately constant over a wide range of wavelengths. Values of β in the test discussed in Section V ranged from 678 cm²/g to 1990 cm²/g. These compare to values for dispersals of carbon particles of 7000 cm²/g to 50,000 cm²/g reported in Refs. 2, 6, and 11. The higher values of β were obtained by applying aerodynamic shear to the particle-laden fluid stream. In the initial cold-flow model tests reported in Section V attempts to use aerodynamic shear to deagglomerate the particle stream at the inlet of the test section were unsuccessful. In future tests, higher values of β may be obtained by the application of aerodynamic shear at a point other than at the inlet to the test section.

TABLE I

GEOMETRIES OF CONFIGURATIONS EMPLOYED IN TESTS





Type of Configuration	Peripheral-Wall Geometry			Propellant Duct Geometry		End-Wall Geometry			Vortex Injection Geometry			Figures Used to Describe Geometries	Figures Presenting Results of Tests
	Type of Wall	Wall Inner Diameter, in.	Wall Thickness, in.	Buffer Layer Thickness, in. Inner	Outer	Seed Inlet Duct Width, in.	Outer Diameter, in.	Thru-Flow Ports	Injection Location	Configuration	Total Injection Area, sq in.		
Radiant Energy Source	2 concentric fused silica coolant tubes 	2.24	0.079	-	-	-	0.080	0.185-in.-dia ports at center of each end wall	Near peripheral wall at one or both ends (see text)	8 or 16 0.10-in.-ID tubes equally spaced on a 1.44-in.-dia circle	0.0628	10	11, 12, 13, 14, 15, 16, 17, 18, 19, 20, 21
Transparent-Wall Model	54 axial fused silica coolant tubes 	1.26	0.010 and 0.005	-	-	-	0.625	0.075-in.-dia ports at center of each end wall	Peripheral wall at 120-deg intervals around circumference	69 0.020-in.-dia ports at each of three circumferential locations	0.0217	22a	24, 25, 26, 29
Simulated Propellant heater	42 axial fused silica coolant tubes 	0.95	0.005	0.438	0.118	0.039	0.625	0.039	Near peripheral wall at one end	8 0.054-in.-ID tubes equally spaced on a 0.875-in.-dia circle	0.0183	39	26, 27, 28, 29
D-C arc heater tests	2 concentric fused silica coolant tubes 	1.06	0.060	0.253	0.118	0.039	0.250-in.-dia cathode end	0.500-in.-dia port at anode end	At cathode end	16 0.015-in.-dia ports with variable injection angle	0.0028	36	40, 41, 42, 43

TABLE II

TYPICAL OPERATING PROCEDURE FOR THE 1.2-MEGW
R-F INDUCTION HEATER

1. 1.2-megw r-f induction heater system was turned on.
2. The r-f drive system was pretuned for the proper resonant frequency.
3. All diagnostic and recording equipment was turned on.
4. All cooling water and gas systems were turned on and preset to the desired starting conditions.
5. The auxiliary d-c starter system was turned on and both electrodes were indexed into contact position.
6. The d-c voltage supplied to the power amplifiers (see Fig. 2) were increased to 3.5 kv by varying the saturable reactor.
7. The d-c starter system was activated.
8. The starter electrode assemblies were removed from the end-wall thru-flow ports.
9. The r-f drive system was then retuned to compensate for the resonant frequency change due to the presence of the r-f plasma discharge within the r-f work coils.
10. Known concentrations of nigrosine dye were added to the annular cooling water.
11. The r-f input power, argon weight flow rate to the vortex injector system and chamber pressure were increased to the level desired for a particular test condition.
12. All required measurements and data acquisition were taken at a particular test condition with an average run time of about 1 hr.
13. The r-f power was reduced to a moderately low level prior to extinguishing the plasma. This eliminated the possibility of induced thermal stress in the fused silica tubes due to a too rapid high-power shut-down.

TABLE III

SUMMARY OF TEST CONDITIONS ABOVE $Q_T = 100$ KW FOR
DATA SHOWN IN FIGS. 15 THROUGH 19

Different Dye Concentrations were
Employed in the Following Tests

Q_T -kw*	P_D -atm	W_A -lb/sec	d-in.	A_S -sq in.	V-in. ³	Q_R -kw	Q_W -kw	Q_E -kw	Q_L -kw
102.03	7.2	0.036	0.727	3.75	0.54	1.96	74.70	23.24	2.13
104.18	8.7	0.028	0.845	4.40	0.75	8.37	66.20	27.43	2.18
104.60	5.5	0.021	0.760	3.96	0.60	8.09	65.90	28.40	2.20
104.81	6.0	0.024	0.810	4.20	0.68	4.73	62.50	35.40	2.18
105.77	6.0	0.022	0.845	4.42	0.75	7.13	67.13	29.31	2.20
109.11	7.0	0.029	0.680	3.53	0.47	5.51	65.20	36.10	2.30
112.57	14.0	0.024	0.870	4.55	0.80	6.29	82.25	21.70	2.33
112.64	16.0	0.039	0.810	4.20	0.68	7.24	78.40	24.60	2.40
112.86	7.0	0.022	0.680	3.52	0.47	9.46	71.30	29.80	2.30
116.16	15.0	0.030	0.850	4.43	0.77	6.64	84.80	22.30	2.42
126.14	7.0	0.025	0.727	3.75	0.54	7.13	85.50	30.97	2.54
132.61	6.8	0.027	0.720	3.71	0.54	5.58	81.60	42.80	2.63
132.63	5.0	0.028	0.711	3.69	0.52	8.10	88.30	33.60	2.63
146.80	8.0	0.030	0.820	4.30	0.70	9.03	77.14	57.90	2.77
151.15	8.0	0.039	0.765	3.98	0.61	8.45	92.50	47.40	2.80
152.31	13.0	0.032	0.720	3.71	0.54	10.20	99.18	40.10	2.83
161.54	8.0	0.037	0.790	4.11	0.65	8.80	99.10	50.70	2.94
163.10	9.5	0.028	0.720	3.71	0.54	16.00	110.00	34.20	2.90
176.06	8.0	0.029	0.770	4.00	0.62	15.50	115.50	42.10	2.96
180.50	8.5	0.041	0.730	3.80	0.55	11.20	110.00	56.10	3.20
184.45	9.0	0.041	0.805	4.20	0.68	10.35	118.00	53.00	3.10
193.00	8.0	0.038	0.845	4.40	0.75	11.40	121.00	57.40	3.20
198.20	8.5	0.039	0.880	4.60	0.82	13.50	123.00	58.40	3.30
204.70	8.5	0.032	0.830	4.30	0.72	17.75	137.00	46.80	3.10
215.90	8.5	0.030	0.820	4.26	0.71	18.00	147.00	47.00	3.90

$$*Q_T = Q_R + Q_W + Q_E + Q_L$$

TABLE IV

COMPARISON OF OPERATING CONDITIONS IN FULL-SCALE ENGINE WITH
HIGHEST POWER RADIANT ENERGY SOURCE TEST AND MODEL TESTS

	Unit Cavity Full-Scale Engine ^a		Highest Power Radiant Energy Source Test	MODEL	
	Reference Engine	Derated Engine		1.26-in.-ID Axial Coolant-Tube Model	0.095-in.-ID Axial Coolant-Tube Model
Transparent-wall configuration	Circumferential	Circumferential	Concentric Tubes	Axial	Axial
Inside diameter, ft	1.604	1.604	0.187	0.105	0.079
Length between containing end walls, ft	6.0	6.0	0.167	0.167	0.167
Length/Diameter ratio	3.75	3.75	0.893	1.59	2.11
Number of coolant tubes	3000	3000	1	54	42
Tube inside diameter, in.	0.050	0.050	2.24	0.040	0.040
Tube outside diameter, in.	0.060	0.060	2.38	0.050	0.050
Tube wall thickness, in.	0.005	0.005	0.070	0.005	0.005
Total tube surface area, ft ²	95.2	95.2	0.147 ^b	0.177 ^b	0.137 ^b
Cylindrical surface area, ft ²	30.2	30.2	0.147 ^b	0.082 ^b	0.062 ^b
Coolant fluid	Hydrogen	Hydrogen	Water-Dye	Water	Water
Buffer fluid	Neon	Neon	Argon	Argon	Argon
Buffer injection velocity, ft/sec	25 ^c	25 ^c	81	210	211
Buffer weight flow, lb /sec	2.96	2.96	0.030	0.012	0.003
Chamber pressure, atm	500	500	8.5	5	2.15
Equivalent black-body radiating temperature, R	15,000	8,000	10,200	-	-
Radiant energy flux per unit area, Btu/sec-ft ² kw/in. ²	24,300 178	1944 14.4	5000 36.7	- -	- -
Total heat flux deposited in wall, Btu/sec-ft ²	490	39.2	108.3	270	71.5
Thermal radiation from fuel, Btu/sec-ft ²	218	17.4	50.3 ^d	11 ^d	2.5 ^d
Conduction-Convection from fuel, Btu/sec-ft ²	26	2.1	58	259	(see text)
Reradiation from propellant, Btu/sec-ft ² (neglected)	-	-	-	-	-
Conduction-convection from propellant, Btu/sec-ft ²	246	19.7	0	0	(see text)

a Data obtained from Refs. 1 and 24

b Based on 3 in. length

c Assumed value of $v_1/v_j = 0.4$

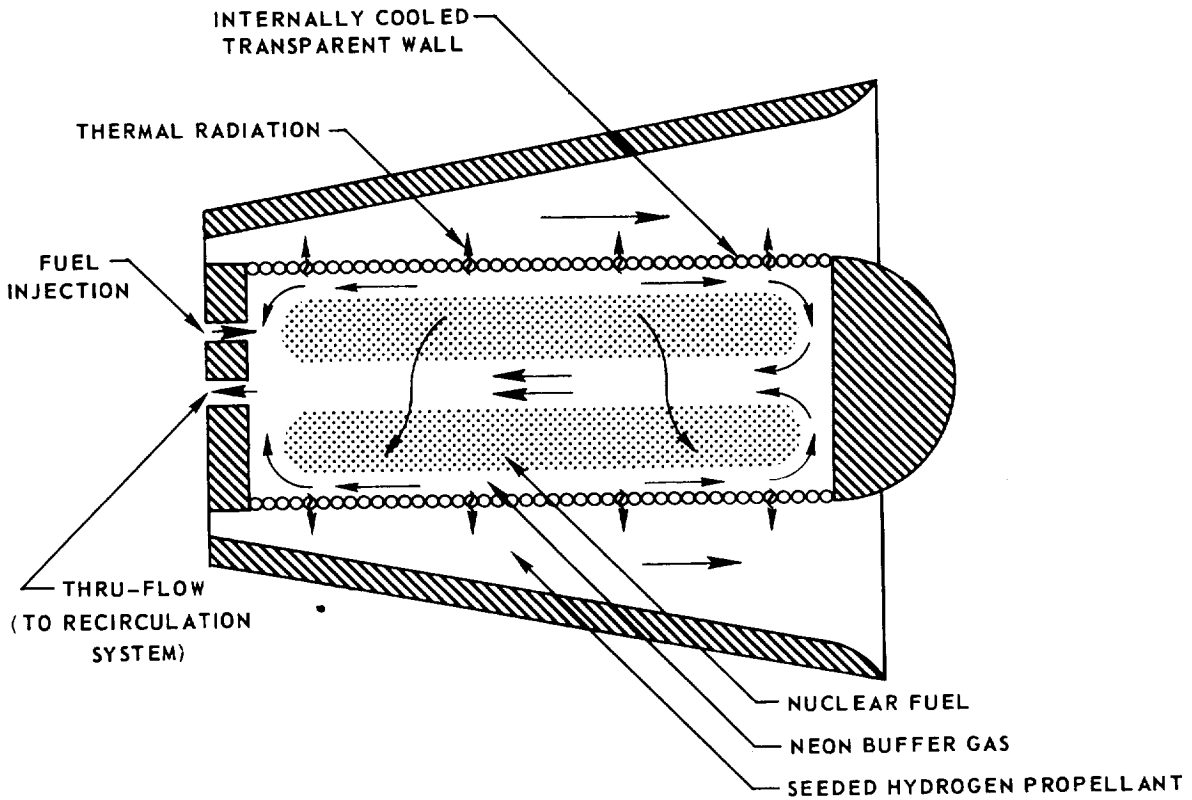
d Assumed 5 percent of total radiation was deposited in model and coolant fluid

TABLE V
 DIMENSIONAL CHARACTERISTICS OF FUSED SILICA TUBES USED IN TRANSPARENT-WALL MODELS

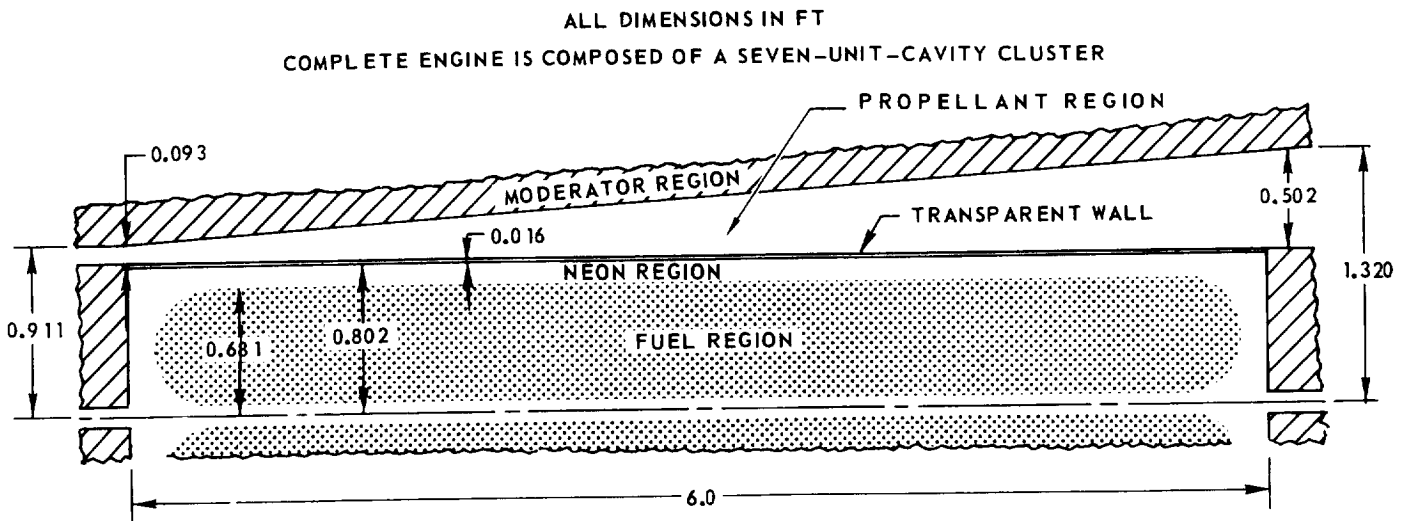
Vendor	Grade	Nominal Wall Thickness, in.	Measured Wall Thickness, in.			Average Nominal	Standard Deviation About Average, in.
			Maximum	Minimum	Average		
I	Commercial	0.005	0.0145	0.009	0.011	2.20	0.0012
		0.010	0.0135	0.007	0.011	1.10	0.0018
II	Commercial	0.005	0.0095	0.0055	0.007	1.40	0.0011
III	Commercial	0.005	0.0085	0.0035	0.0061	1.22	0.0011
		0.010	0.010	0.0075	0.009	0.90	0.0007
IV	Commercial	0.020	0.0185	0.011	0.017	0.85	0.0019
		0.020	0.026	0.020	0.022	1.10	0.0013

NUCLEAR LIGHT BULB ENGINE CONCEPT

a) UNIT CAVITY OF NUCLEAR LIGHT BULB ENGINE

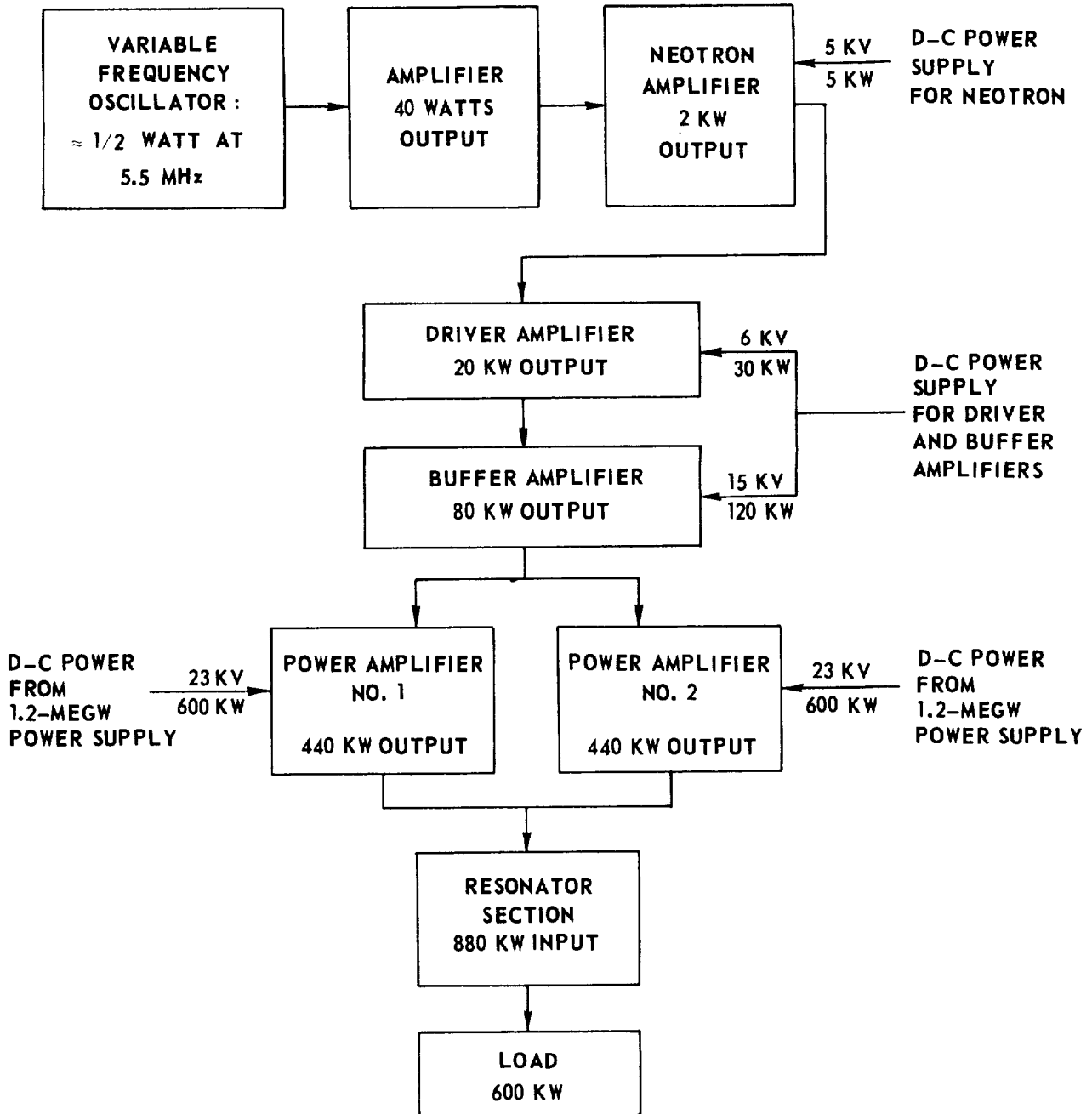


b) DIMENSIONS OF UNIT CAVITY IN REFERENCE ENGINE



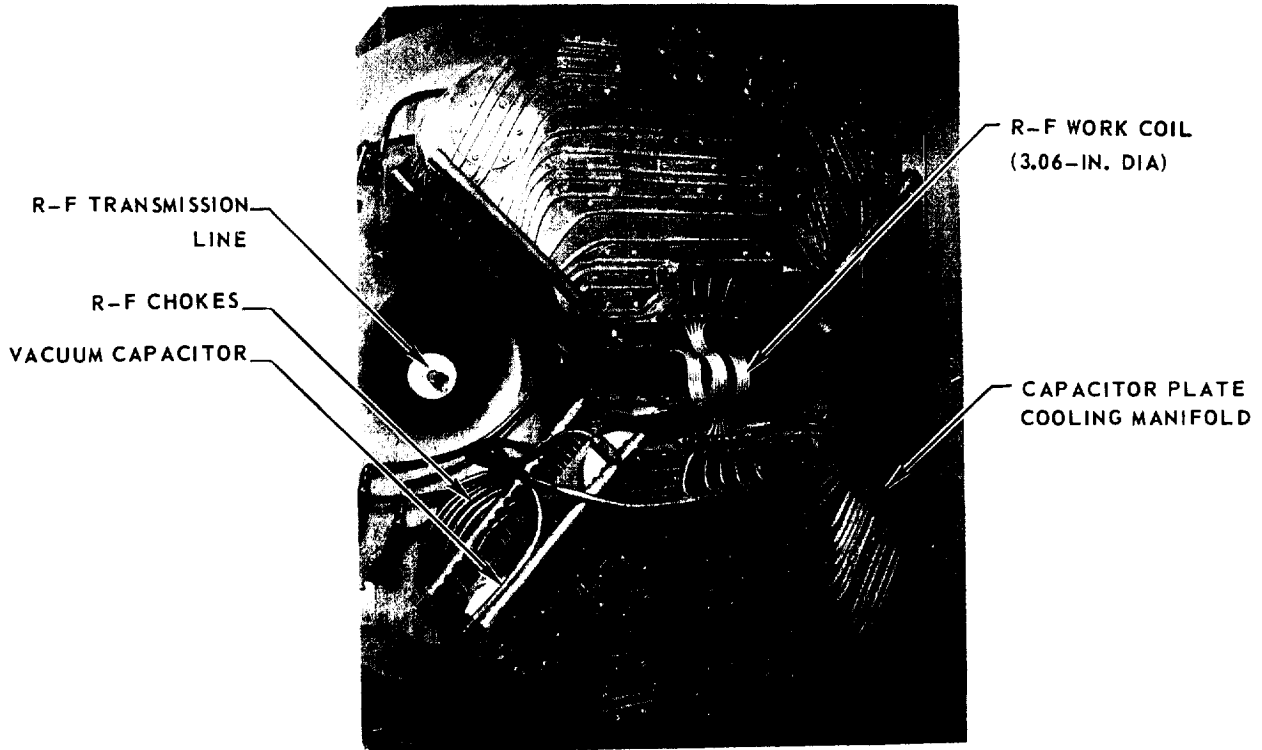
BLOCK DIAGRAM OF UARL 1.2-MEGW R-F INDUCTION HEATER

POWER LEVELS SHOWN ARE MAXIMUM DESIGN VALUES
 MAXIMUM TOTAL D-C INPUT POWER DURING THIS PROGRAM FOR POWER
 AMPLIFIERS 1 AND 2 WAS APPROXIMATELY 600 KW

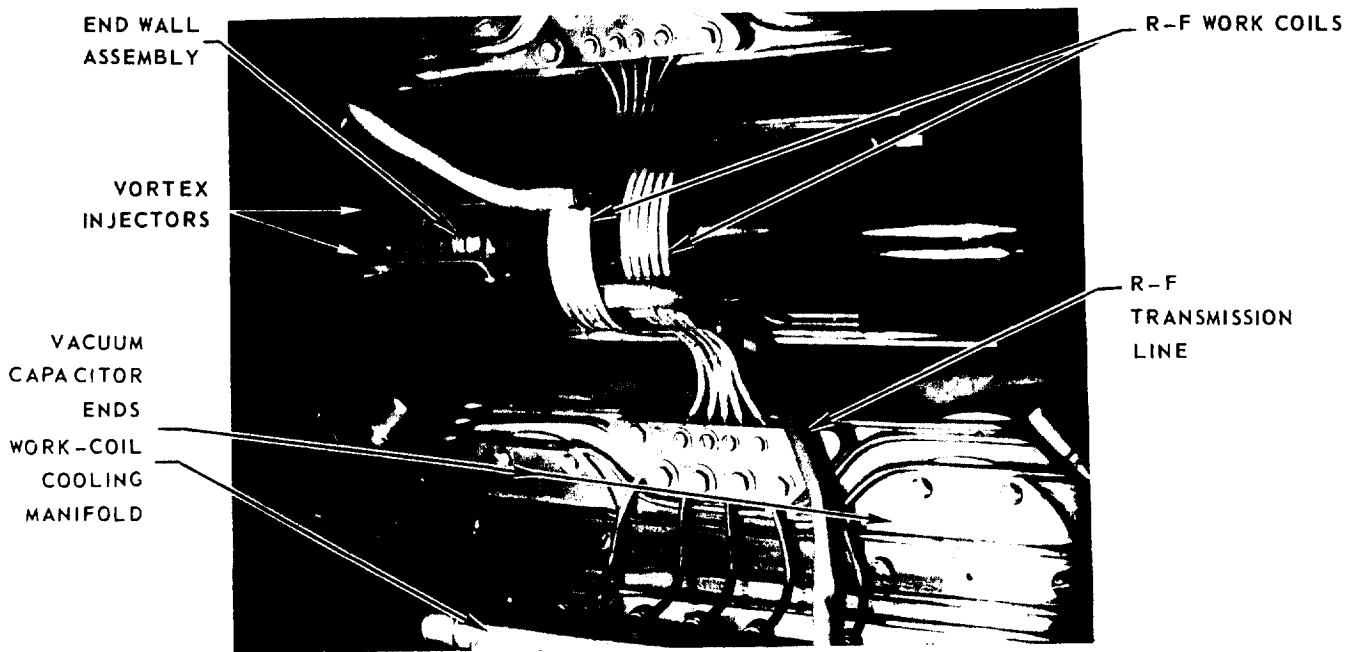


PHOTOGRAPHS OF 1.2-MEGW R-F INDUCTION HEATER RESONATOR SECTION

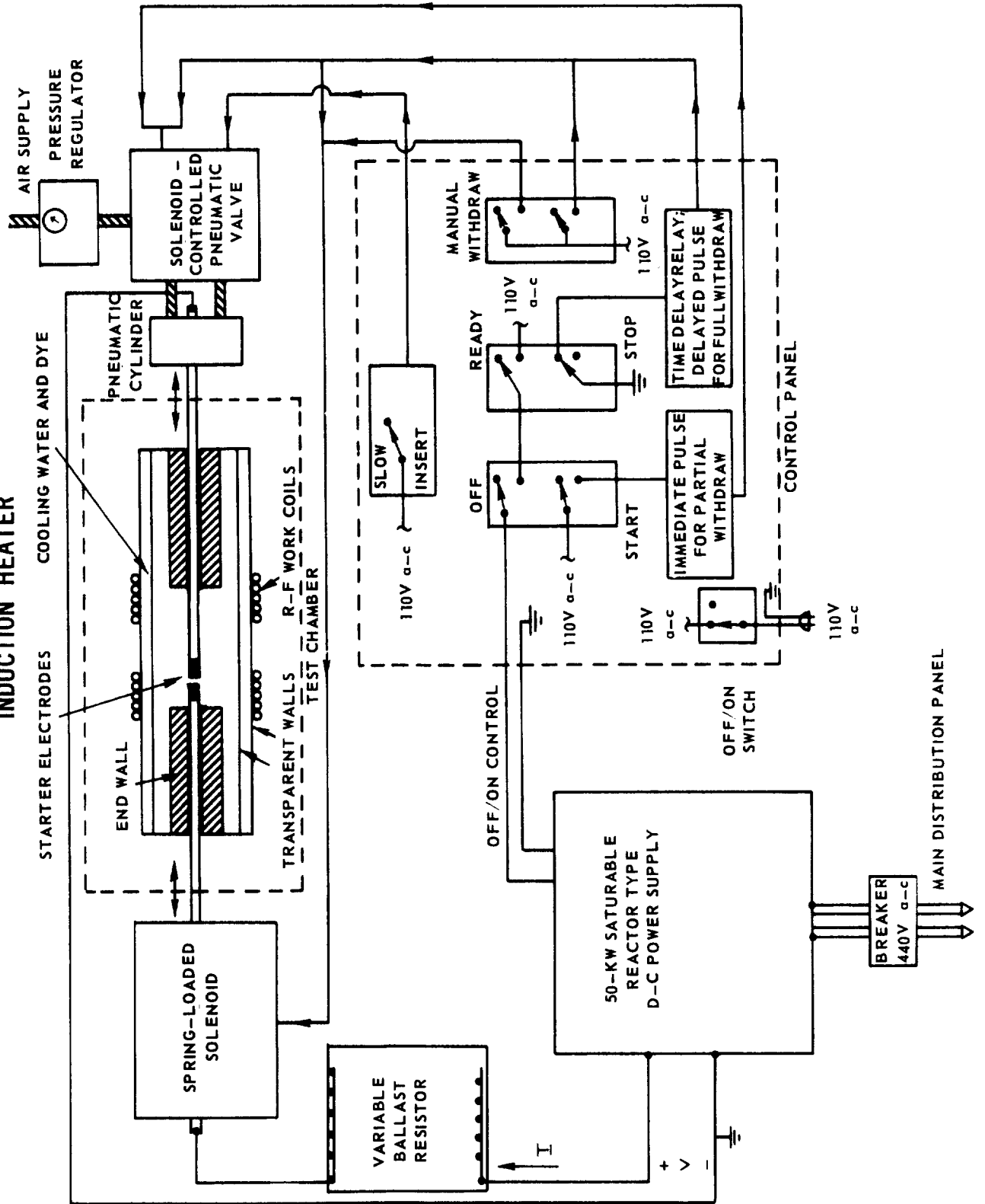
a) PARTIALLY ASSEMBLED RESONATOR



b) DETAILS OF R-F WORK COILS



BLOCK DIAGRAM OF TEST CHAMBER AND PLASMA STARTING SYSTEM FOR 1.2-MEGW R-F INDUCTION HEATER

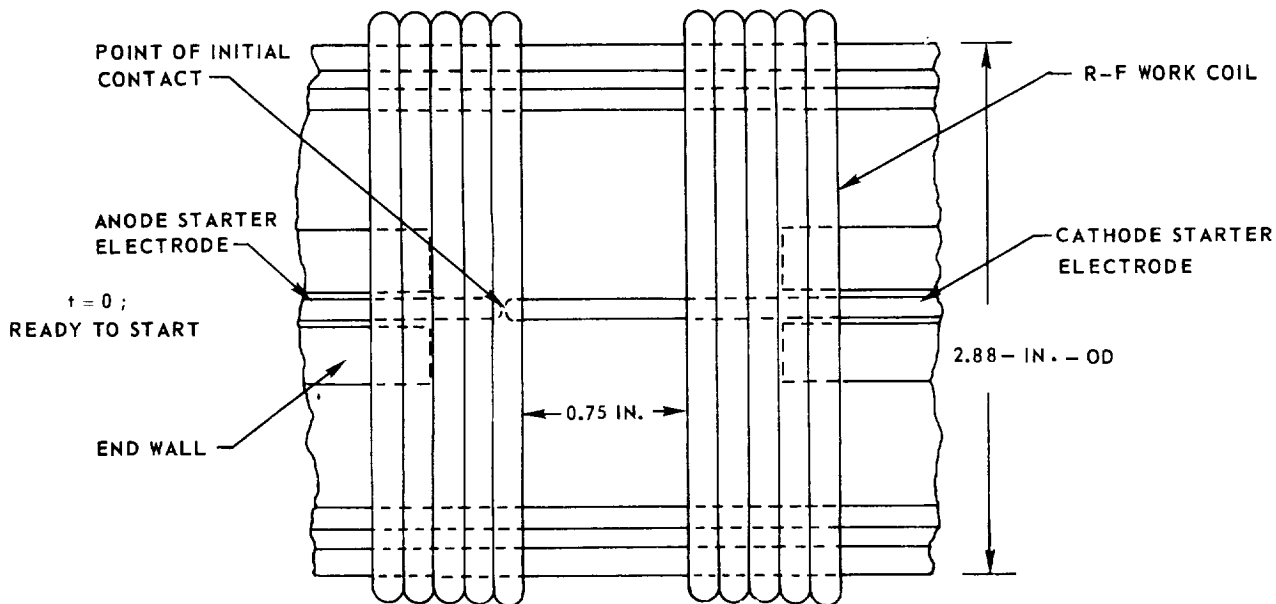


SCHEMATIC DIAGRAM OF TEST CHAMBER AND PHOTOGRAPHS OF R-F PLASMA STARTING SEQUENCE

1.2-MEGW R-F INDUCTION HEATER

SEE FIG. 4 FOR DETAILS OF R-F PLASMA STARTING SYSTEM

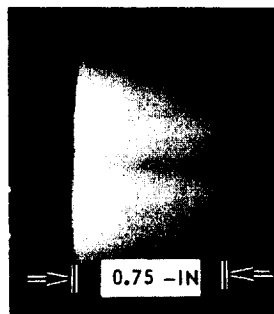
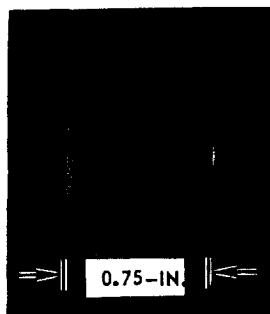
a) SCHEMATIC DIAGRAM



b) TYPICAL D-C ARC START ONLY

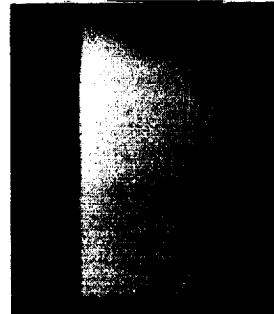
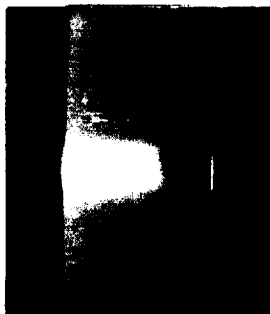
c) TYPICAL D-C TO R-F START

$t = 10$ mSEC ;
INITIATION
OF D-C ARC

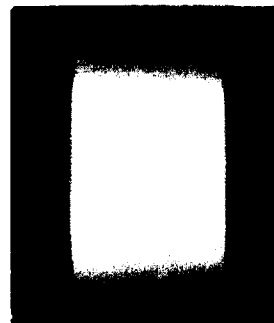
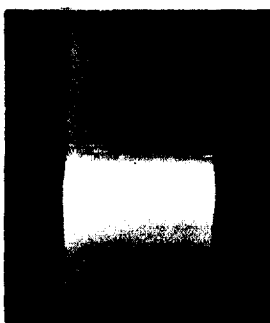


PARTIAL
R-F COUPLING
CHAMBER PRESSURE,
 $P_D = 5$ ATM

$t = 52$ mSEC ;
ELECTRODES
PARTIALLY
WITHDRAWN



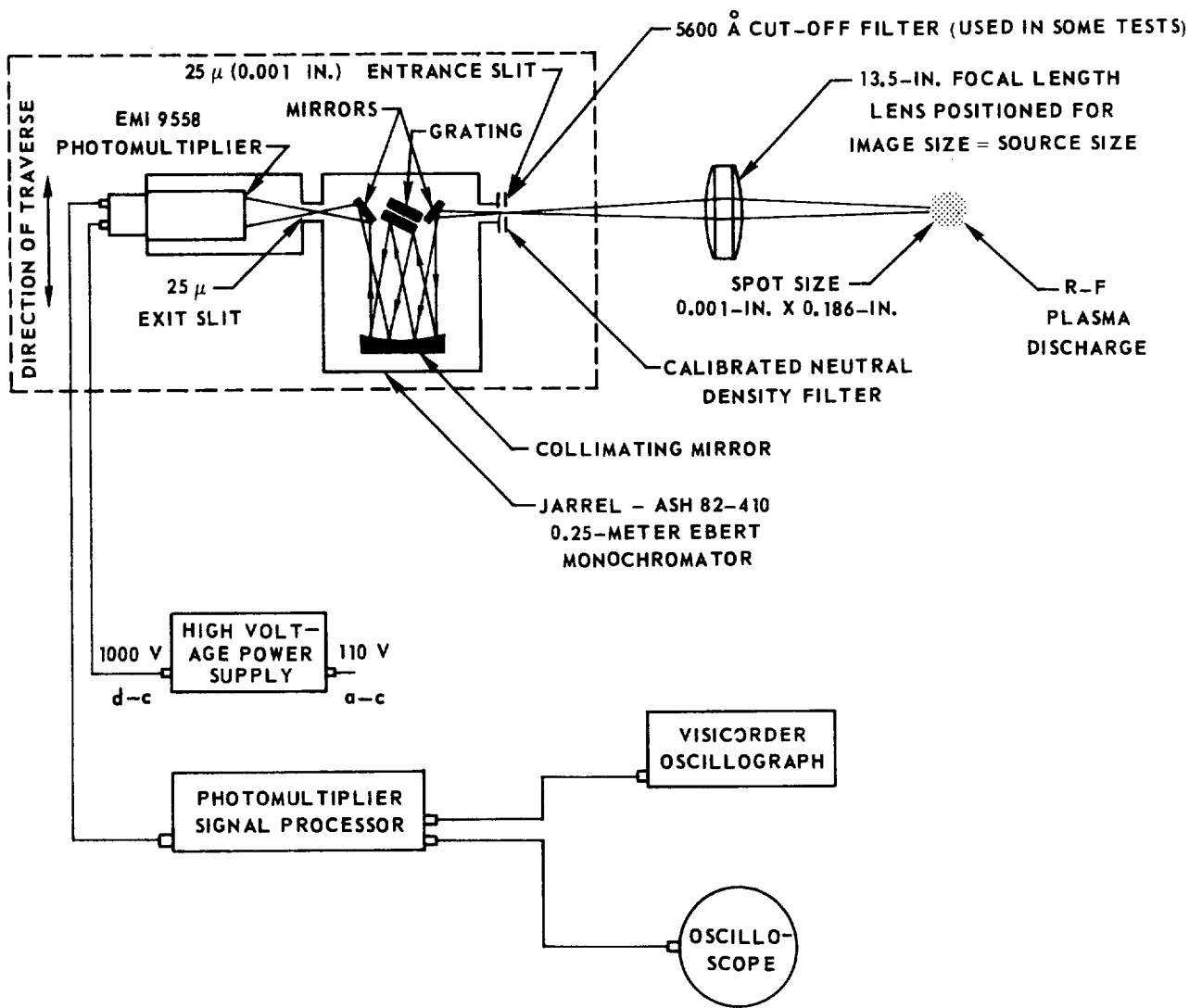
$t = 94$ mSEC ;
BOTH ELECTRODES
WITHDRAWN
INTO END WALLS



TOTAL R-F
PLASMA DISCHARGE
POWER = 60 KW

SCHEMATIC OF OPTICAL SYSTEM FOR SPECTRAL MEASUREMENTS

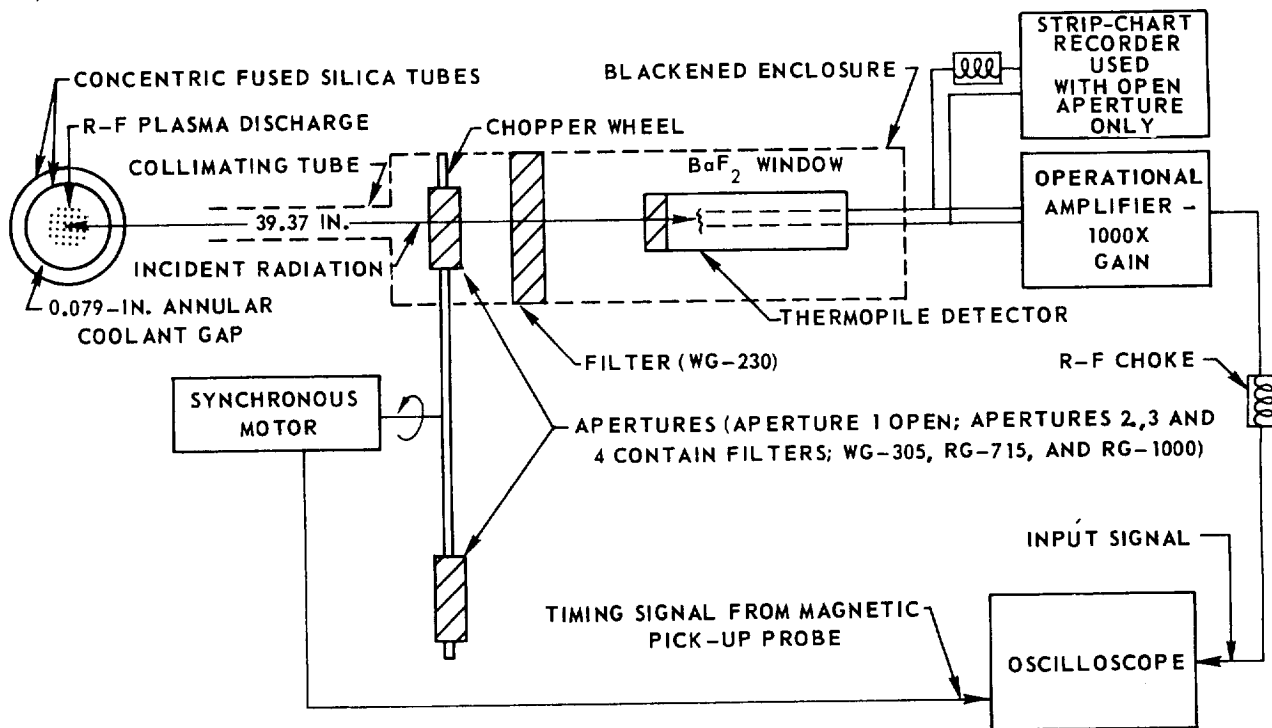
ALL EQUIPMENT WITHIN DASHED OUTLINE MOUNTED ON TABLE WITH SLIDE MECHANISM AND TRAVERSED TO PROBE ACROSS R-F PLASMA DISCHARGE



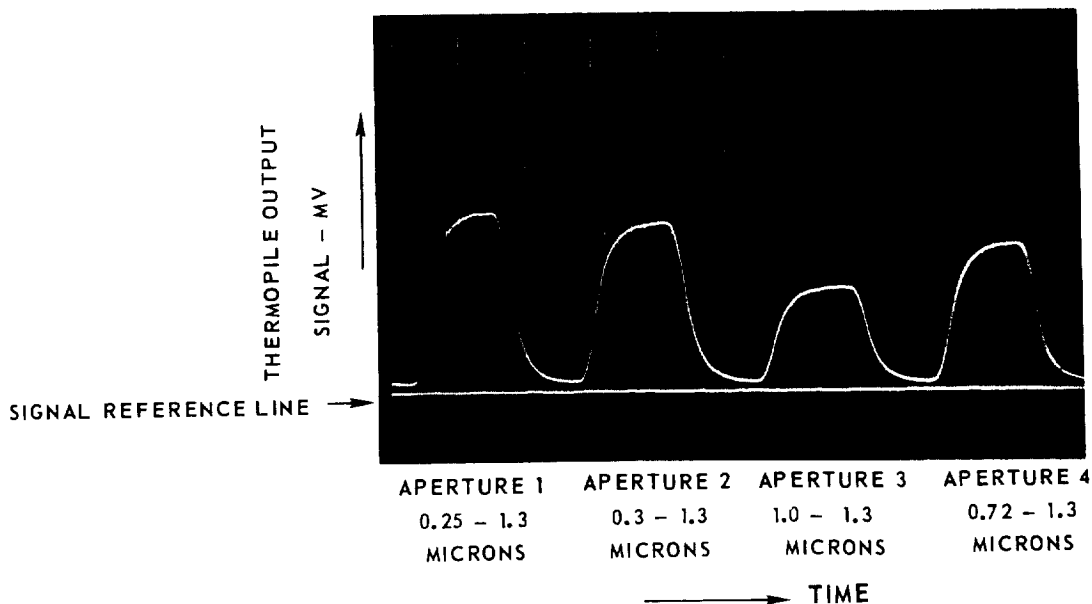
BLOCK DIAGRAM OF RADIOMETER OPTICAL SYSTEM AND OSCILLOSCOPE TRACE OF TYPICAL OUTPUT

SEE FIG. 8 FOR TRANSMISSION CHARACTERISTICS OF VARIOUS FILTERS

a) BLOCK DIAGRAM OF OPTICAL SYSTEM



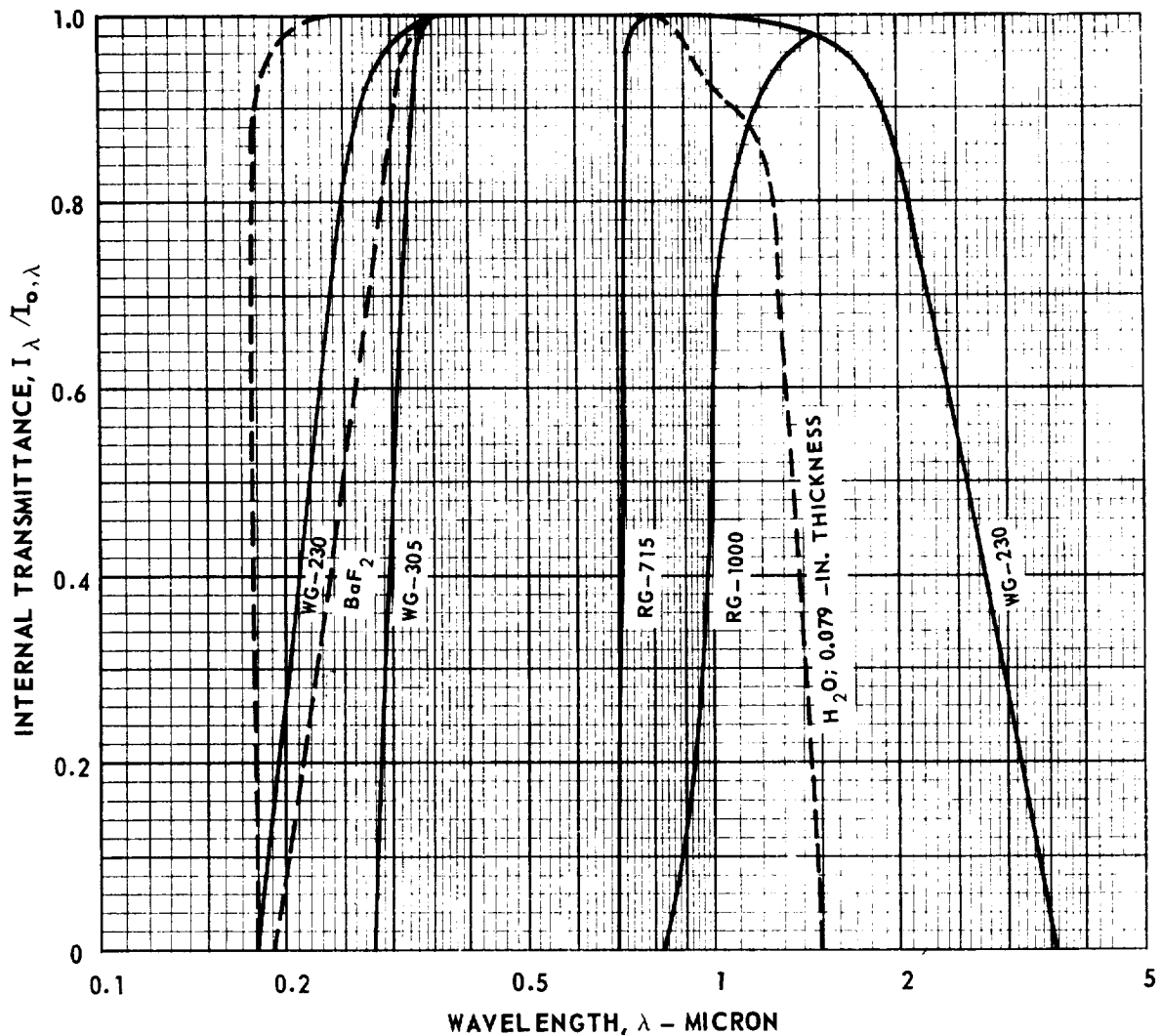
b) OSCILLOSCOPE TRACE USING CHOPPER WHEEL



TRANSMISSION CHARACTERISTICS OF FILTERS USED FOR RADIATION MEASUREMENTS

FILTER THICKNESS - 0.079 IN.
SEE FIG. 7 FOR RADIOMETER OPTICAL SYSTEM

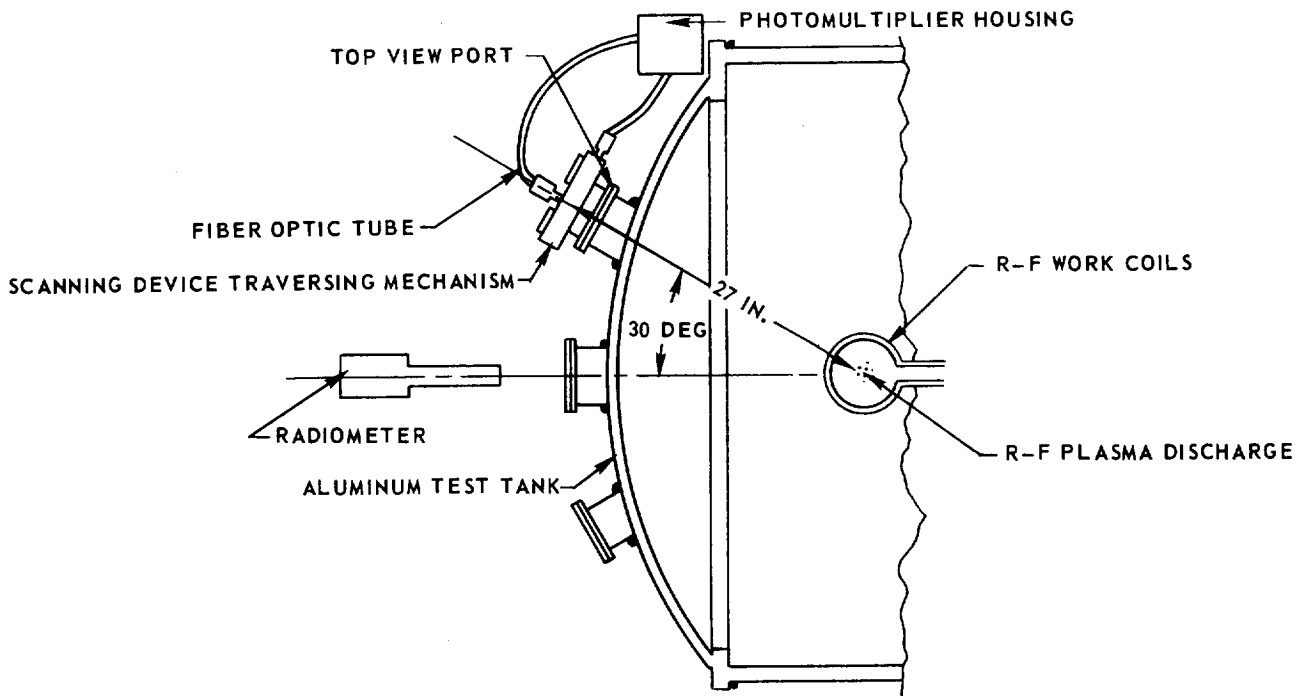
FILTER	MEASURED UPPER AND LOWER 50 PERCENT TRANSMISSION LEVELS, λ - MICRONS	
	LOWER CUT-OFF	UPPER CUT-OFF
BaF ₂ THERMOPILE DETECTOR	0.25	--
WG-305	0.30	2.6
RG-715	0.72	--
RG-1000	1.00	--
0.079-IN. THICK LAYER OF WATER	0.18	1.3
WG-230	0.22	2.6



SKETCH AND PHOTOGRAPH OF OPTICAL SCANNING SYSTEM FOR DISCHARGE DIAMETER DETERMINATION

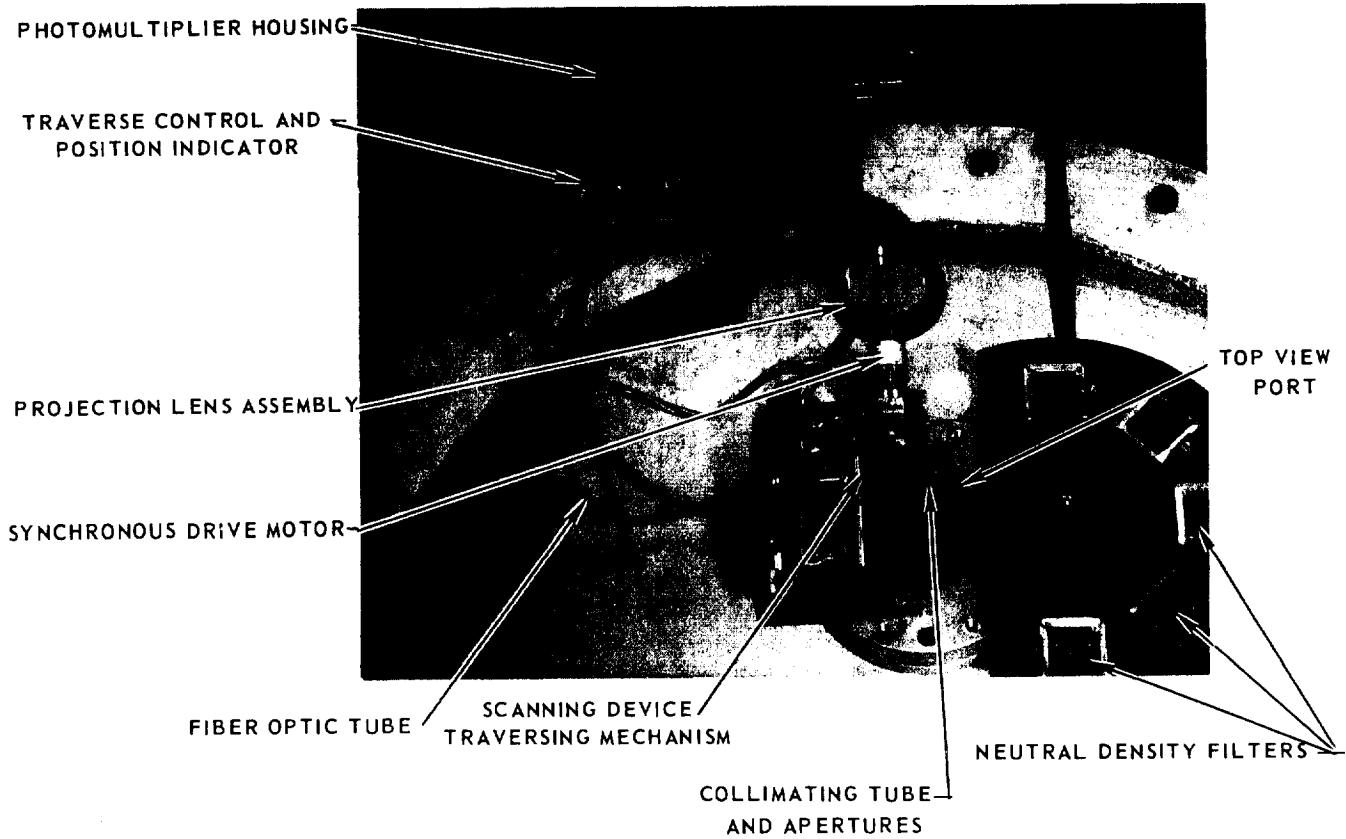
1.2-MEGW R-F INDUCTION HEATER

a) SKETCH OF SCANNING SYSTEM

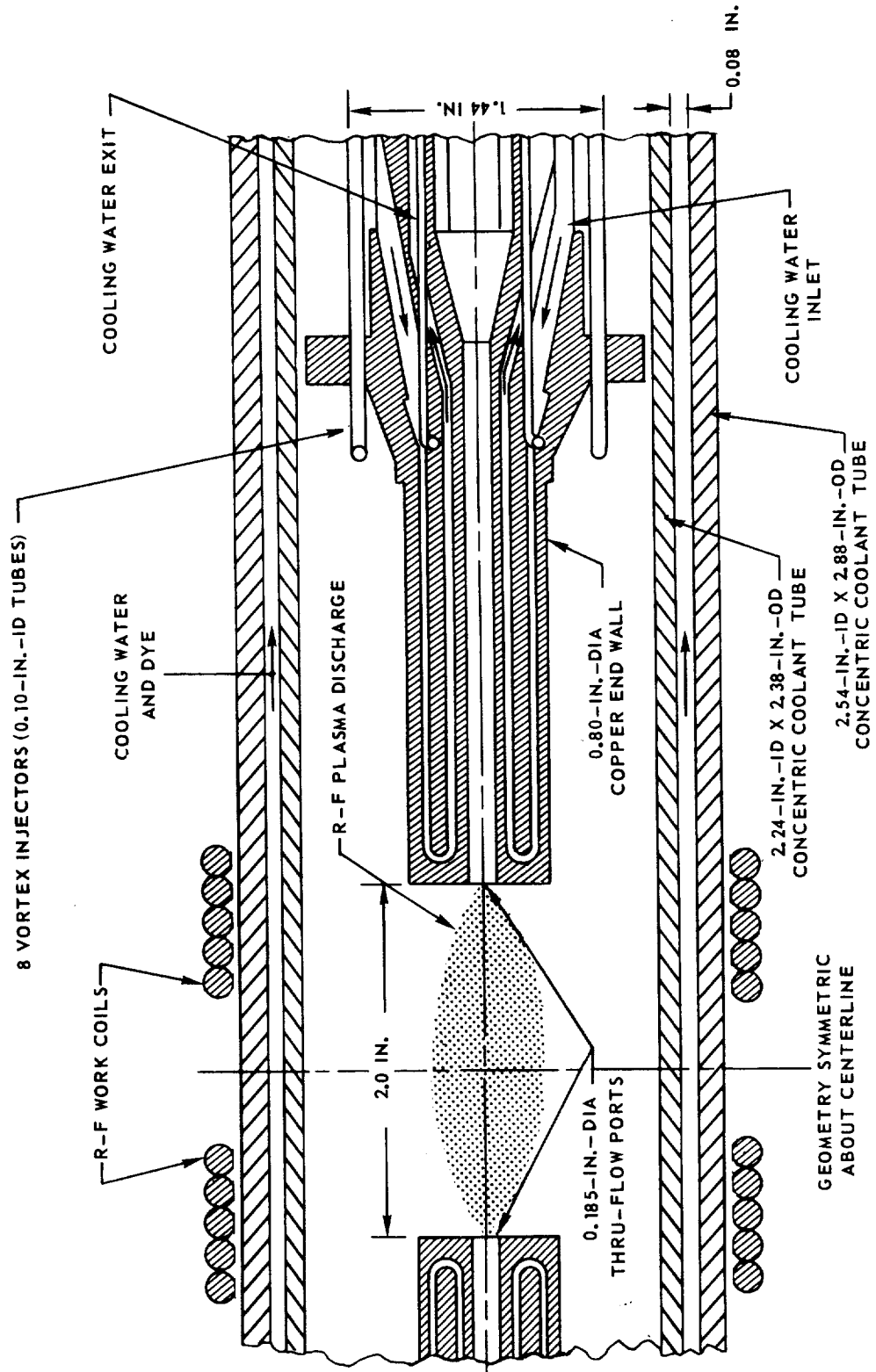


b) PHOTOGRAPH OF SCANNING SYSTEM

PHOTOMULTIPLIER OUTPUT DISPLAYED ON STRIP CHART RECORDER



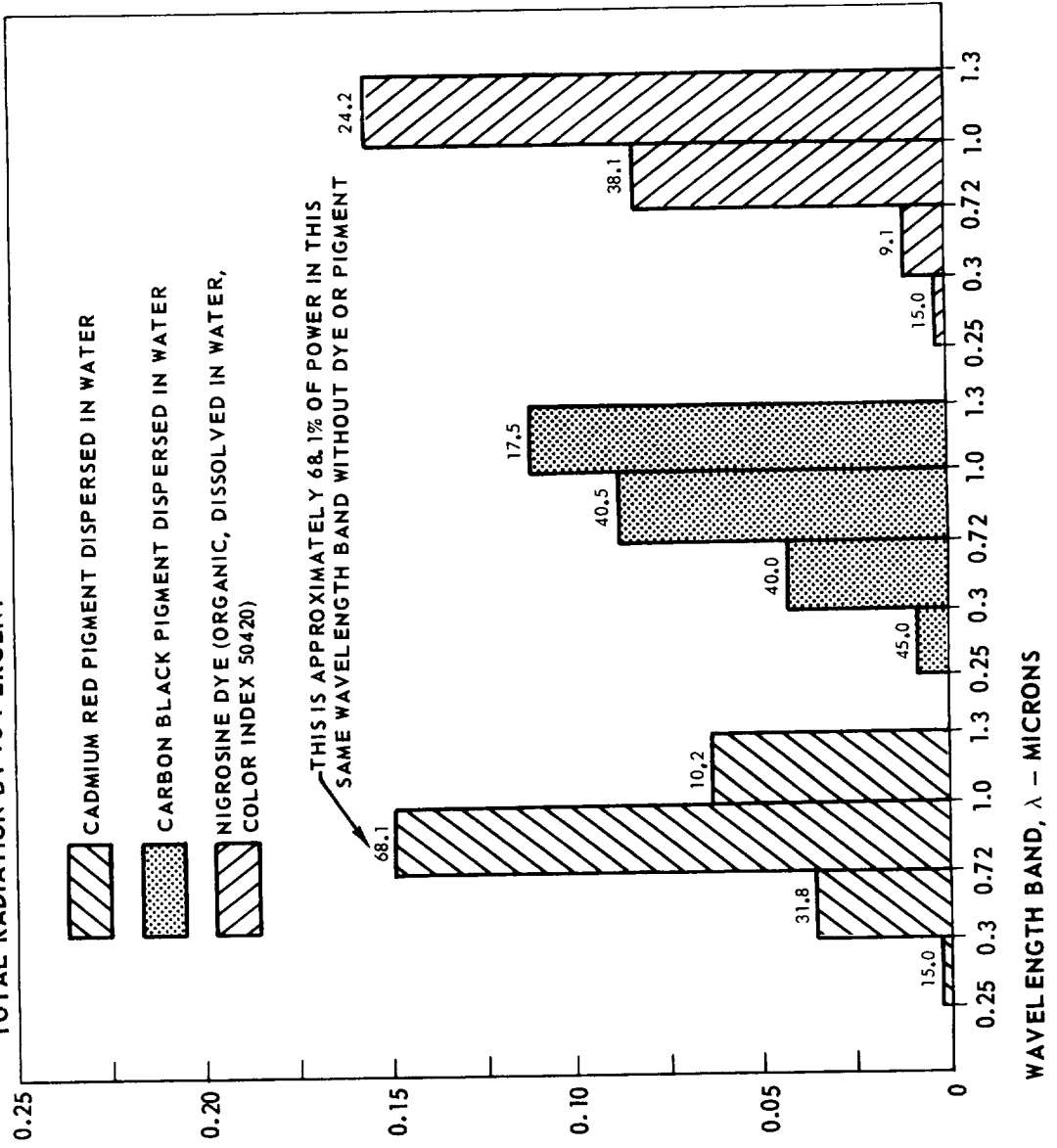
POSITION OF END WALLS AND TEST CHAMBER RELATIVE TO COILS OF 1.2-MEGW R-F INDUCTION HEATER



COMPARISON OF RELATIVE POWER TRANSMITTED THROUGH DYE AND PIGMENTS IN PERIPHERAL-WALL COOLING WATER

SEE FIG. 7 FOR BLOCK DIAGRAM OF OPTICAL SYSTEM ; STANDARD LAMP REPLACED R-F PLASMA DISCHARGE
NOTE DIFFERENCE IN ORDINATE SCALES

b) DYES AND PIGMENTS ADDED TO ANNULAR COOLANT (0.079-IN. GAP) TO REDUCE
TOTAL RADIATION BY 75 PERCENT



a) STANDARD LAMP ONLY

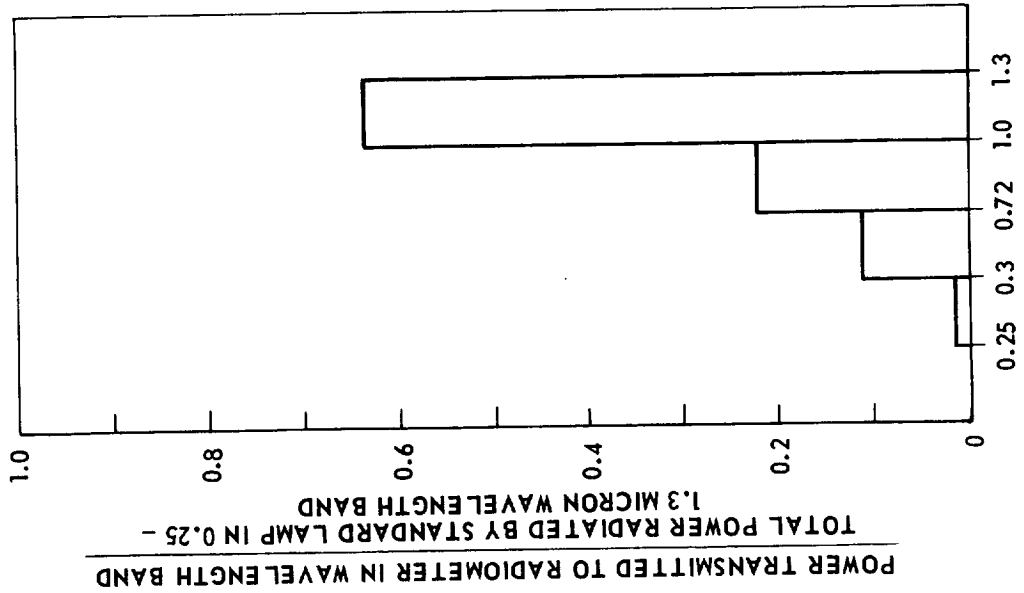
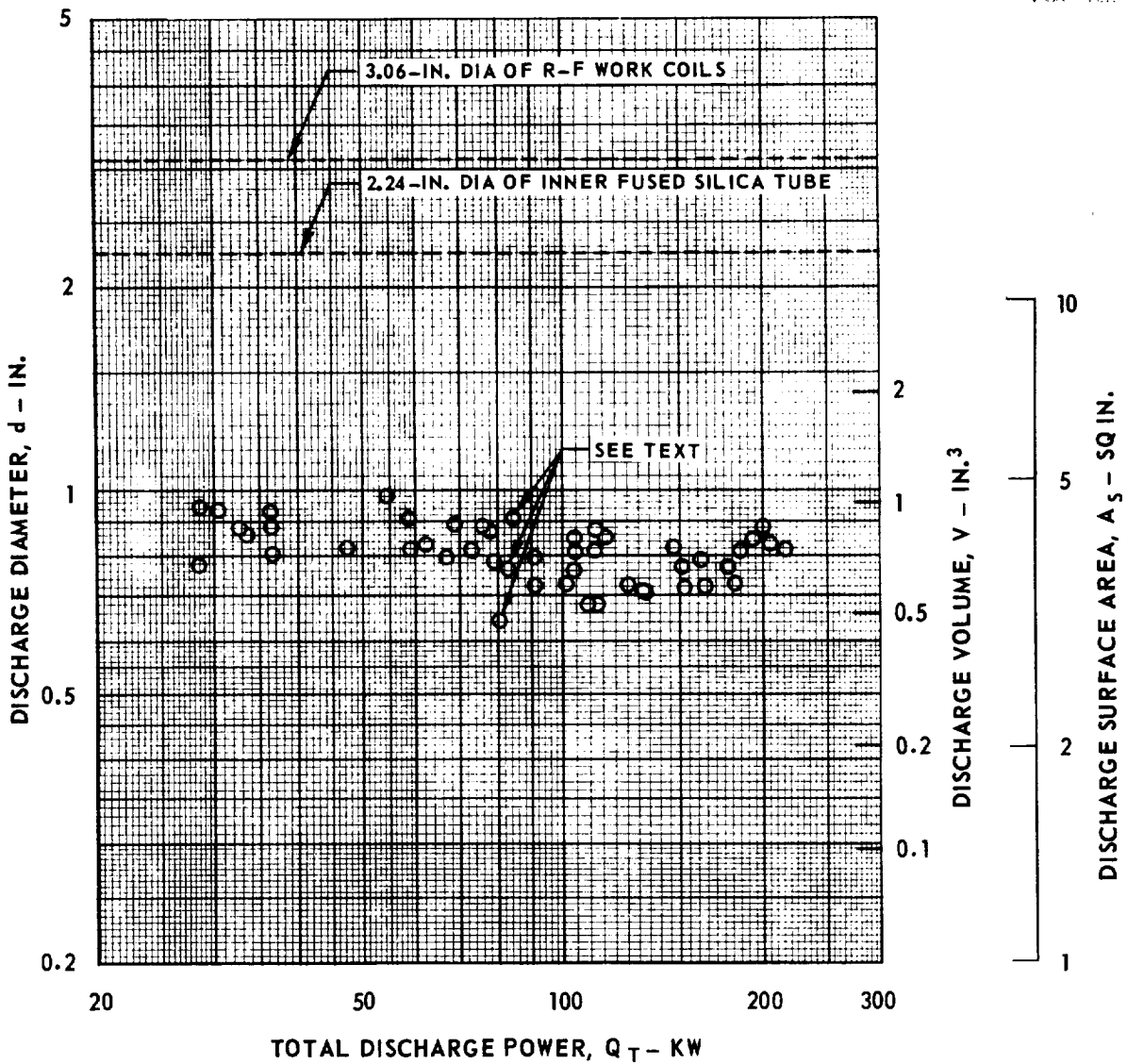


FIG. 11

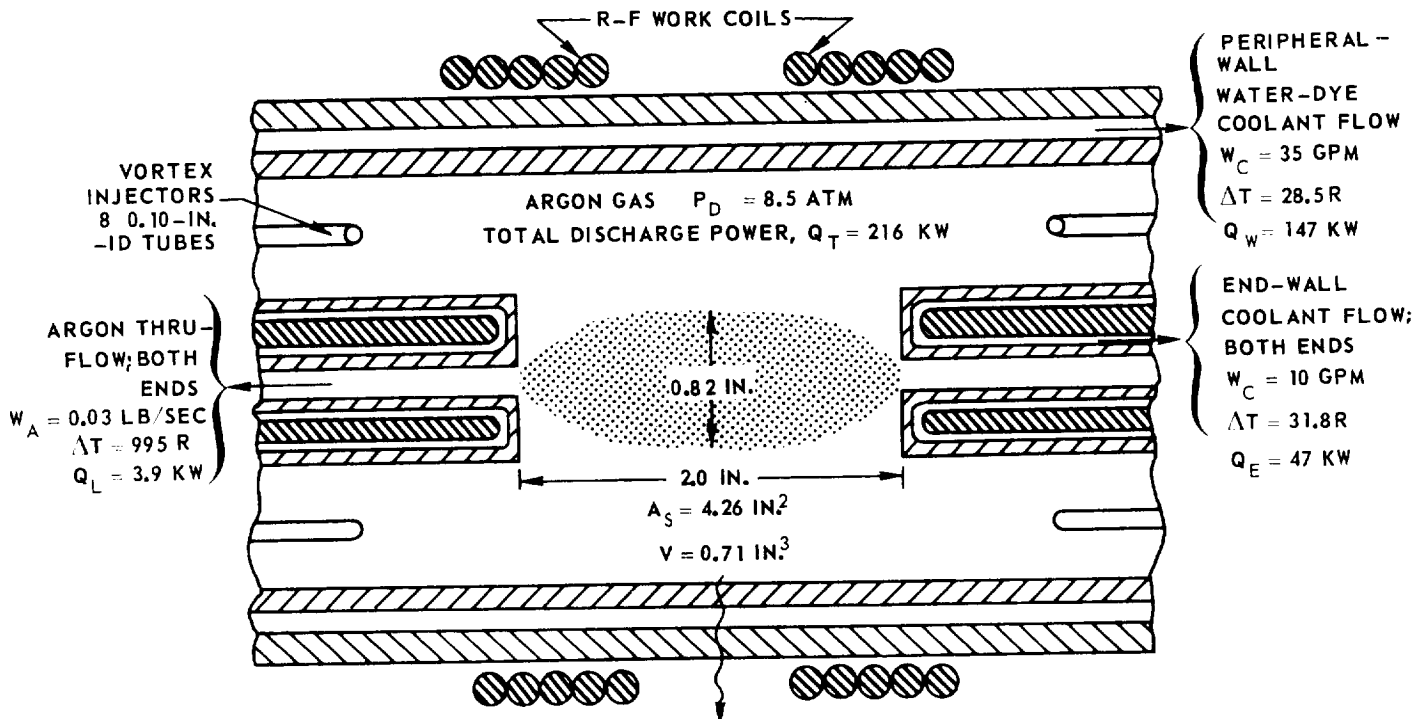
GEOMETRIC CHARACTERISTICS OF ARGON R-F PLASMAS OBTAINED IN RADIANT ENERGY SOURCE TESTS

1.2-MEGW R-F INDUCTION HEATER
 RANGE OF CHAMBER PRESSURE, $P_D = 2$ TO 16 ATM
 RANGE OF ARGON WEIGHT FLOW, $W_A = 0.010$ TO 0.041 LB/SEC
 SEE FIG. 10 FOR DETAILS OF TEST CONFIGURATION
 REFER TO TABLE III FOR DATA ABOVE $Q_T = 100$ KW



SKETCH OF END WALLS AND R-F PLASMA DISCHARGE SHOWING POWER LOSSES FOR HIGHEST POWER OPERATING POINT

1.2-MEGW R-F INDUCTION HEATER



$$Q_R = (8.6 \times 10^{-3} \text{ KW/MV}) (2.09 \times 10^3 \text{ MV}) = 18 \text{ KW}$$

$$\text{TOTAL D-C INPUT POWER, } Q_T = 600 \text{ KW AT } 5.51 \text{ MHz}$$

$$\text{TOTAL DISCHARGE POWER, } Q_T = 147 + 47 + 3.9 + 18 = 216 \text{ KW}$$

$$\text{R-F SYSTEM COUPLING EFFICIENCY, } \eta = 216/600 = 36\%$$

PROBABLE MAXIMUM POWER CONDUCTED THROUGH PERIPHERAL WALL, $Q_C = 9.0 \text{ KW}$ (SEE TEXT)

TOTAL POWER RADIATED THROUGH INNER PERIPHERAL WALL, $Q_{R,T} = 147 - 9 + 18 = 156 \text{ KW}$

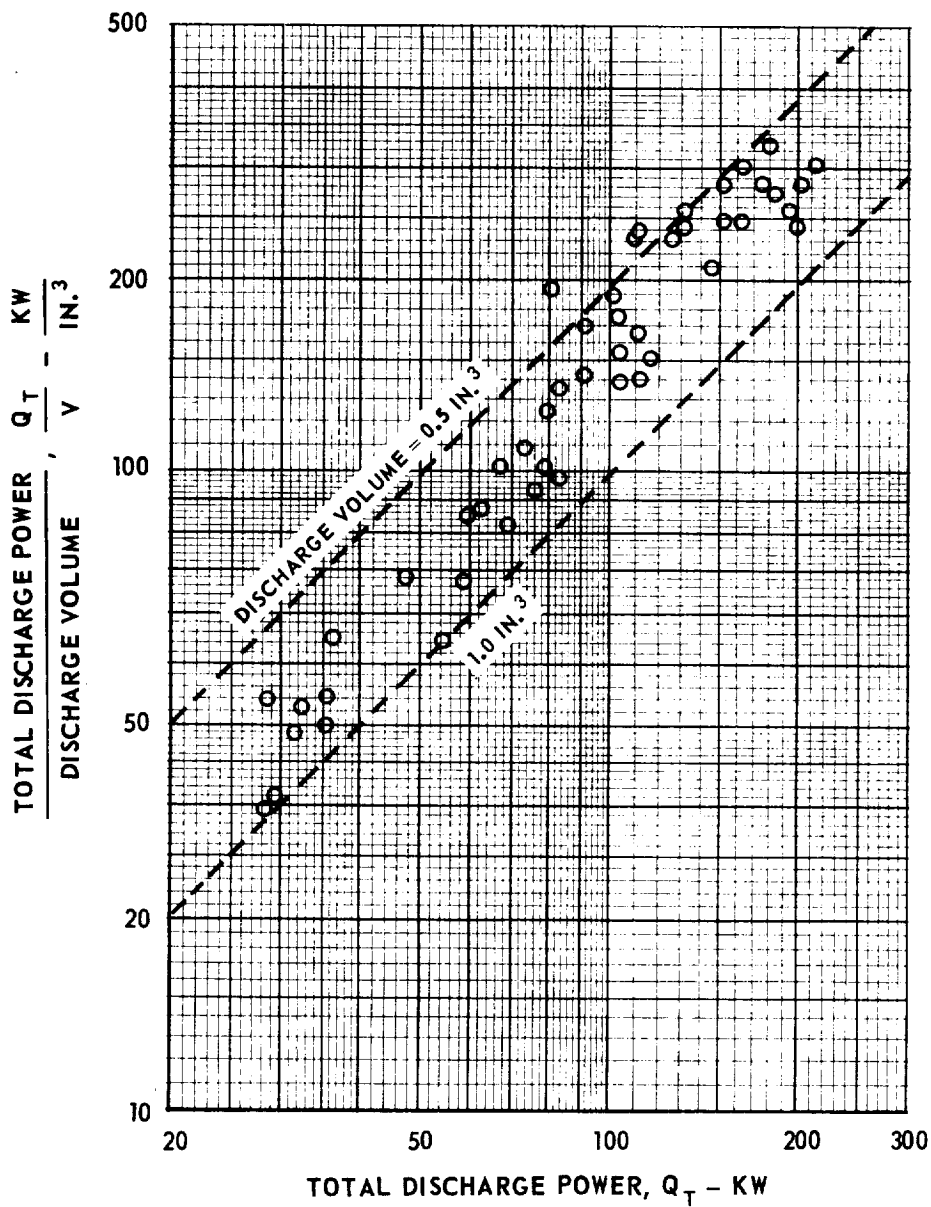
$$\phi_R = Q_{R,T}/A_S = 156/4.26 = 36.7 \text{ KW/IN.}^2 \quad (T^* = 10,200 \text{ R})$$

FRACTION OF DISCHARGE POWER RADIATED THROUGH INNER PERIPHERAL WALL

$$Q_{R,T}/Q_T = 156/216 = 0.72 \quad (F_{C,C} = 1 - 0.72 = 0.28)$$

VARIATION OF DISCHARGE POWER PER UNIT VOLUME WITH TOTAL DISCHARGE POWER

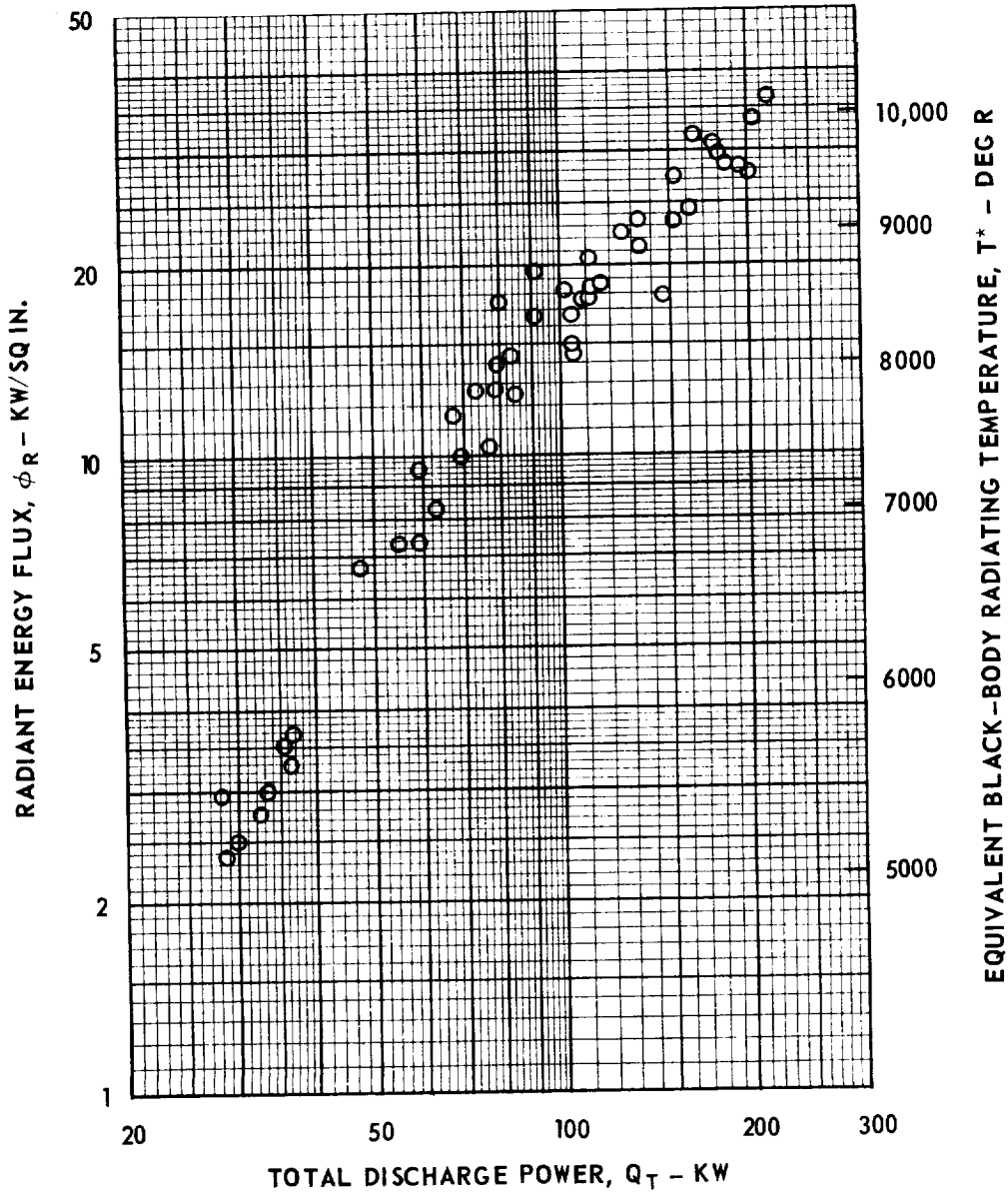
1.2-MEGW R-F INDUCTION HEATER
RANGE OF CHAMBER PRESSURE, $P_D = 2$ TO 16 ATM
RANGE OF ARGON WEIGHT FLOW, $W_A = 0.010$ TO 0.041 LB/SEC
SEE FIG. 10 FOR DETAILS OF TEST CONFIGURATION
REFER TO TABLE III FOR DATA ABOVE $Q_T = 100$ KW



VARIATION OF RADIANT ENERGY FLUX WITH TOTAL DISCHARGE POWER

1.2-MEGW R-F INDUCTION HEATER
 RANGE OF CHAMBER PRESSURE, $P_D = 2$ TO 16 ATM
 RANGE OF ARGON WEIGHT FLOW, $W_A = 0.010$ TO 0.041 LB/SEC
 SEE FIG. 10 FOR DETAILS OF TEST CONFIGURATION
 REFER TO TABLE III FOR DATA ABOVE $Q_T = 100$ KW

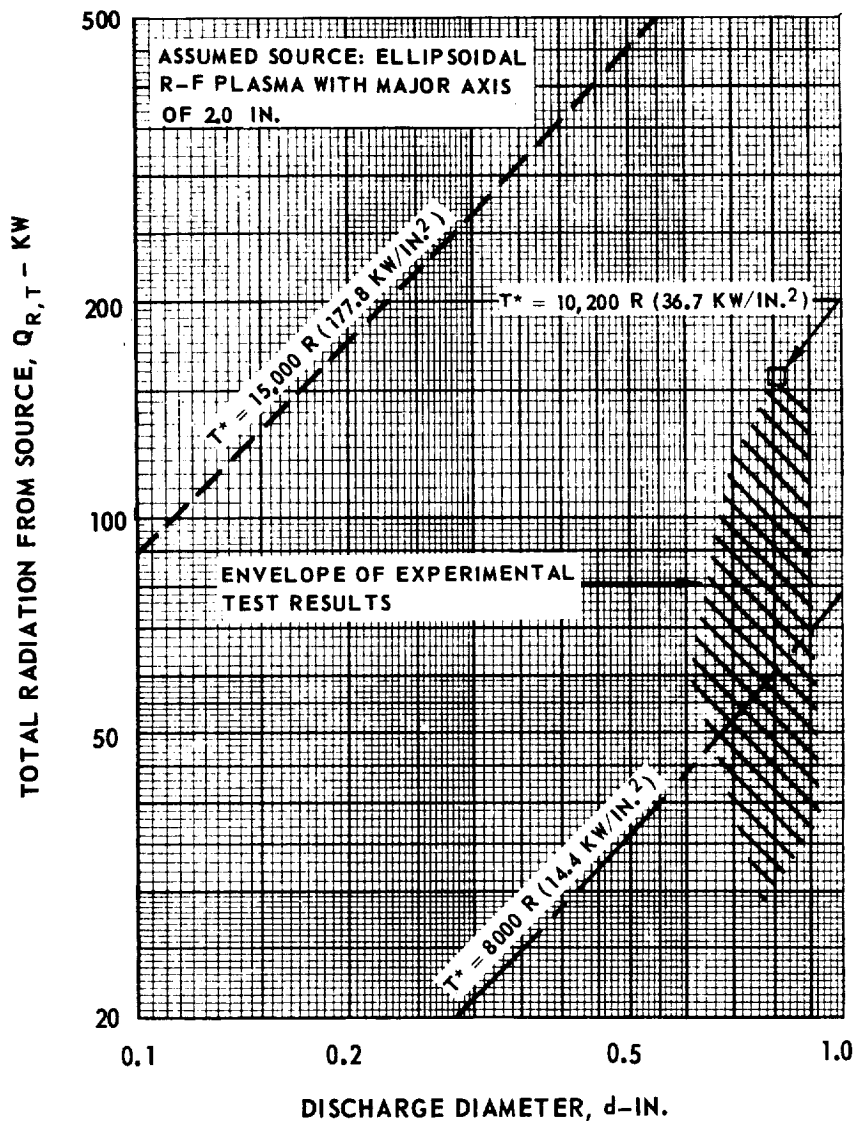
$$\phi_R = Q_{R,T} / A_S$$



COMPARISON OF EXPERIMENTAL RESULTS FROM 1.2-MEGW R-F INDUCTION HEATER WITH RADIATION FLUX LEVELS DESIRED FOR SIMULATION OF THE THERMAL RADIATION FROM A NUCLEAR LIGHT BULB ENGINE

SEE FIG. 10 FOR DETAILS OF TEST CONFIGURATION
REFER TO TABLE III FOR DATA ABOVE $Q_T = 100$ KW

- — — DESIGN FLUX FOR REFERENCE ENGINE
- MAXIMUM RADIATION FLUX LEVEL ACHIEVED TO DATE
- - - - DESIGN FLUX FOR DERATED REFERENCE ENGINE

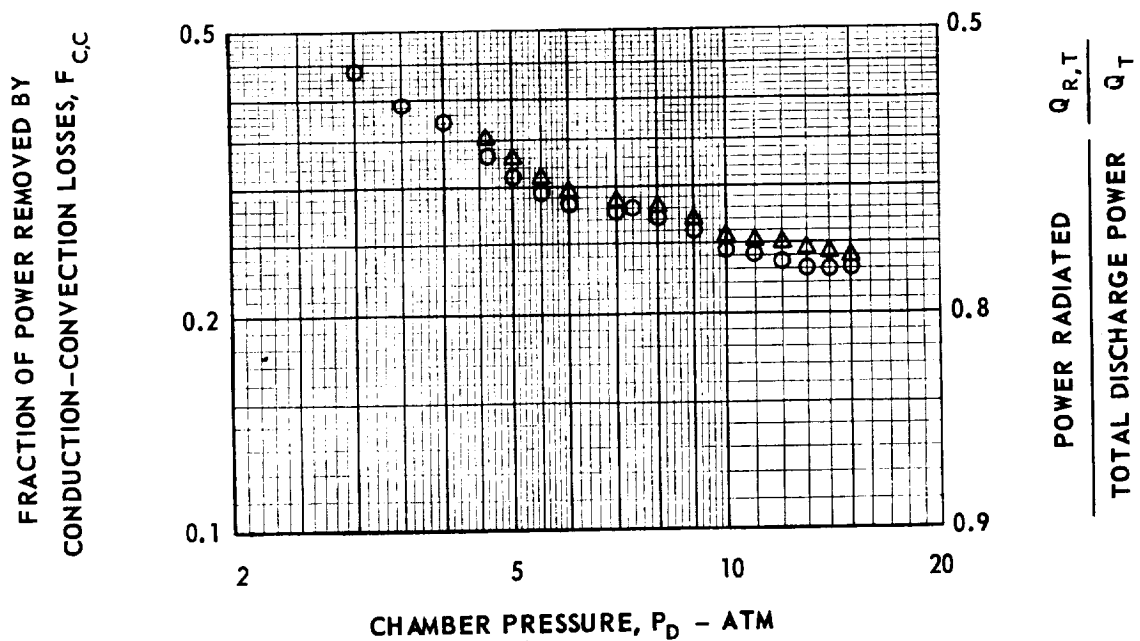


EFFECT OF CHAMBER PRESSURE ON FRACTION OF POWER REMOVED BY CONDUCTION AND CONVECTION LOSSES

SEE FIG.10 FOR DETAILS OF TEST CONFIGURATION
 RANGE OF TOTAL DISCHARGE POWER, $Q_T = 50$ TO 116 KW

$$F_{CC} \approx 1 - \left[\frac{Q_{R,T}}{Q_T} \right]$$

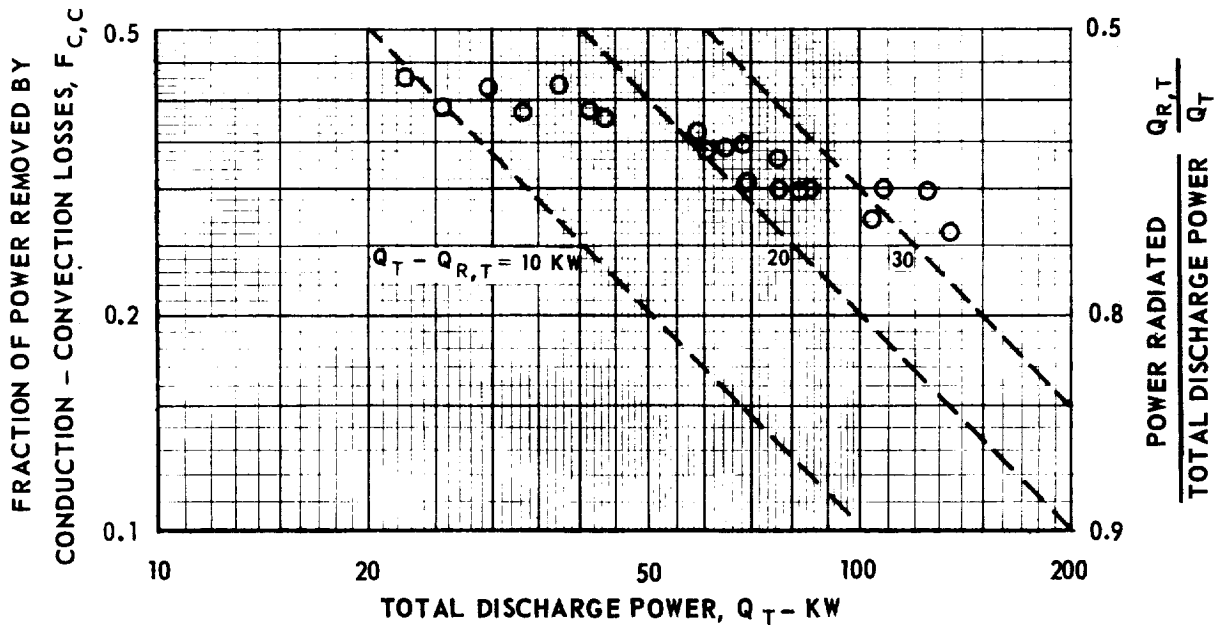
SYMBOL	ARGON WEIGHT FLOW, W_A - LB/SEC
Δ	0.012
\circ	0.015



EFFECT OF TOTAL DISCHARGE POWER ON FRACTION OF POWER REMOVED BY CONDUCTION AND CONVECTION LOSSES



SEE FIG. 10 FOR DETAILS OF TEST CONFIGURATION
 RANGE OF DISCHARGE PRESSURE, $P_D = 5$ TO 6 ATM
 RANGE OF ARGON WEIGHT FLOW, $W_A = 0.010$ TO 0.028 LB/SEC

$$F_{C,C} = 1 - \left[\frac{Q_{R,T}}{Q_T} \right]$$

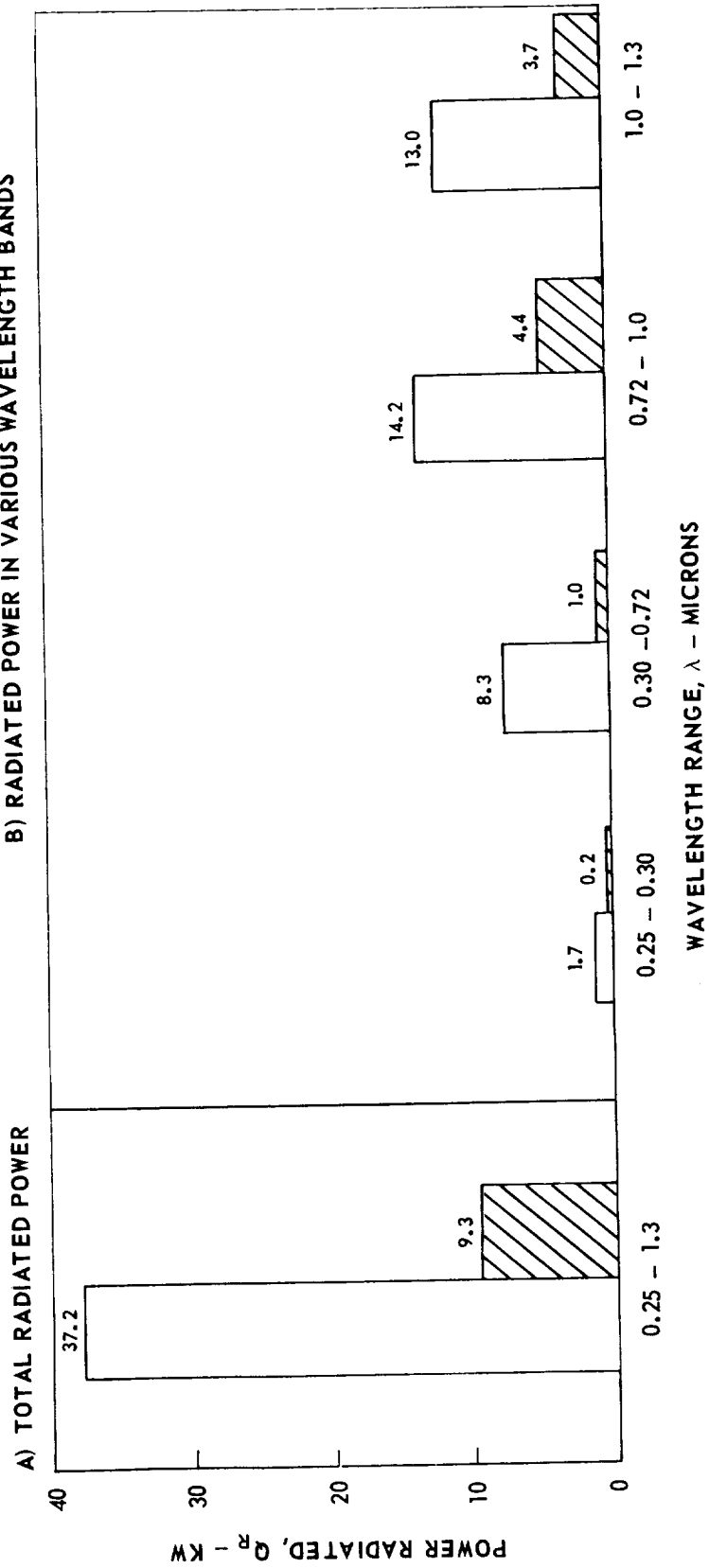


POWER RADIATED THROUGH PERIPHERAL-WALL COOLANT IN VARIOUS WAVELENGTH BANDS WITH AND WITHOUT DYE ADDED

1.2-MEGW R-F INDUCTION HEATER
 RADIATION PASSES THROUGH TWO FUSED SILICA TUBES AND COOLANT
 REFER TO FIG.10 FOR TEST CONFIGURATION
 $Q_T = 80 \text{ KW}$ $P = 4 \text{ ATM}$ $W_A = 0.018 \text{ LB/SEC}$

 WATER-COOLED TRANSPARENT WALL
 WATER-COOLED TRANSPARENT WALL WITH 800 PPM NIGROSINE DYE ADDED

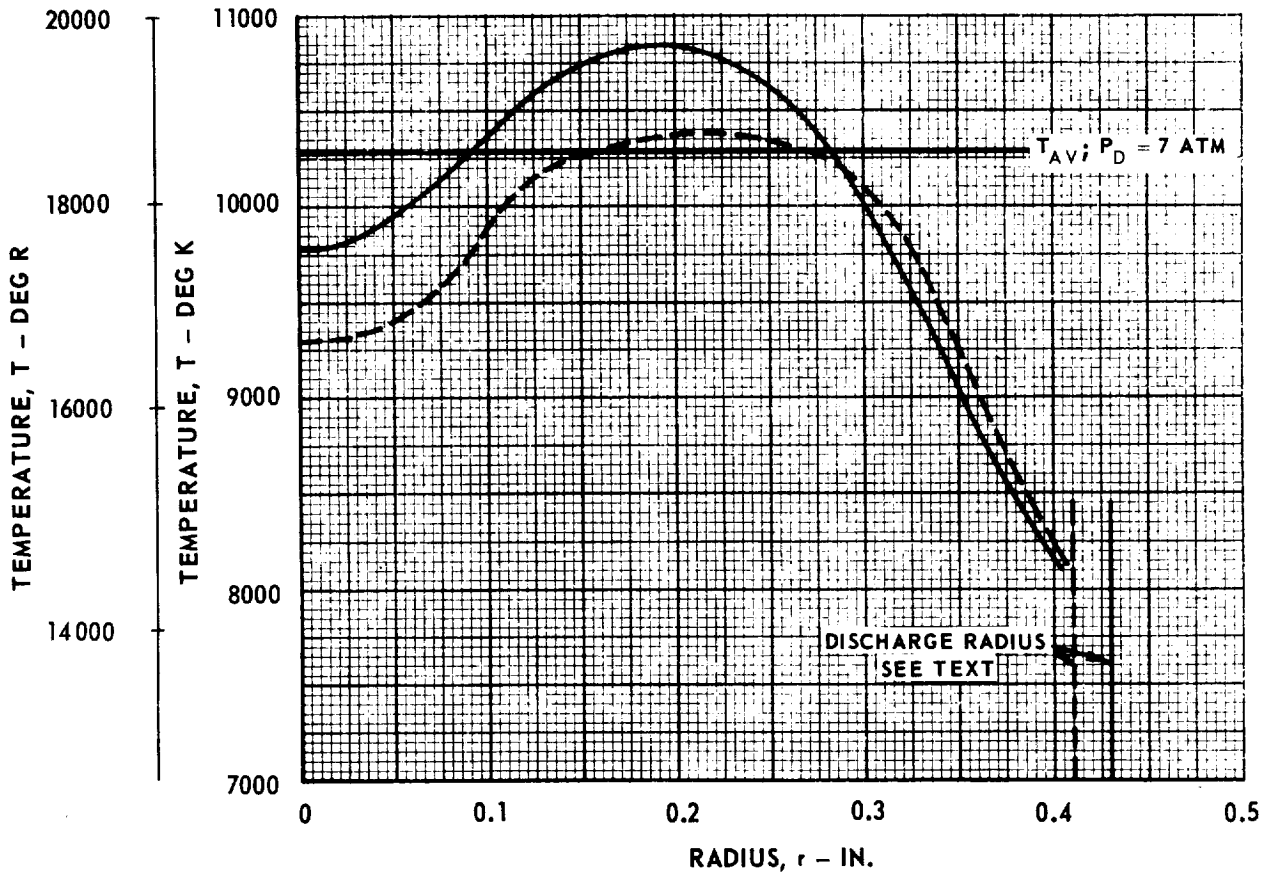
B) RADIATED POWER IN VARIOUS WAVELENGTH BANDS



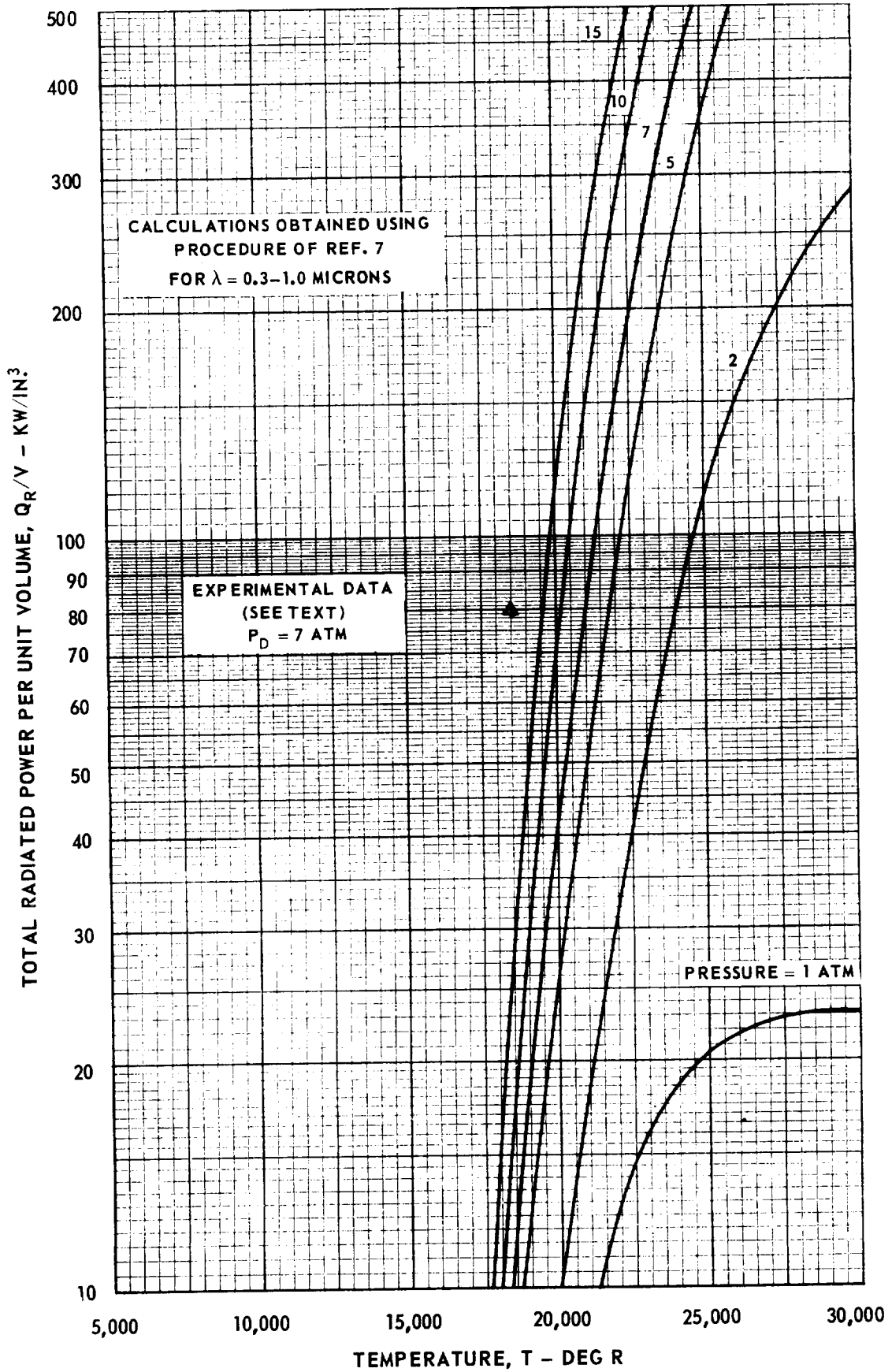
TYPICAL RADIAL DISTRIBUTIONS OF TEMPERATURE OBTAINED IN ARGON R-F PLASMA TESTS

1.2-MEGW R-F INDUCTION HEATER
TEMPERATURE PROFILE DETERMINED FROM INTENSITY OF ARGON 4158.59 Å LINE
SEE FIG. 10 FOR SKETCH OF CONFIGURATION USED
SEE FIG. 6 FOR SCHEMATIC OF OPTICAL SYSTEM USED

- $P_D = 7 \text{ ATM}, Q_T = 120 \text{ KW}, Q_{R,T} = 66 \text{ KW}, Q_{R,T}/V = 82 \text{ KW/IN}^3, T_{AV} = 18,550 \text{ R}$
- - - $P_D = 4 \text{ ATM}, Q_T = 60 \text{ KW}, Q_{R,T} = 35.5 \text{ KW}$

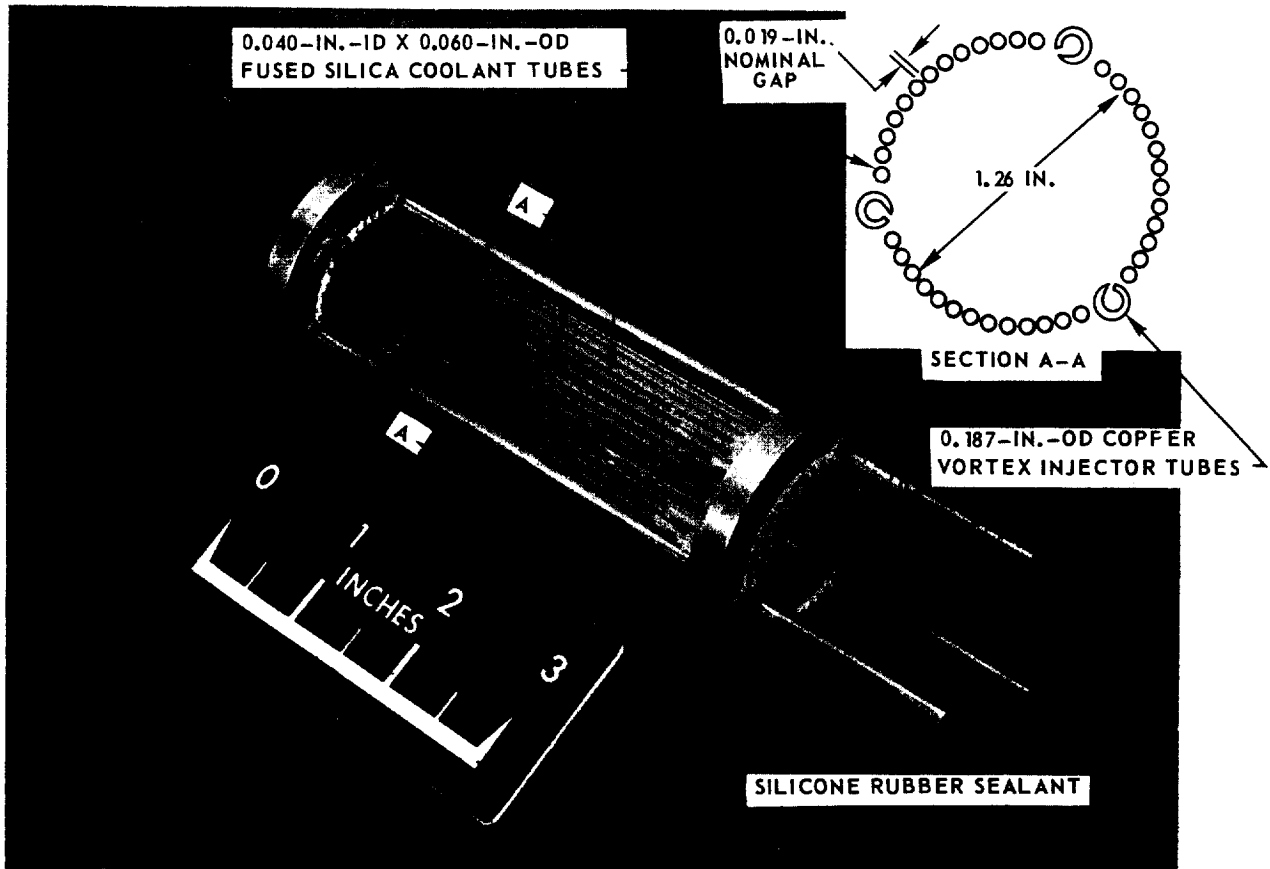


CALCULATED VARIATION OF RADIATED POWER PER UNIT VOLUME WITH TEMPERATURE FOR AN ARGON PLASMA

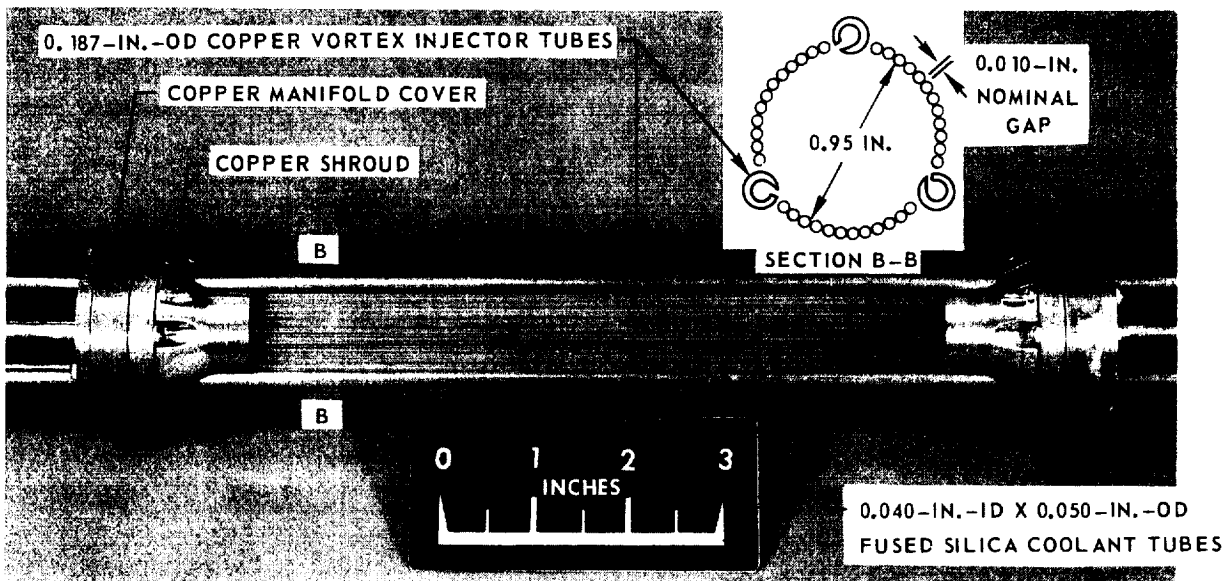


PHOTOGRAPHS OF TRANSPARENT-WALL AXIAL COOLANT-TUBE MODELS EMPLOYED IN R-F PLASMA TESTS

a) DETAILS OF 1.26-IN.-ID MODEL

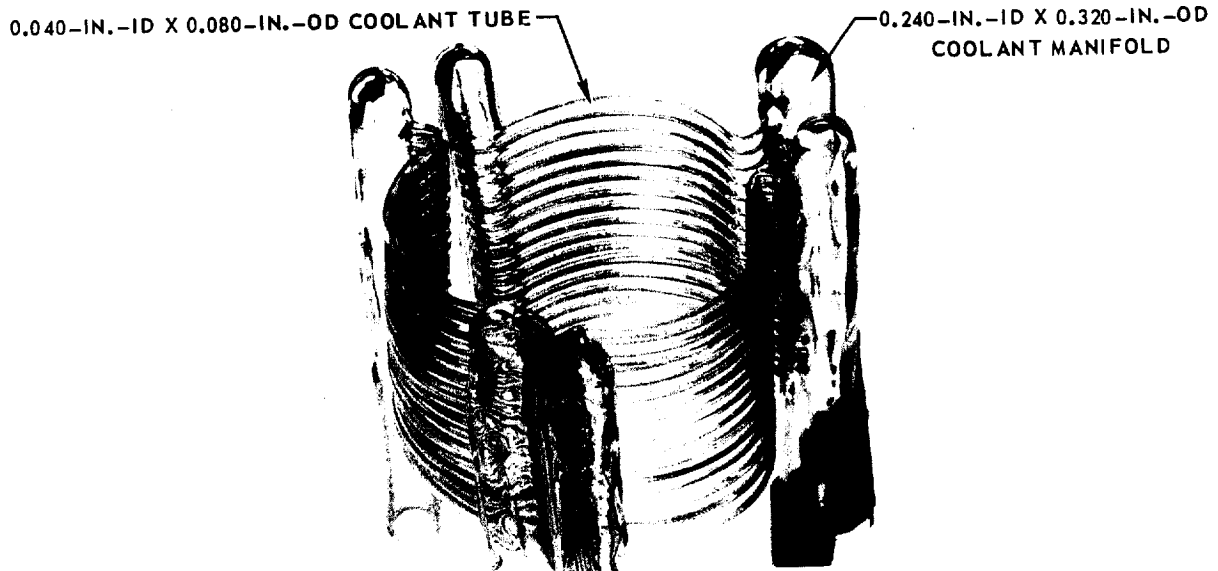


b) DETAILS OF 0.95-IN.-ID MODEL

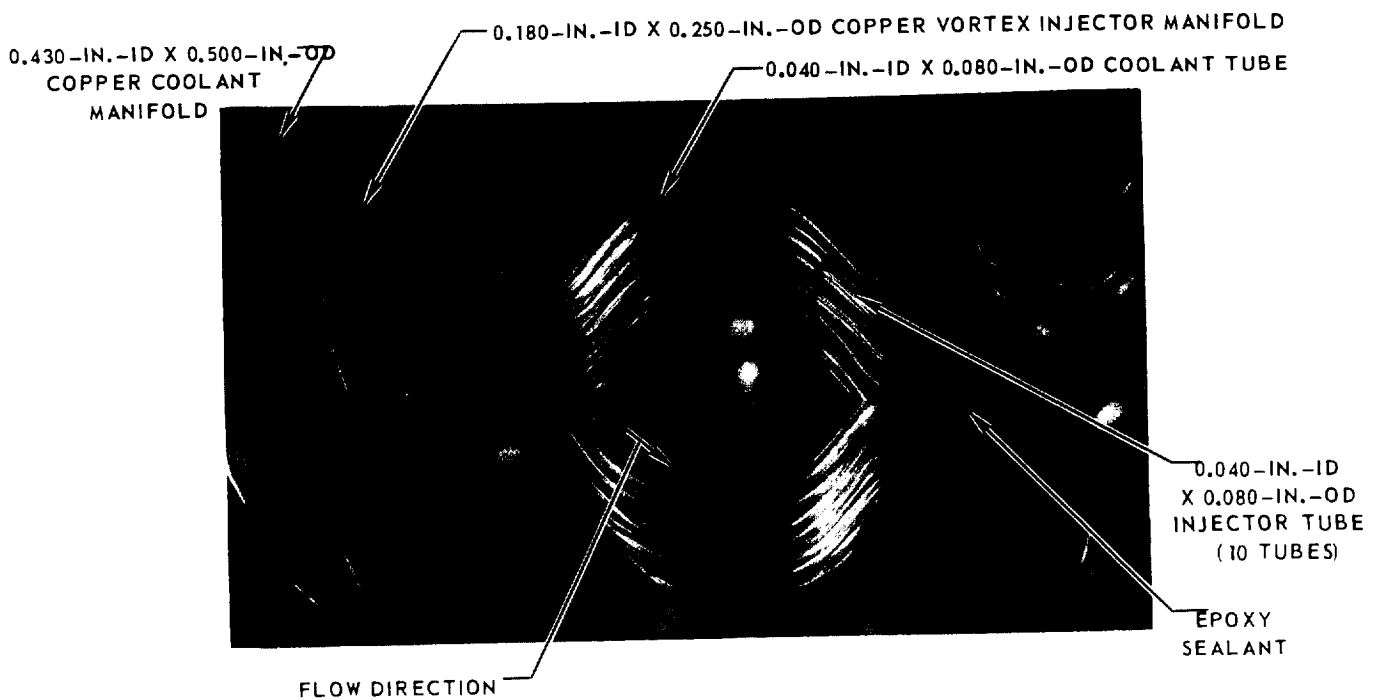


PHOTOGRAPHS OF TRANSPARENT-WALL CIRCUMFERENTIAL-COOLANT-TUBE MODEL COMPONENTS

a) CONFIGURATION WITH FUSED SILICA COOLANT TUBES AND FUSED SILICA COOLANT MANIFOLDS



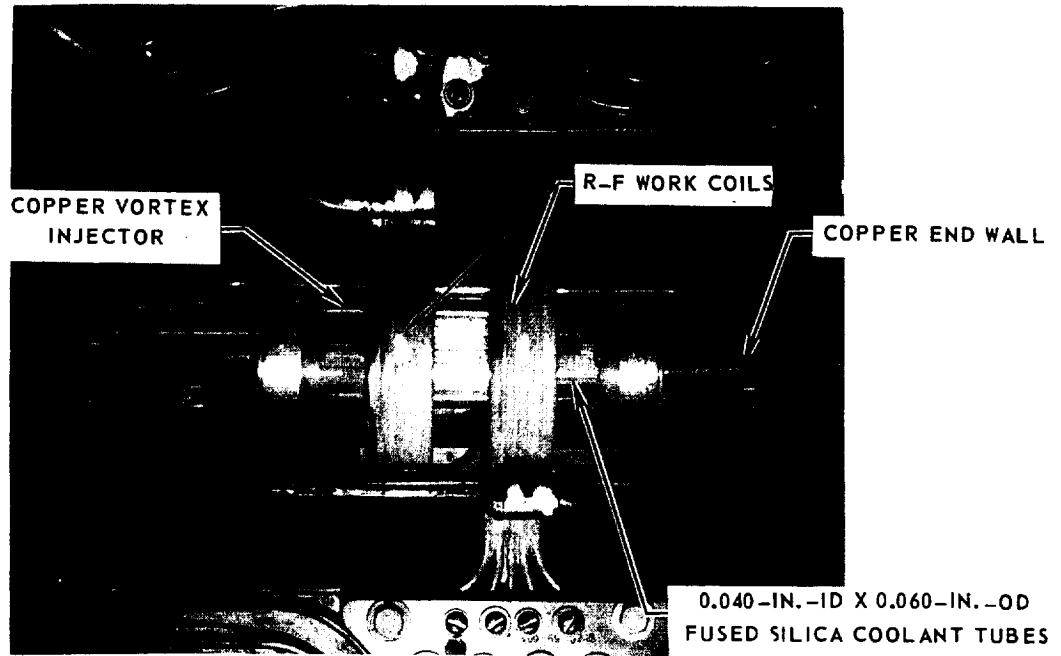
b) CONFIGURATION WITH FUSED SILICA COOLANT TUBES AND COPPER COOLANT MANIFOLD



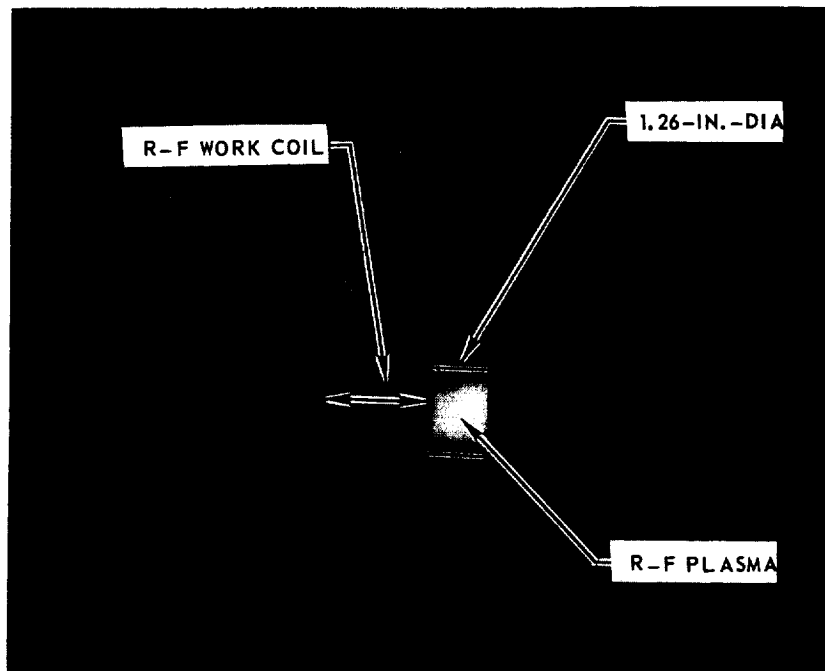
PHOTOGRAPHS OF 1.26-IN.-ID AXIAL-COOLANT-TUBE MODEL EMPLOYED IN R-F PLASMA TESTS

SEE TABLE IV FOR SUMMARY OF TEST RESULTS
REFER TO FIG. 22a FOR MODEL DETAILS

a) PHOTOGRAPH OF MODEL INSTALLED IN 1.2-MEGW R-F INDUCTION HEATER



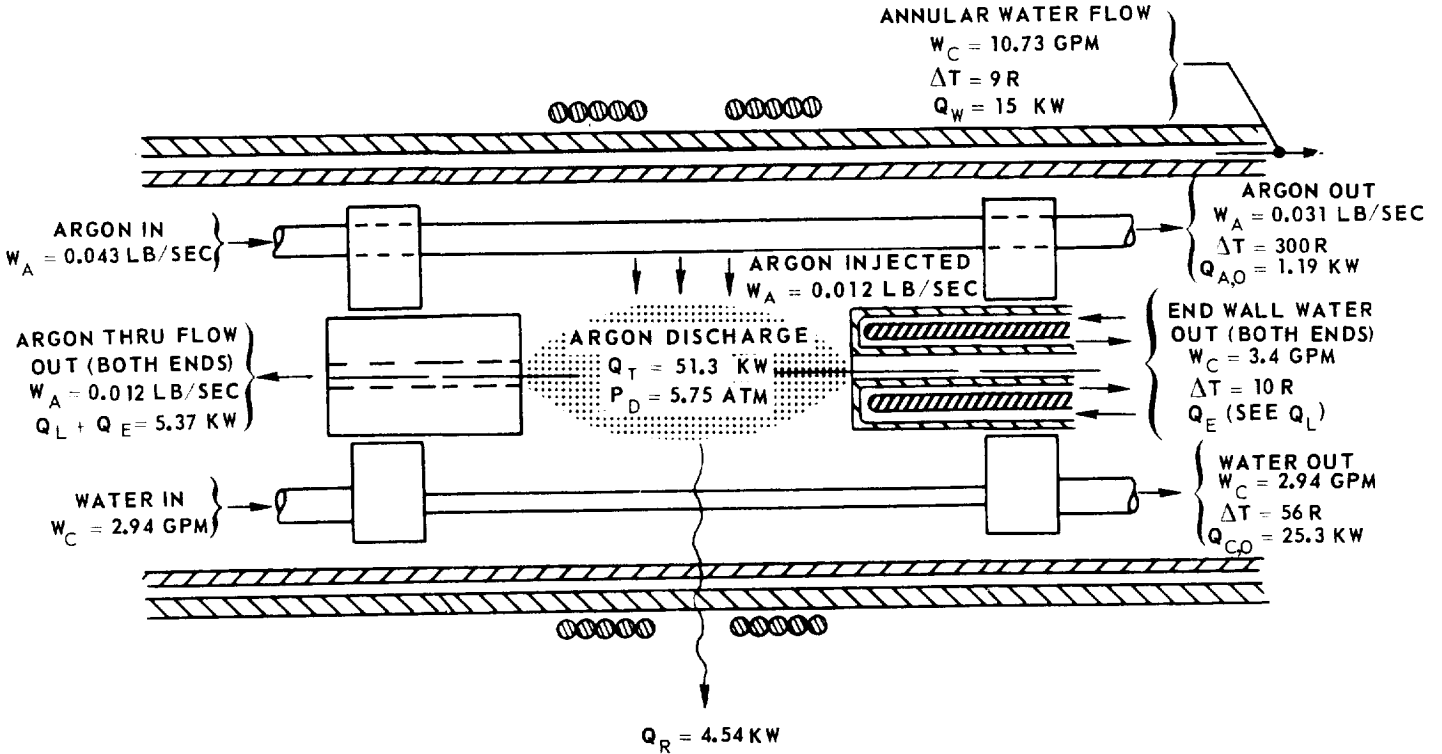
b) PHOTOGRAPH OF R-F PLASMA



SKETCH OF TYPICAL POWER LOSSES FOR 1.26-IN.-ID AXIAL COOLANT-TUBE MODEL

TESTED IN 1.2-MEGW R-F INDUCTION HEATER

REFER TO FIG. 22a FOR DETAILS OF MODEL



TOTAL POWER RADIATED/TOTAL DISCHARGE POWER, $Q_{R,T} / Q_T$:

$$\frac{Q_{R,T}}{Q_T} = \frac{Q_R + Q_W}{Q_T} = \frac{4.54 + 15}{51.3} = 0.381$$

WHERE:

$$Q_T = Q_{C,O} + Q_{A,O} + Q_R + Q_W + (Q_L + Q_E)$$

$$= 25.3 + 1.19 + 4.54 + 15 + 5.37$$

$$Q_T = 51.3 \text{ KW}$$

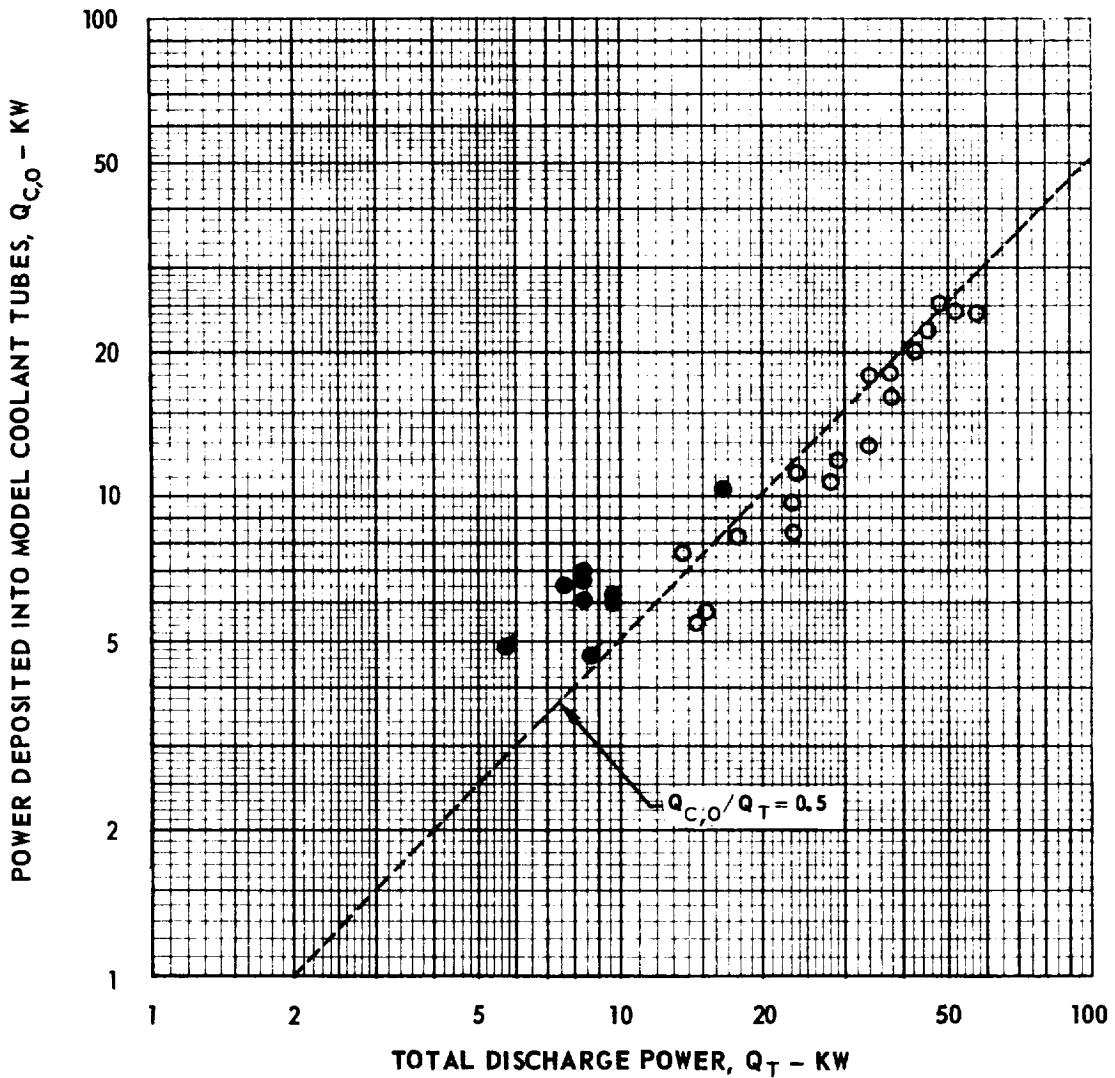
$$Q_{C,O}, Q_W, (Q_L + Q_E) = (0.146)(\text{GPM})(\Delta T)$$

$$Q_{A,O} = (0.1252)(W_A)(\Delta T)$$

$$Q_R = (8.6 \times 10^{-3})(MV)$$

VARIATION OF POWER DEPOSITED INTO AXIAL-COOLANT-TUBES WITH TOTAL DISCHARGE POWER IN TRANSPARENT-WALL MODEL TESTS

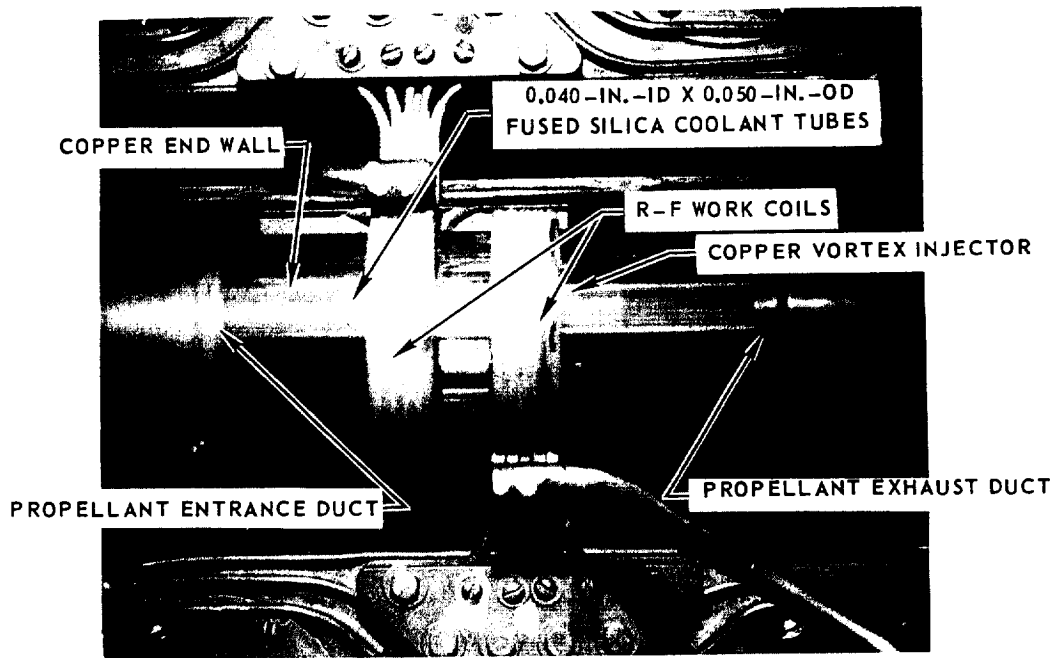
1.2-MEGW R-F INDUCTION HEATER
 RANGE OF CHAMBER PRESSURE, $P_D = 2.2$ TO 9.2 ATM
 RANGE OF ARGON WEIGHT FLOW RATE $W_A = 0.0032$ TO 0.012 LB/SEC
 OPEN SYMBOLS DENOTE TESTS WITH 1.26-IN.-ID AXIAL-COOLANT-TUBE MODEL
 SEE FIG. 22a FOR DETAILS OF MODEL
 SOLID SYMBOLS DENOTE TESTS WITH 0.95-IN.-ID AXIAL-COOLANT-TUBE MODEL
 SEE FIG. 22b FOR DETAILS OF MODEL
 FLAGGED SYMBOLS DENOTE DATA TAKEN BEFORE SEED DEPOSITION ON MODEL



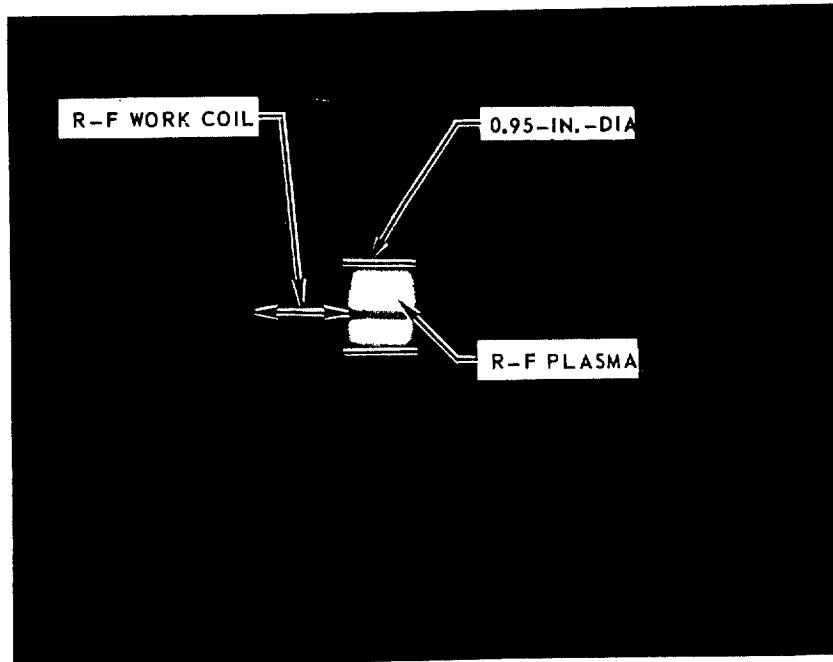
PHOTOGRAPHS OF 0.95-IN.-ID AXIAL COOLANT-TUBE MODEL EMPLOYED IN R-F PLASMA TESTS

SEE TABLE IX FOR SUMMARY OF TEST RESULTS
REFER TO FIG. 22b FOR MODEL DETAILS

a) PHOTOGRAPH OF MODEL INSTALLED IN 1.2-MEGW R-F INDUCTION HEATER

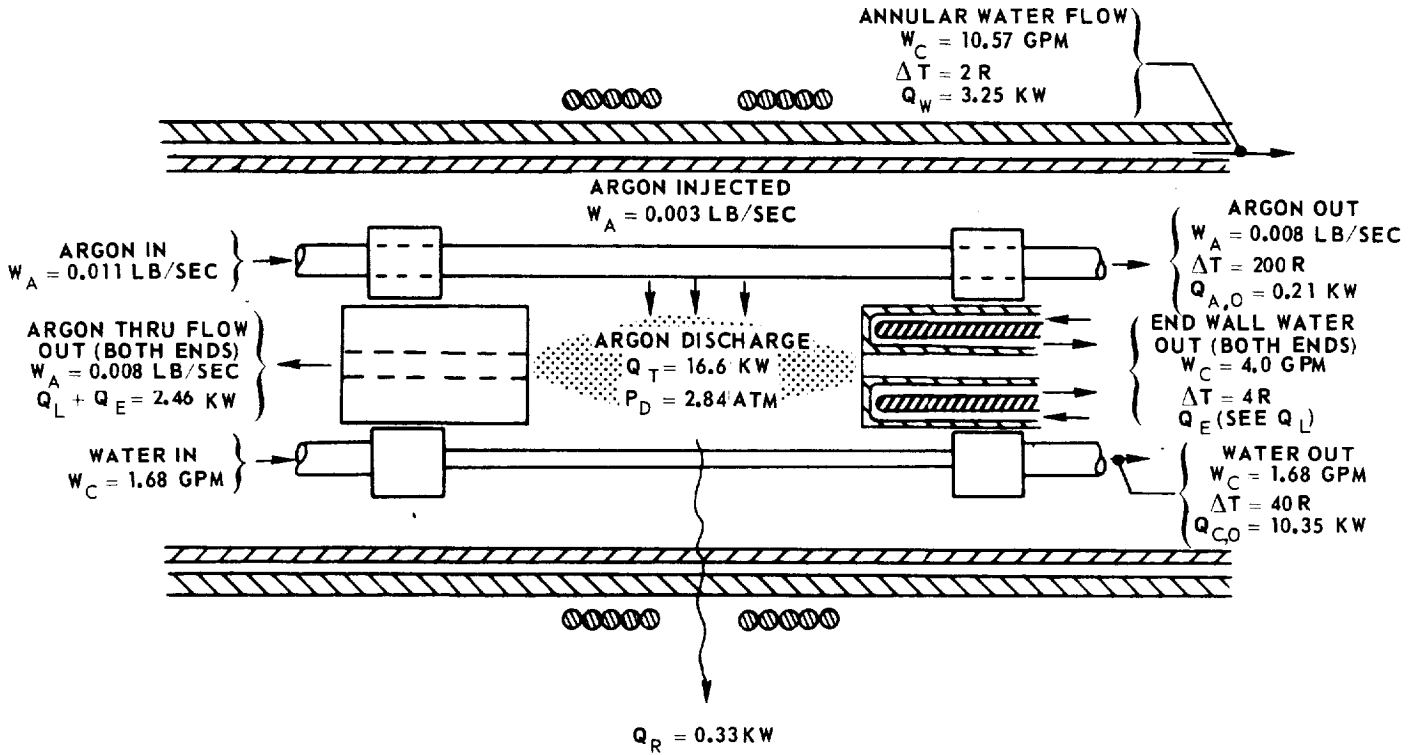


b) PHOTOGRAPH OF R-F PLASMA



SKETCH OF TYPICAL POWER LOSSES FOR 0.95-IN.-ID AXIAL-COOLANT-TUBE MODEL

TESTED IN 1.2-MEGW R-F INDUCTION HEATER
 REFER TO FIG. 22b FOR DETAILS OF MODEL
 DATA TAKEN AFTER SEED DEPOSITION ON MODEL



TOTAL POWER RADIATED/TOTAL DISCHARGE POWER, $Q_{R,T}/Q_T$:

$$\frac{Q_{R,T}}{Q_T} = \frac{Q_R + Q_W}{Q_T} = \frac{0.33 + 3.25}{16.6} = 0.216$$

WHERE:

$$Q_T = Q_{C,O} + Q_{A,O} + Q_R + Q_W + (Q_L + Q_E)$$

$$= 10.35 + 0.21 + 0.33 + 3.25 + 2.46$$

$$Q_T = 16.6 \text{ KW}$$

$$Q_{C,O}, Q_W, (Q_L + Q_E) = (0.146)(\text{GPM})(\Delta T)$$

$$Q_{A,O} = (0.1252)(W_A)(\Delta T)$$

$$Q_R = (8.6 \times 10^{-3})(MV)$$

COMPARISON OF MODEL WALL HEAT DEPOSITION RATES WITH THOSE CALCULATED IN FULL-SCALE ENGINE

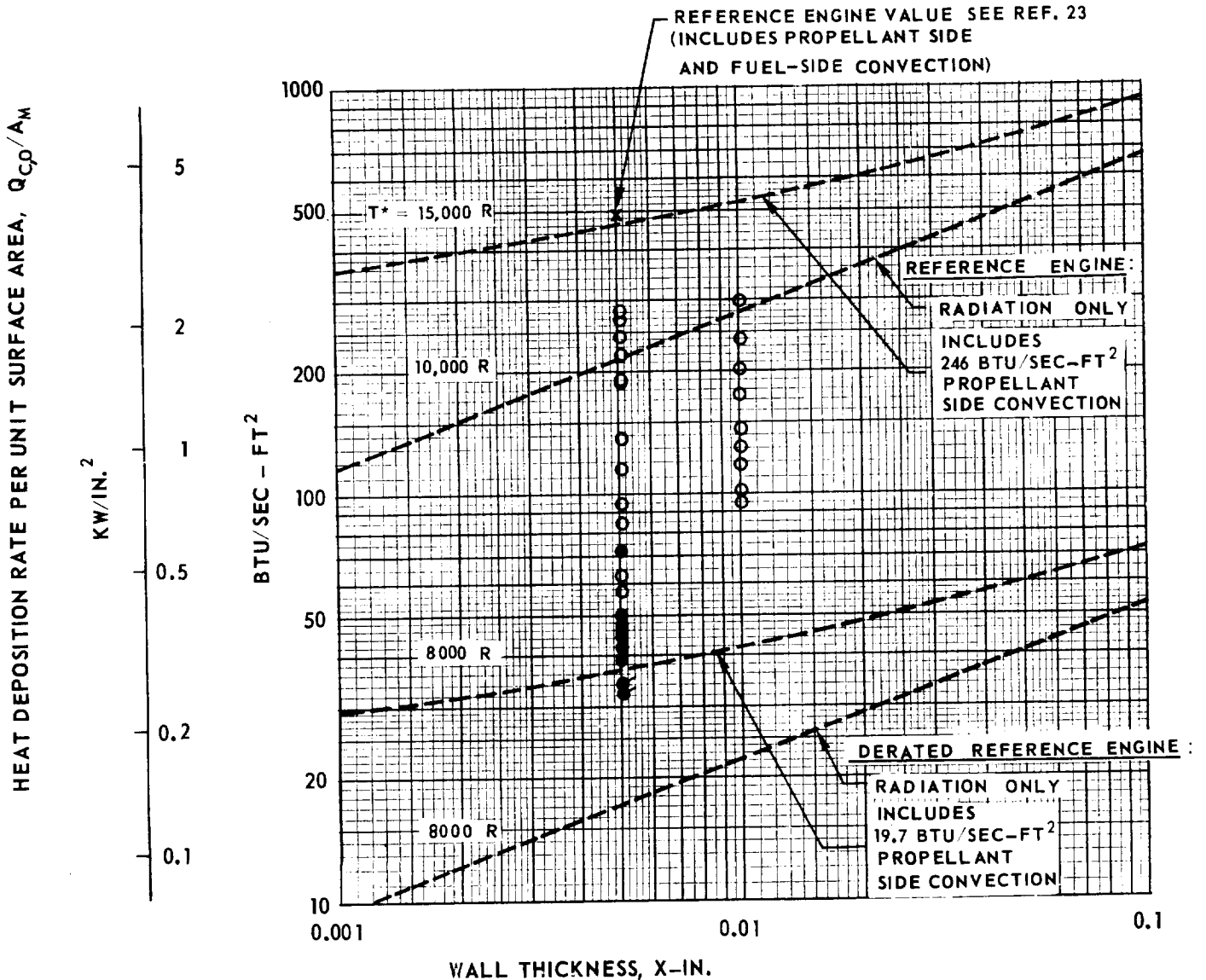
RANGE OF CHAMBER PRESSURE, $P_D = 2.2$ TO 9.2 ATM
 RANGE OF ARGON WEIGHT FLOW, $W_A = 0.0032$ TO 0.012 LB/SEC

DASHED LINES DENOTE FULL-SCALE ENGINE VALUES (REF. 24)

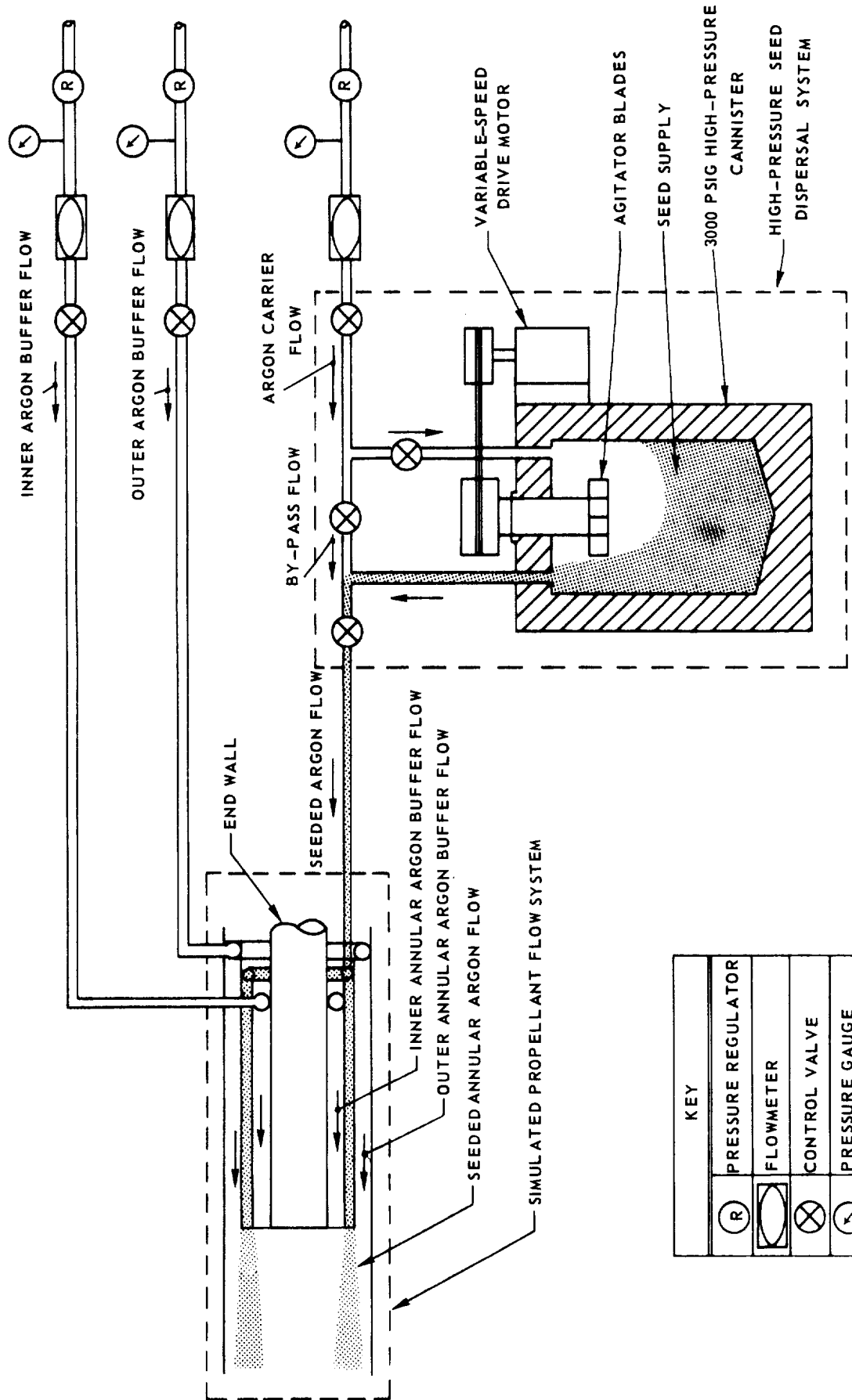
OPEN SYMBOLS DENOTE TESTS WITH 1.26-IN.-ID AXIAL COOLANT-TUBE MODEL
 REFER TO FIG. 22a AND TABLE IV FOR DETAILS OF CONFIGURATION
 $A_M = 0.0885$ IN.² (ONE-HALF TOTAL TUBE SURFACE AREA) - SEE TEXT

SOLID SYMBOLS DENOTE TESTS WITH 0.95-IN.-ID AXIAL COOLANT-TUBE MODEL
 REFER TO FIG. 22b ALSO TABLE IV FOR DETAILS OF CONFIGURATION
 $A_M = 0.137$ IN.² (TOTAL TUBE SURFACE AREA) - SEE TEXT

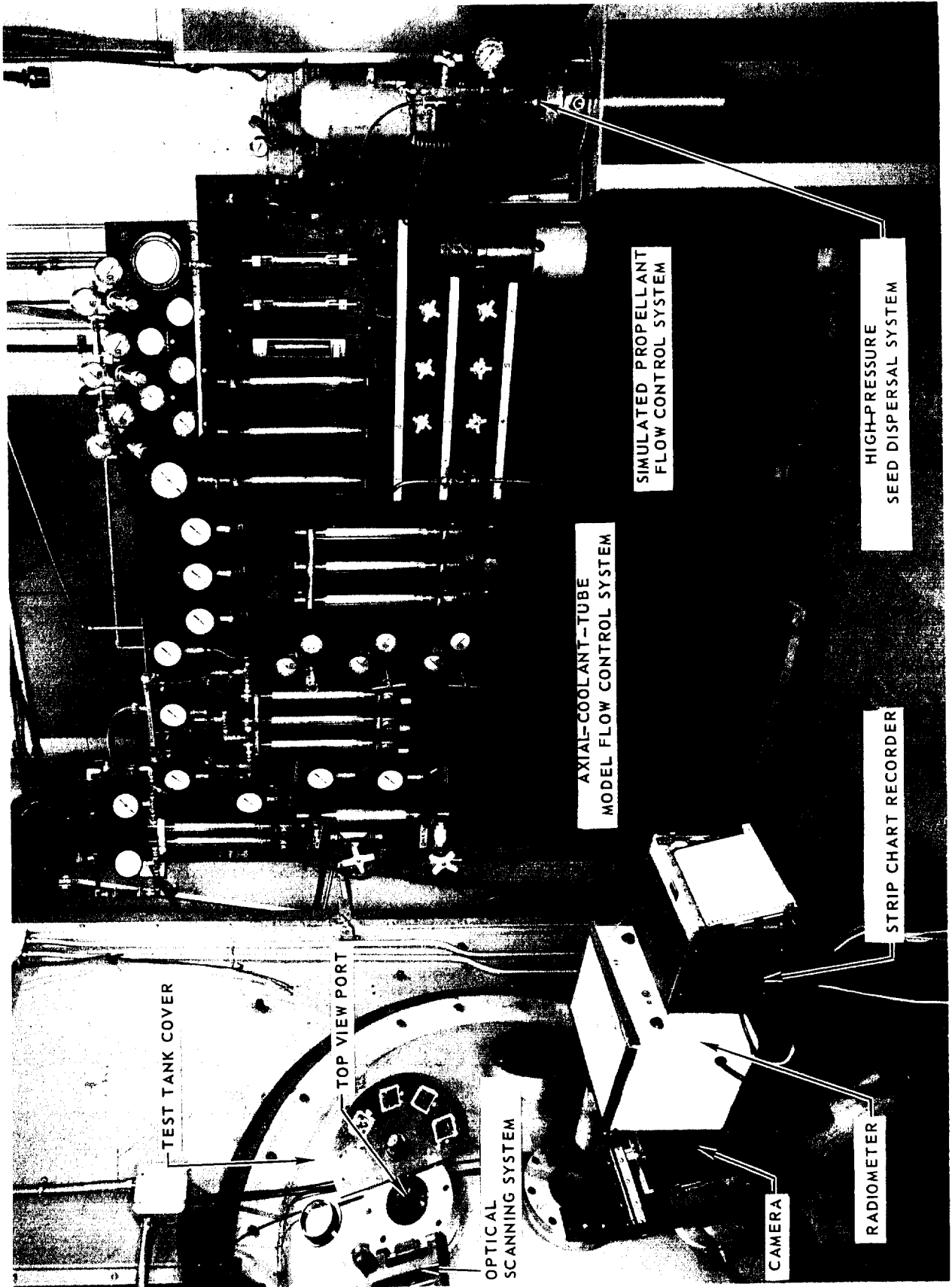
FLAGGED SOLID SYMBOLS DENOTE DATA TAKEN BEFORE SEED DEPOSITION ON MODEL



**SCHEMATIC DIAGRAM OF SIMULATED PROPELLANT FLOW SYSTEM
AND HIGH-PRESSURE SEED DISPERSAL SYSTEM**

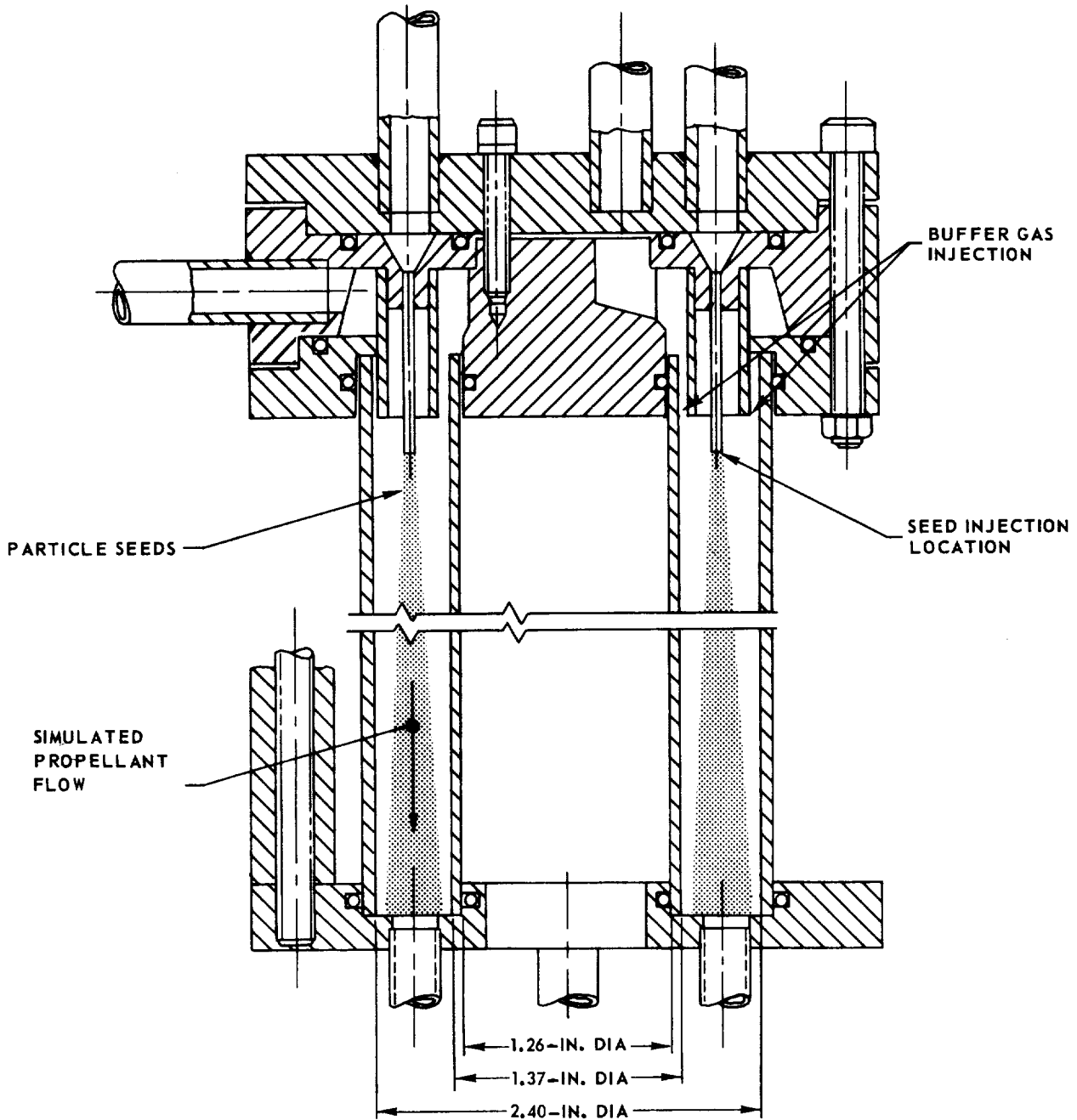


PHOTOGRAPH OF FLOW CONTROL SYSTEMS AND HIGH-PRESSURE SEED DISPERSAL SYSTEM AS USED IN 1.2-MEGW R-F INDUCTION HEATER TESTS



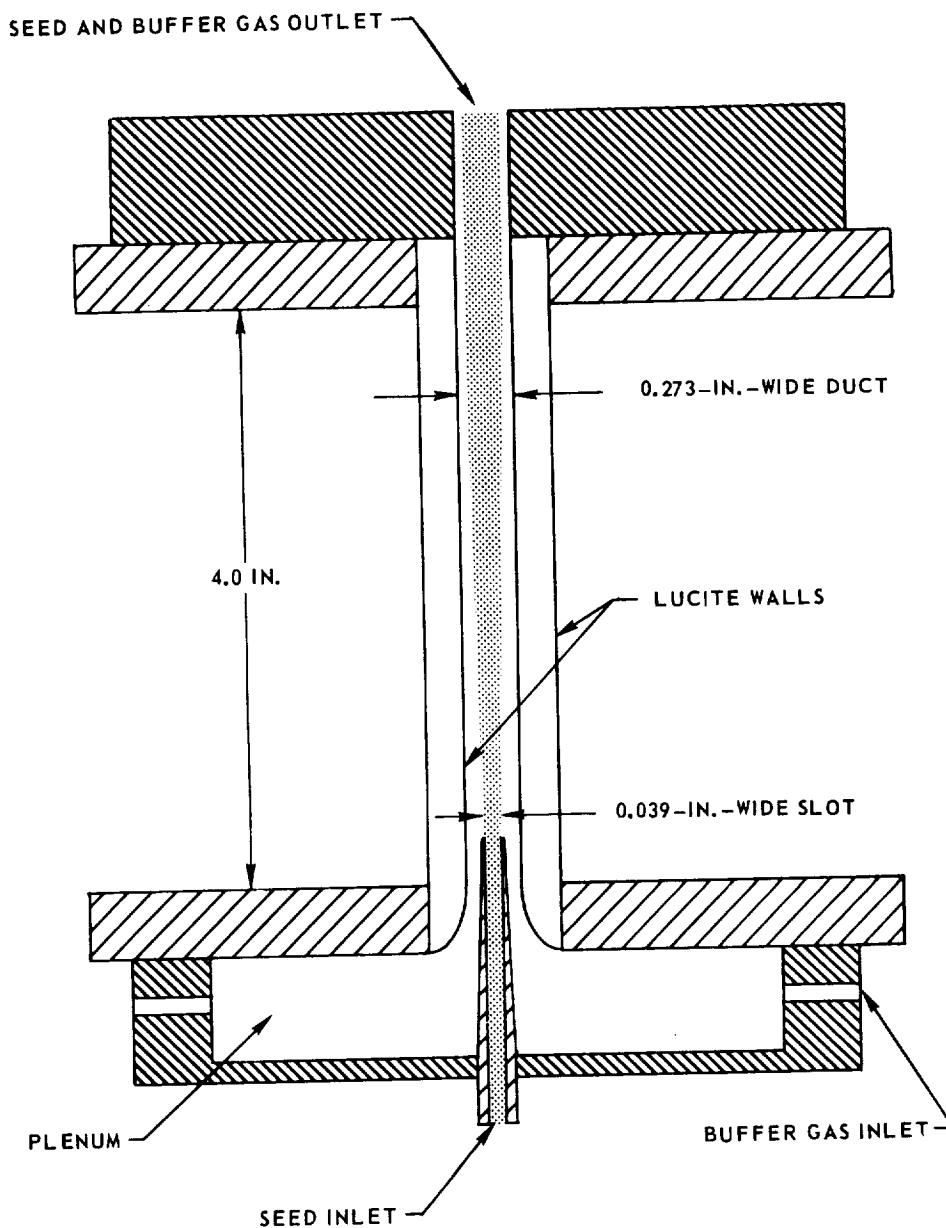
SCHEMATIC OF INITIAL CONFIGURATION FOR SIMULATED PROPELLANT FLOW EXPERIMENTS

USED IN COLD FLOW TESTS ONLY
CONFIGURATION SHOWN FULL SIZE

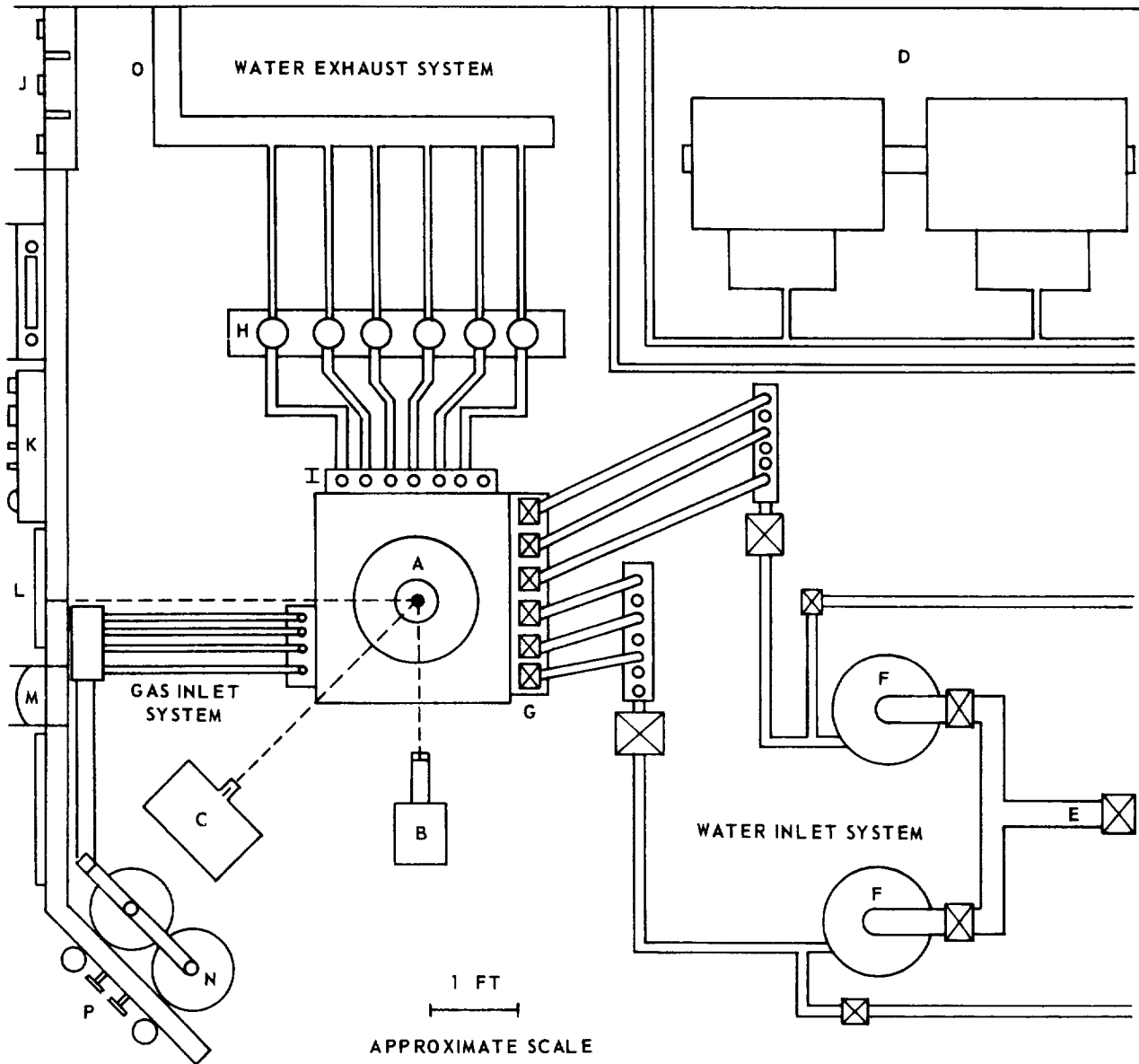


SKETCH OF TWO DIMENSIONAL PROPELLANT FLOW SIMULATOR

USED IN COLD FLOW TESTS ONLY
FLOW PASSAGE DIMENSIONS = 4.0 IN. BY 3.0 IN.



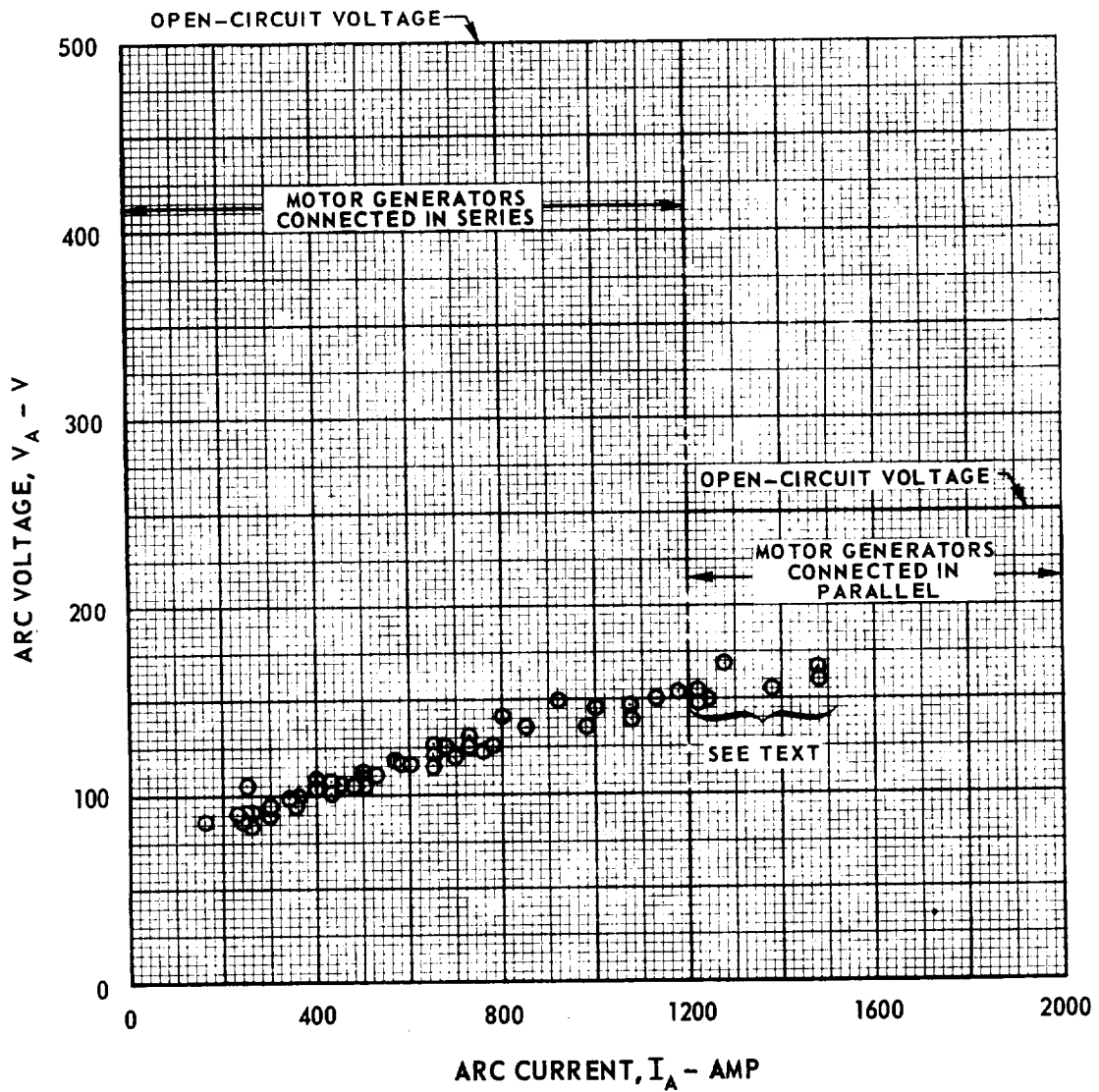
SCHMATIC OF D-C ARC HEATER FACILITY



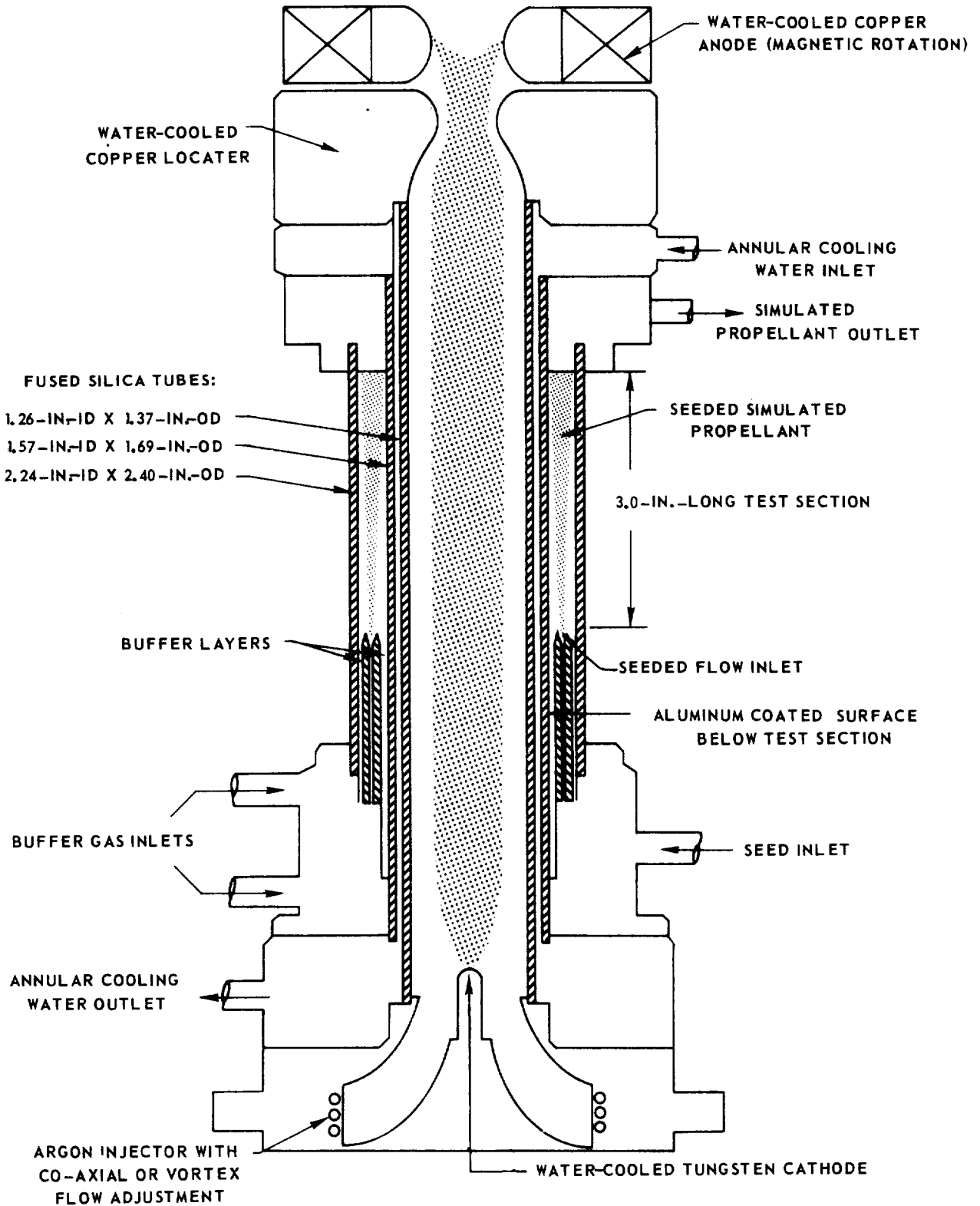
- | | | |
|------------------------------|----------------------------|---|
| A) D-C ARC | G) CONTROL VALVES | M) OSCILLOSCOPE |
| B) CAMERA | H) FLOWMETERS | N) ARGON SUPPLY |
| C) RADIOMETER | I) THERMOCOUPLES | O) COOLING WATER DRAIN |
| D) MOTOR-GENERATOR SETS | J) BALLAST RESISTOR | P) CONTROL PANEL FOR PROPELLANT HEATING TESTS |
| E) MAIN WATER SUPPLY LINE | K) ARC CONTROL CONSOLE | |
| F) HIGH-PRESSURE WATER PUMPS | L) SHIELDED VIEWING WINDOW | |

ELECTRICAL OPERATING CHARACTERISTICS OF D-C ARC HEATER

1.0 ATM PRESSURE ARGON ARC



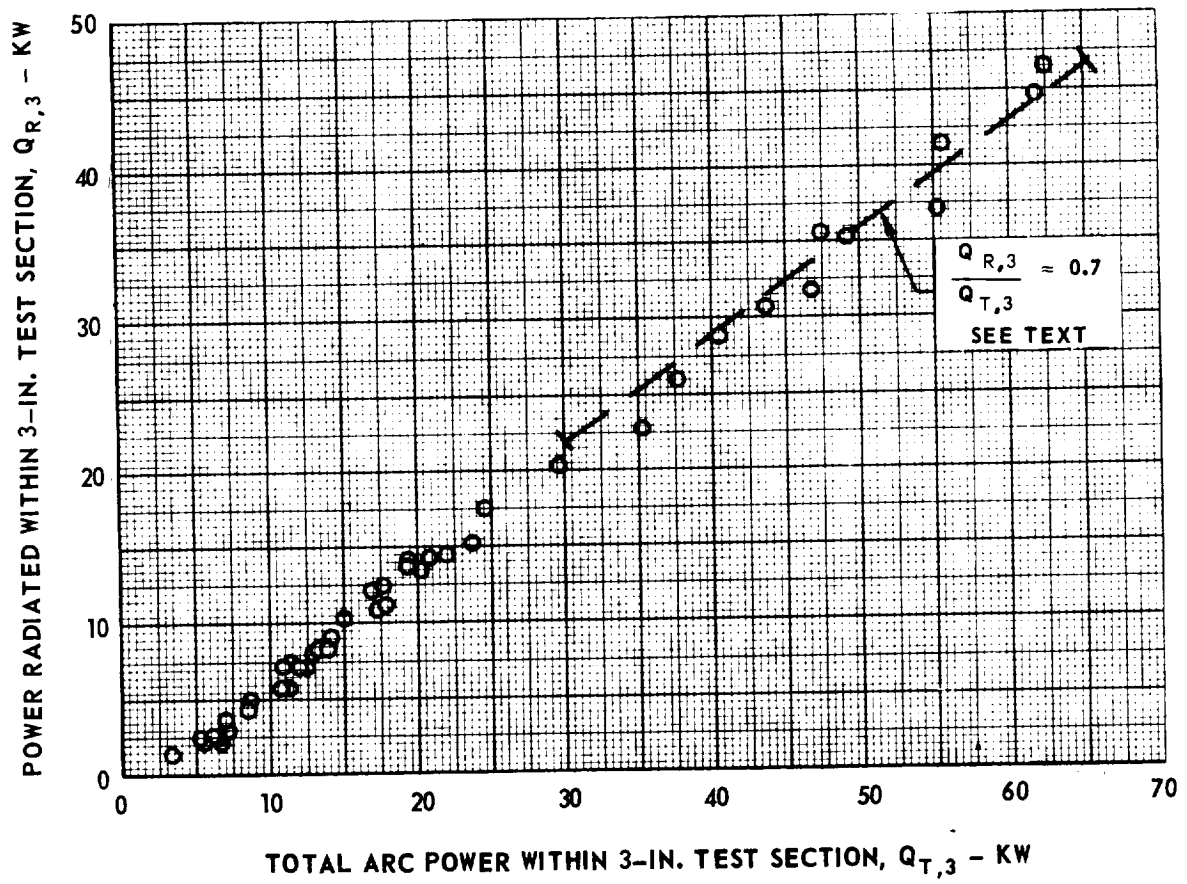
SKETCH OF BASIC D-C ARC HEATER CONFIGURATION SHOWN WITH SURROUNDING SIMULATED PROPELLANT HEATING DUCT



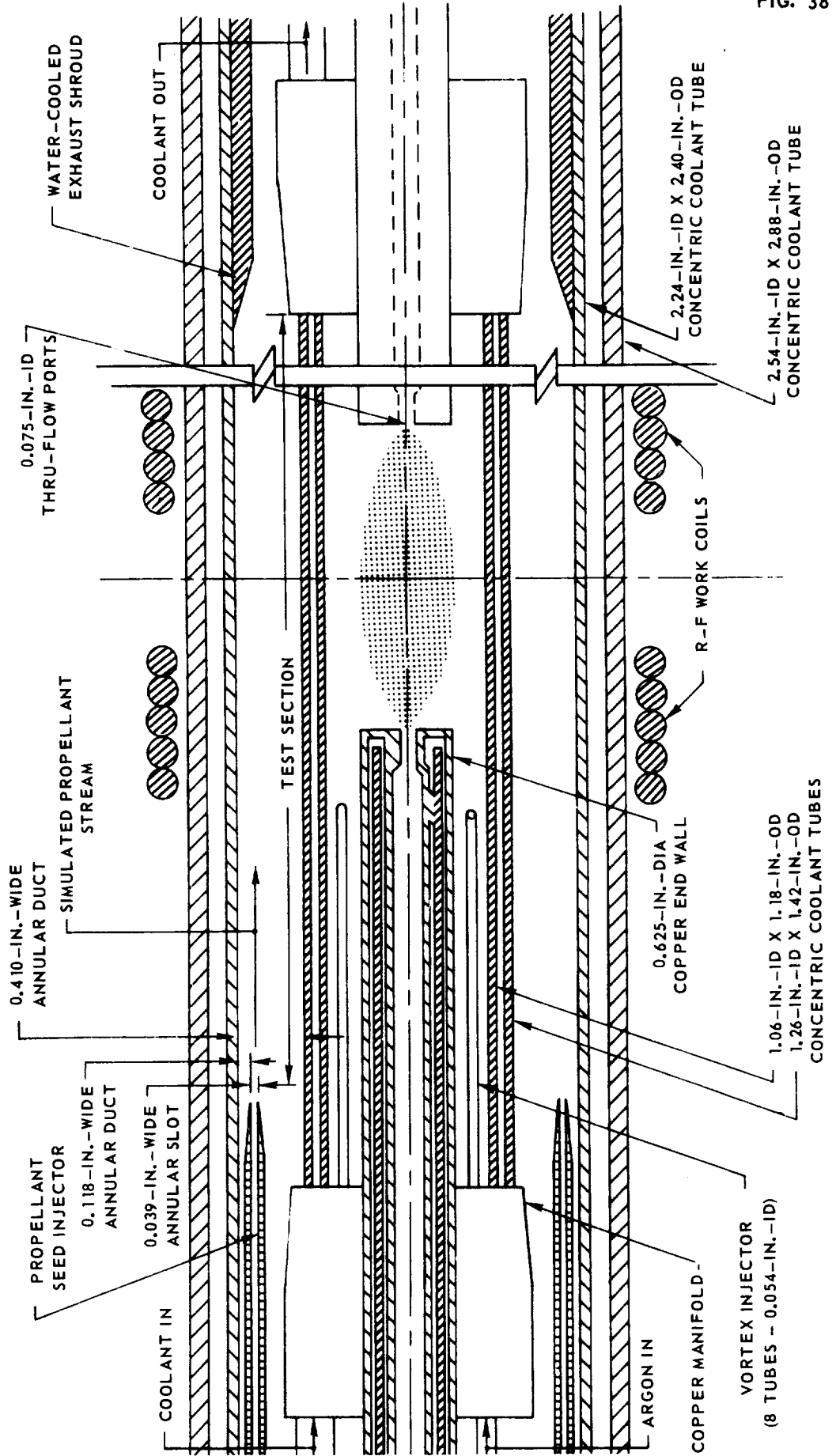
RADIATION CHARACTERISTICS OF D-C ARC HEATER USED IN SIMULATED PROPELLANT HEATING TESTS

SEE FIG.36 FOR SKETCH OF BASIC D-C ARC HEATER CONFIGURATION

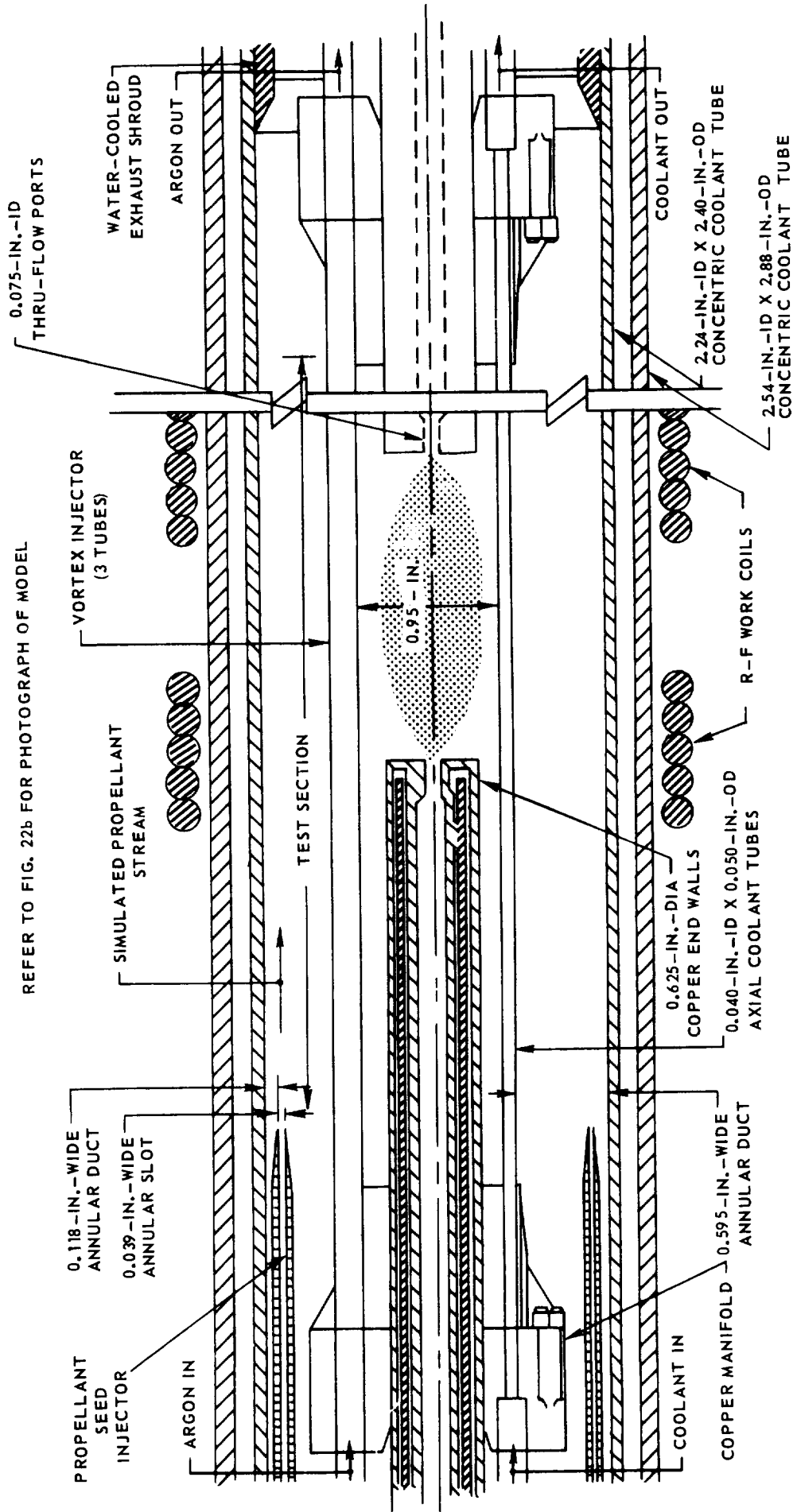
NOTE: PROPELLANT FLOW DUCTING AND ASSOCIATED WATER COOLING WAS REMOVED DURING THESE TESTS



SKETCH OF PROPELLANT HEATING DUCT CONFIGURATION WITH 1.06-IN.-ID CONCENTRIC COOLANT-TUBE MODEL FOR TESTS IN 1.2-MEGW R-F INDUCTION HEATER



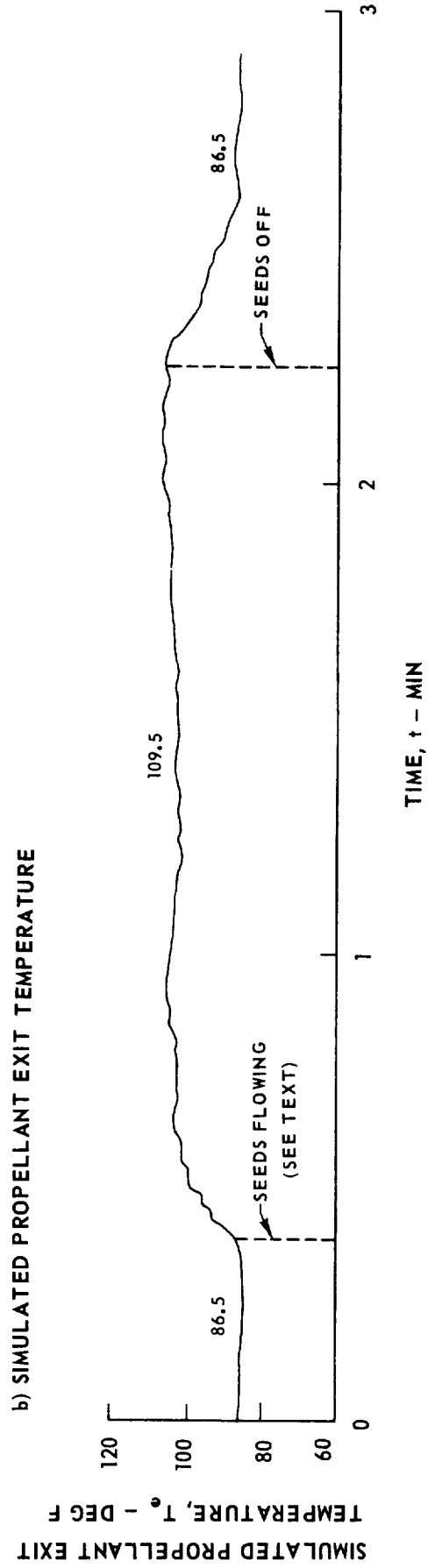
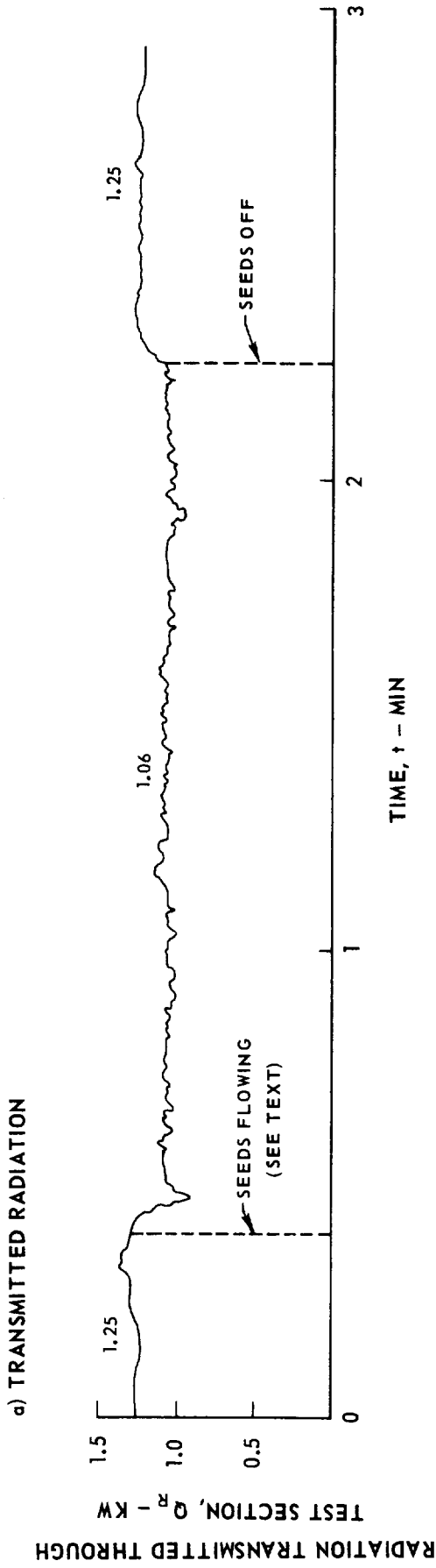
SKETCH OF PROPELLANT HEATING DUCT CONFIGURATION WITH 0.95-IN.-ID AXIAL-COOLANT-TUBE MODEL FOR TESTS IN 1.2-MEGW R-F INDUCTION HEATER



REFER TO FIG. 22b FOR PHOTOGRAPH OF MODEL

TYPICAL RESULTS FROM INITIAL SIMULATED PROPELLANT HEATING TESTS

1.2-MEGW R-F INDUCTION HEATER
SEE FIG. 38 FOR SKETCH OF CONFIGURATION



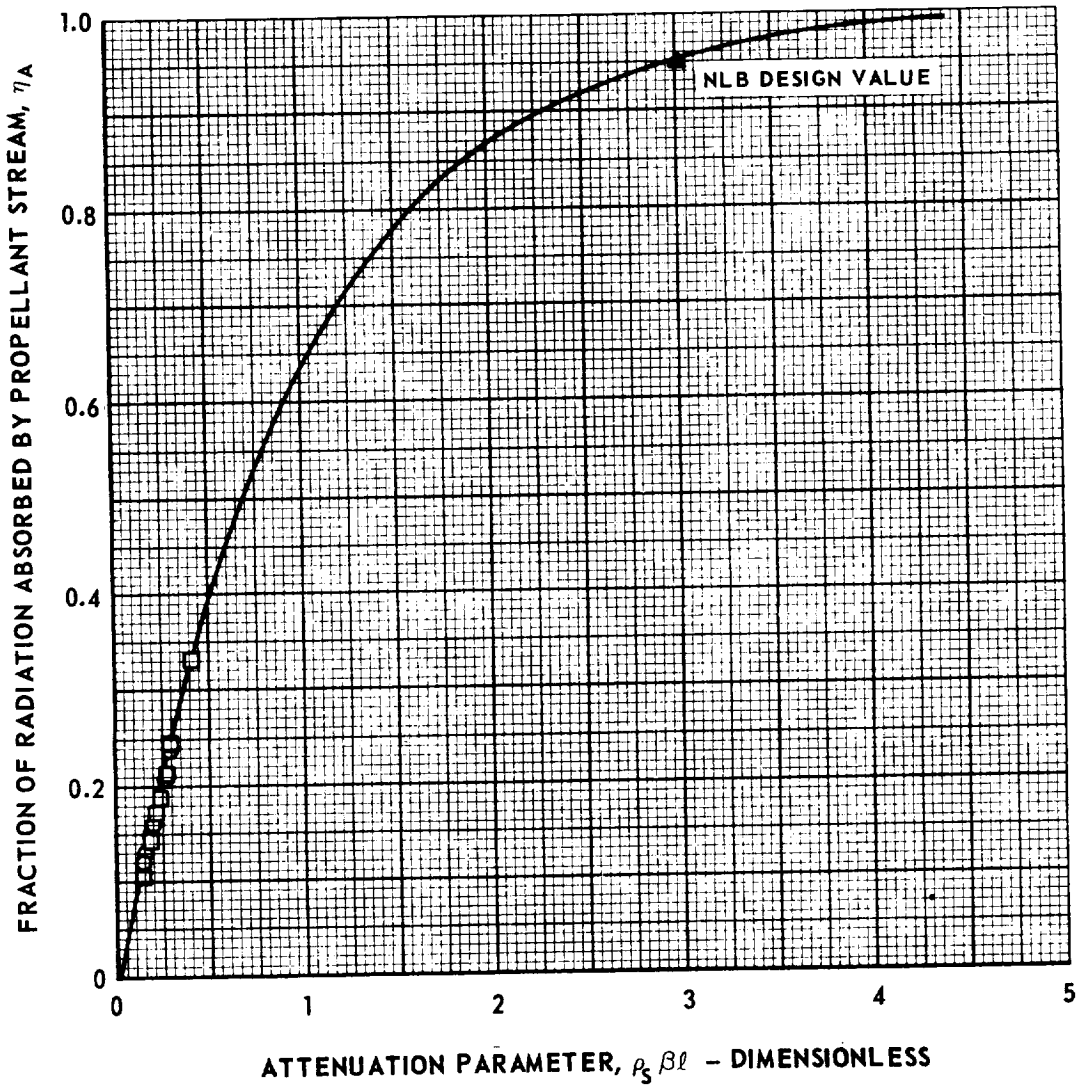
EFFECT OF ATTENUATION PARAMETER ON FRACTION OF RADIATION ABSORBED BY PROPELLANT STREAM

SEE FIGS. 36 AND 38 FOR SKETCH OF CONFIGURATIONS

○ - 1.2 MEGW R-F INDUCTION HEATER TESTS

□ - D-C ARC HEATER TESTS

$$\eta_A = 1 - e^{-\rho_s \beta l}$$



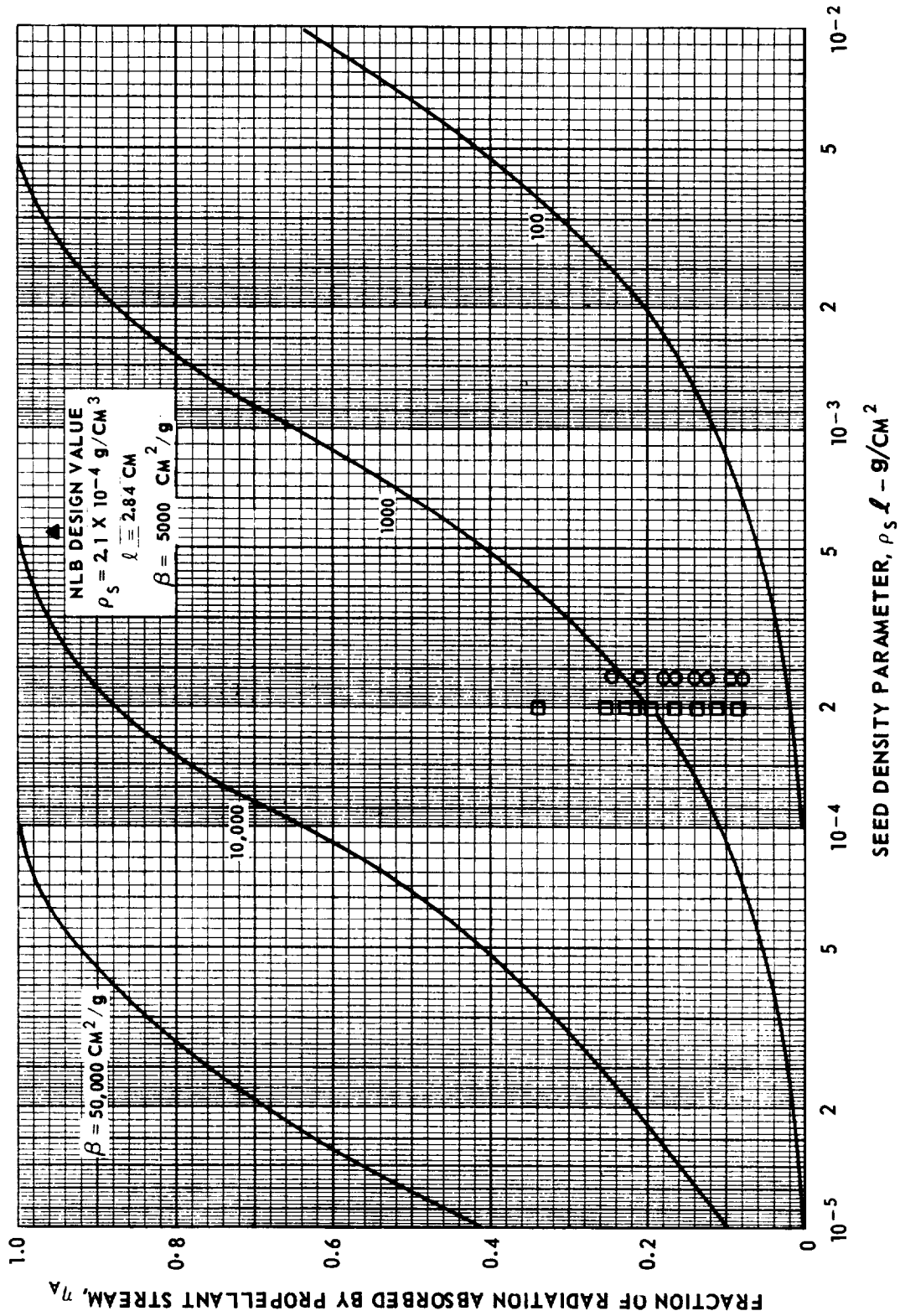
EFFECT OF PROPELLANT STREAM SEED DENSITY ON FRACTION OF RADIATION ABSORBED BY PROPELLANT STREAM

SEE FIG. 36 AND 38 FOR SKETCH OF CONFIGURATIONS

○ 1.2-MEGW R-F INDUCTION HEATER TESTS

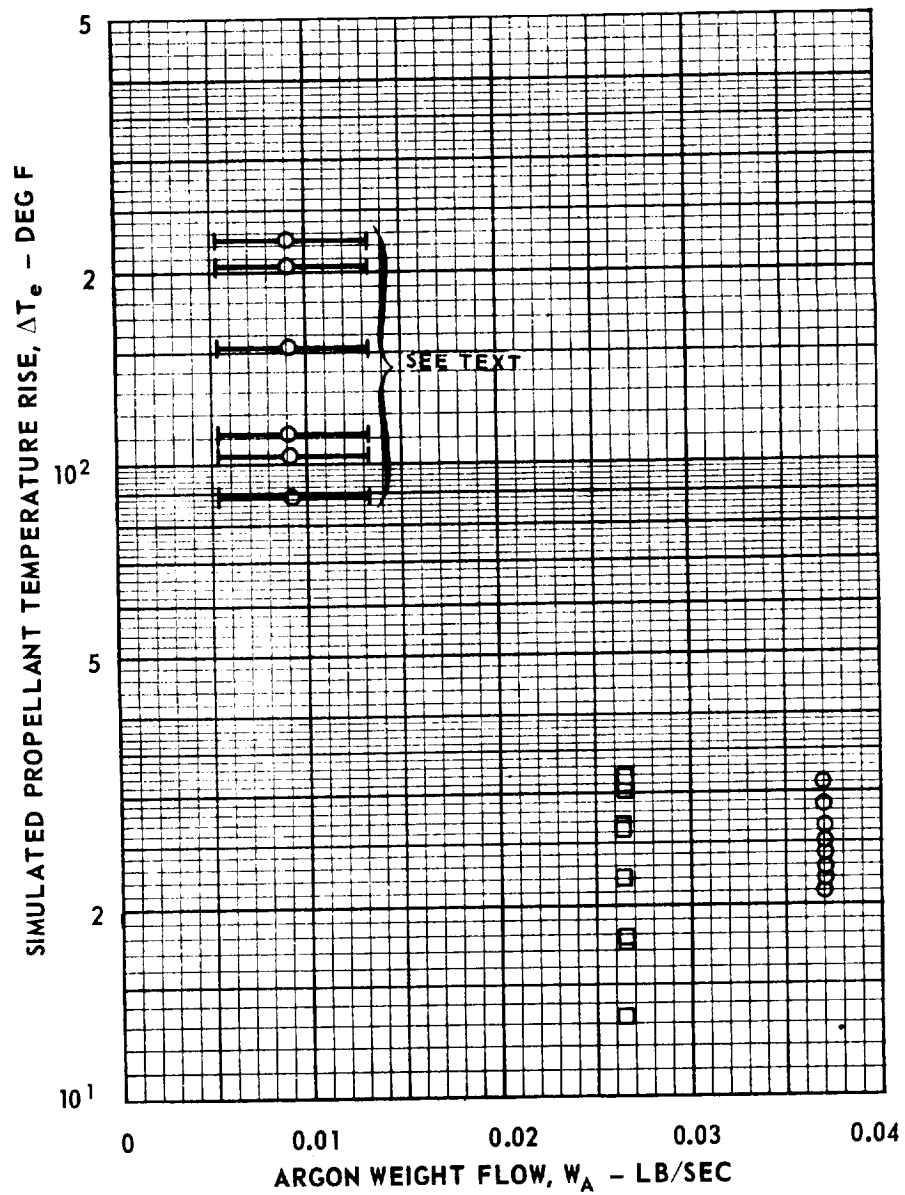
□ D-C ARC HEATER TESTS

$$\eta_A = 1 - e^{-\rho_S \ell \beta}$$



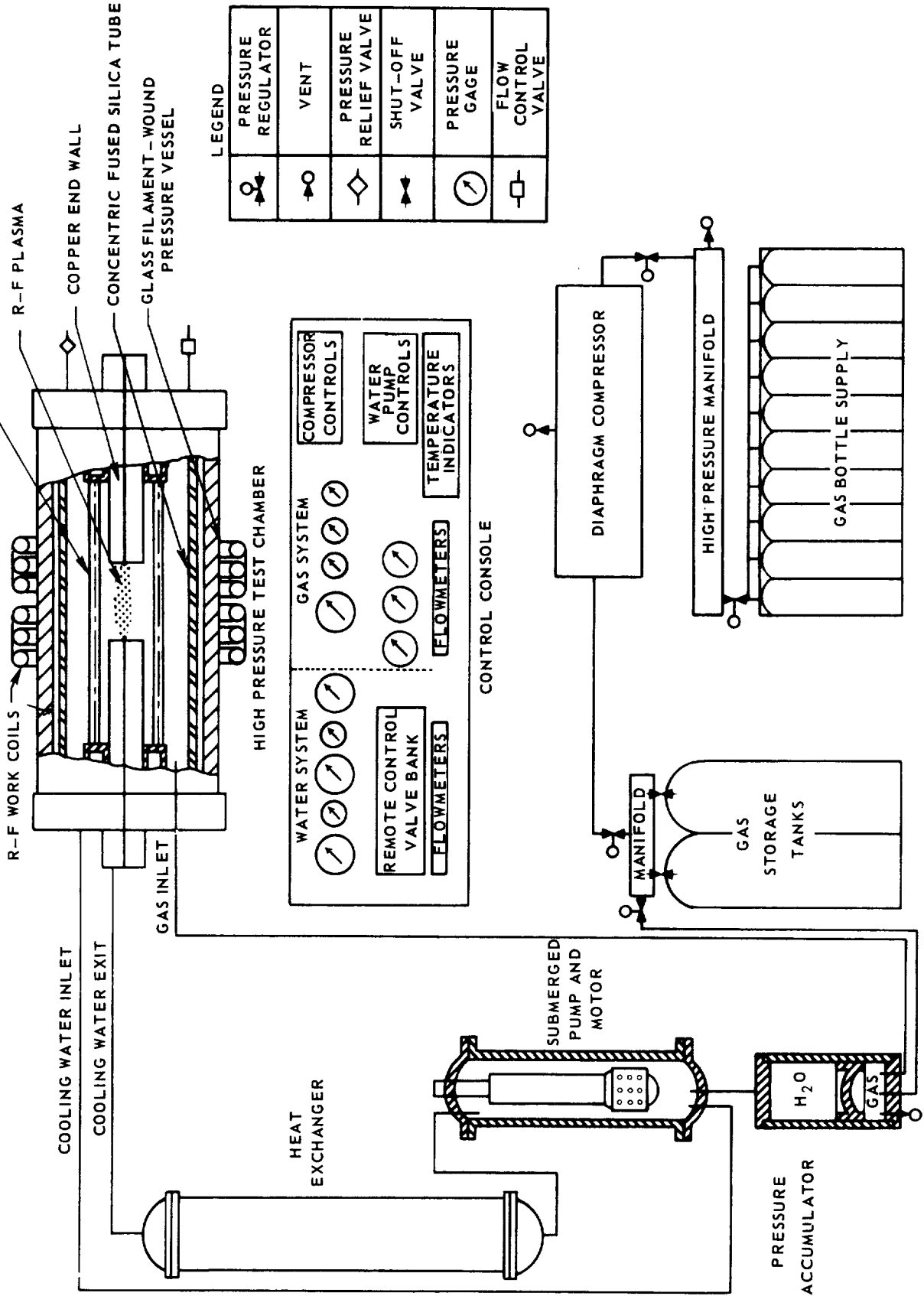
EFFECT OF ARGON WEIGHT FLOW ON SIMULATED PROPELLANT TEMPERATURE RISE

SEE FIGS. 36 AND 38 FOR SKETCH OF CONFIGURATION
 CONCENTRIC - COOLANT-TUBE MODELS
 ○ 1.2-MEGW R-F INDUCTION HEATER TESTS 1.06-IN.-ID MODEL
 □ D-C ARC HEATER TESTS 1.26-IN.-ID MODEL



BLOCK DIAGRAM OF POSSIBLE 200- AND 500-ATM R-F PLASMA TEST EQUIPMENT

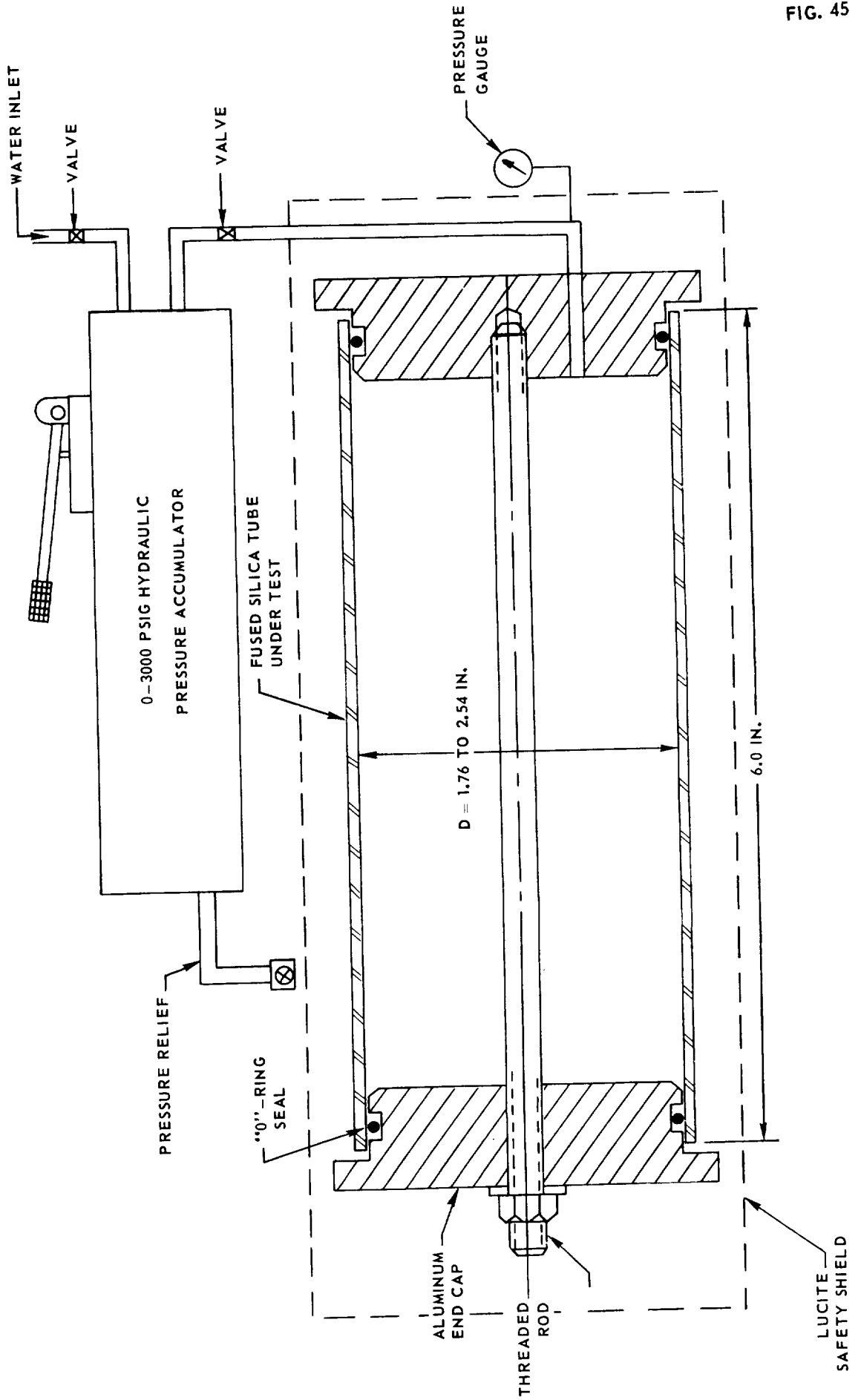
SEPARATE GAS AND WATER SYSTEMS FOR DIFFERENT TEST CONFIGURATIONS NOT SHOWN
 TRANSPARENT - WALL MODEL



LEGEND

	PRESSURE REGULATOR
	VENT
	PRESSURE RELIEF VALVE
	SHUT-OFF VALVE
	PRESSURE GAGE
	FLOW CONTROL VALVE

TEST EQUIPMENT EMPLOYED IN MECHANICAL TESTS OF FUSED SILICA TUBES



RESULTS OF HYDROSTATIC PRESSURE TESTS ON FUSED SILICA TUBES

REFER TO FIG. 45 FOR TEST CONFIGURATION

